



Shalinee Jha M. Tech.

**Biochemical and metabolic studies towards the characterization of
dipeptidyl peptidase-3 knockout mice**

DOCTORAL THESIS

to achieve the university degree of
Doktorin der Naturwissenschaften
submitted to

Graz University of Technology

Supervisor

Univ.-Prof. Mag. rer. nat. Dr. rer. nat. Peter Macheroux
Institute of Biochemistry
Graz University of Technology

Graz, October 2018

AFFIDAVIT

I declare that I have authored this thesis independently, that I have not used other than declared sources/resources, and that I have explicitly indicated all material which has been quoted either literally or by content from the sources used. The text document uploaded to TUGRAZonline is identical to the present doctoral thesis.

Date

Signature

The PhD thesis, titled “Biochemical and metabolic characterization of dipeptidyl peptidase 3 (DPP3) knockout mice”, was completed under supervision of Univ. Prof. Mag. rer. nat. Dr. rer. nat. Peter Macheroux at the Institute of Biochemistry at the Faculty of Technical Chemistry, Chemical & Process Engineering and Biotechnology at Graz University of Technology between November 2014 and October 2018.

*To my family
And friends who are like family!*

Acknowledgments

The journey of my PhD has been rewarding with a fair share of highs and lows. Not only has it taught me scientific skills, but valuable life skills as well. This certainly would not have been possible without the support of many people. I take this opportunity to express my gratitude to all the people who have been instrumental in the completion of this thesis in some way.

I would like to show my deepest gratitude to my supervisor Prof. Peter Macheroux for giving me the opportunity to work on a wonderful project which never ceased to challenge us. Your enthusiasm for science motivated me to perform better. I can never thank you enough for inspiring me in so many ways with your dedication and perseverance. I want to thank the DK Molecular Enzymology Doctoral Program for funding this research and for providing me the opportunity to move to the beautiful country Austria. I would also like to thank my thesis committee members: Prof. Robert Zimmermann, Prof. Rolf Breinbauer and Prof. Karl Gruber, and my thesis examiner, Prof. Tobias Madl, for their valuable contributions in designing this project. The DPP3 project is highly collaborative, with our co-operation partners spanning from universities to companies in many different cities. I would like to take this opportunity to thank each and every person involved in this collaboration for their valuable contributions towards this project.

A special thanks goes to Ulrike Taschler for being my mentor and introducing me to all the amazing mouse experiments. You were always the person I could reach out to when things did not work. I am grateful to you for your patience and constructive criticism. I want to additionally thank Jakov Ivkovic and Prashant Kumar who worked on this project before me and thus, introduced me to many aspects of the project.

This is also the time to mention the support that I received from the administrative staff of TU and KFU, Graz. I would like to thank Kristina Schilds, Annemarie Lehsl and Tinkara Kristovic who ensured that there were no glitches in the administrative affairs. On a similar note, I am immensely thankful to our technical staff, Eva-Maria Frießer, Rosemarie Trenker-El-Toukhy, Elfriede Zenzmaier and Alma Makic for their help.

I consider myself lucky to be a part of a lab which was equally motivated for work and fun. I have had the joy of engaging scientific discussions as well as friendly gossips over coffee or ice-cream with my colleagues from the Biochemistry department. I would like to thank, in no

particular order, Eveline Brodl, Bastian Daniel, Peter Augustin, Barbara Konrad, Johannes Niederhauser, Grazia Davidovic, Samiullah Khan, Julia Messenlehner, Gustav Oberdorfer, Andreas Winkler, Stefan Ettl and Geoffrey Gourinchas for making the workplace so exciting. I will always cherish our Institute trips, international lunches, cake times and Christmas parties. I want to especially thank Marina Toplak for all the scientific help and for our game evenings. I would also like to extend this acknowledgement to the temporary members of our lab, the master, bachelor and project students who, even in their limited time, added tremendous impact.

There are some people who make a place in your heart for all the right reasons and I was fortunate to meet some of these special people during my PhD. This acknowledgement will not be complete without thanking all of them. I want to thank Wolf-Dieter Lienhart for his stress-relieving fitness sessions, card tricks, nerf gun and billiard matches. I want to thank Chanakan Tongsook for all the marvellous cakes and for being a part of our girly trips. I want to thank Majd Lahham for giving company on late evenings and weekends in the lab. I want to thank Silvia Wallner for always giving the right advice and for the delicious Christmas cookie baking tradition every year. I want to thank Emilia Strandback, Karin Koch and Chaitanya Tabib, not only for their constant scientific help but also for joining me in figuring out life as we go along. Thank you for all the memories that we made together. Thank you Savitri Tabib for joining us in those memories. All of you made Graz a home away from home for me.

Last, but definitely not the least, I would like to thank my family for always being a pillar of support for me and always believing in me. The distances are difficult but the warmth never fades away.

I remain indebted to all of them for their guidance and support.

“Life is an equilibrium state between synthesis and degradation of proteins.”

Yoshinori Ohsumi

Nobel Prize in Physiology or Medicine, 2016

Abstract

Dipeptidyl peptidase 3 (DPP3) is a metallopeptidase containing a catalytic center with bivalent metal, such as Zn^{2+} or Co^{2+} as cofactor. It belongs to the M49 family, which is characterized by the presence of two signature motifs: HEXXGH and EEXRAE/D, involved in the coordination of the metal ion. DPP3 preferentially hydrolyzes peptides from 4 to 12 amino acids in length. Several bioactive peptides have been identified as DPP3 substrates. These include endogenous opioid peptides and peptides from the renin-angiotensin system. DPP3 has been implicated in an array of pathophysiological processes. It is upregulated in cancer cells and involved in apoptosis modulation and blood pressure regulation. There are strong evidences suggesting its role in endogenous pain regulation and defense against oxidative damage. However, the precise molecular mechanisms underlying the mediation of these effects by DPP3 are still unknown.

This thesis embarks on the metabolic and behavioral characterization of DPP3 knockout mice. Using an amalgamation of biochemical, biophysical and physiological studies, the knockout mice were compared to control wildtype mice. It was found that DPP3 deletion results in altered levels of several angiotensin peptides, thereby consolidating its involvement in the renin-angiotensin pathway, which affects the reno-cardiovascular circuit in mammals. There is also an indication of oxidative stress in the DPP3 knockout mice due to angiotensin II-mediated reactive oxygen species (ROS) production.

The second focus of this thesis revolved around the design and characterization of specific inhibitors against DPP3. These inhibitors can be exploited to gain structural and mechanistic insights into ligand binding to DPP3, which can ultimately reveal its substrate specificity and selectivity. Kinetic screening yielded two compounds – (*R*)-hydroxyethelene (*HER*) and (*S*)-hydroxyethelene (*SHE*), which effectively inhibit DPP3 *in vitro*. Additionally, a comparison of *HER* with tynorphin, the strongest inhibitor reported against DPP3, showed that *HER* is more effective in stably inhibiting DPP3 over a period of time.

Towards the end, the thesis presents an outlook into utilizing peptidomic approaches to identify natural substrates of DPP3. Since a peptidase may cleave many substrates *in vitro*, traditional biochemical approaches for determining endogenous substrates are time consuming and may be unreliable. Therefore, assessing the global changes in the peptidome following the knockout of DPP3 may facilitate identification of peptides likely to be substrates or products of DPP3.

Kurzfassung

Dipeptidyl peptidase 3 (DPP3) ist eine Metallopeptidase mit einem katalytisch aktiven bivalenten Metallion, wie Zn^{2+} oder Co^{2+} . Das Enzym zählt zur M49 Proteinfamilie, welche durch zwei Sequenzmotive gekennzeichnet ist: HEXXGH und EEXRAE/D, welche beide für die Koordinierung des Metallions wichtig sind. DPP3 hydrolysiert bevorzugt Peptide mit einer Länge von 4 bis 12 Aminosäuren, wobei verschiedene bioaktive Peptide als Substrate für DPP3 identifiziert wurden. Dazu zählen z.B. endogene opioide Peptide und Peptide des Renin-Angiotensin Systems. DPP3 wird mit einer Vielzahl pathophysiologischer Prozesse in Verbindung gebracht. Es wurde gezeigt, dass DPP3 in Krebszellen hochreguliert ist und eine wichtige Rolle in Apoptose und Bluthochdruck-Regulierung spielt. Außerdem gibt es starke Hinweise auf einen Einfluss von DPP3 in Prozesse wie die endogene Schmerzregulierung und oxidativen Stress. Der genaue Mechanismus für diese breite Wirkung von DPP3 ist jedoch noch nicht bekannt.

In dieser Arbeit wird eine Charakterisierung von DPP3 Knockout Mäusen präsentiert. In einer Kombination biochemischer, biophysikalischer und physiologischer Studien wurden metabolische Parameter und das Verhalten von Knockout Mäusen mit Kontroll-Wildtyp Mäusen verglichen. Es konnte gezeigt werden, dass die Deletion von DPP3 die Levels von Angiotensin Peptiden verändert, was auf eine Beteiligung des Enzyms am Renin-Angiotensin Weg schließen lässt. Es gibt außerdem Hinweise auf oxidativen Stress in DPP3 Knockout Mäusen aufgrund der durch Angiotensin-II mediierten Produktion von Reaktiven Sauerstoffspezies (ROS).

Der zweite Focus dieser Arbeit lag im Design und der Charakterisierung spezifischer Inhibitoren von DPP3. Diese Inhibitoren können verwendet werden um strukturelle und mechanistische Erkenntnisse zur Substratspezifität und Selektivität des Enzyms zu erhalten. Ein *in vitro* durchgeführtes kinetisches Screening ergab zwei potentielle Inhibitoren: (*R*)-Hydroxyethelen (*HER*) und (*S*)-Hydroxyethelen (*SHE*). Zusätzlich zeigte ein Vergleich von *HER* mit Tynorphin, dem bis dato stärksten DPP3 Inhibitor, dass die neu identifizierte Verbindung DPP3 über einen längeren Zeitraum effektiver und stabiler inhibiert.

Am Ende dieser Arbeit wird außerdem noch ein Ausblick auf die Verwendung Peptidomischer Ansätze zur Identifizierung natürlicher Substrate von DPP3 gegeben. Nachdem Peptidasen *in vitro* sehr viele verschiedene Substrate hydrolysieren, sind traditionelle biochemische Ansätze bei der Suche nach endogenen Substraten zeitaufwändig

und nur wenig verlässlich. Daher erscheint die Untersuchung von durch den Knockout von DPP3 resultierenden Veränderungen im Peptidom eine vielversprechend Strategie zur Identifizierung von Peptiden, die als Substrate oder Produkte von DPP3 dienen.

-
- Parts of this thesis have been published in:
1. Koch K, Strandback E, Jha S, Richter G, Bourgeois B, Madl T and Macheroux P. Oxidative stress induced structural changes in the microtubule-associated flavoenzyme Irc15p from *Saccharomyces cerevisiae*. **Protein Science**. 2018 Sep 29.
 2. Rehfeld L, Funk E, Jha S, Macheroux P, Mellander O and Bergmann A. Novel methods for the quantification of Dipeptidyl Peptidase 3 (DPP3) concentration and activity in human blood samples. (Accepted in **The Journal of Applied Laboratory Medicine**).
- The synthesis of hydroxyethylene transition state peptidomimetic inhibitors (*R*)-hydroxyethylene and (*S*)-hydroxyethylene has been published in the doctoral thesis of Dr. Jakov Ivkovic (PhD student in the lab of Prof. Rolf Breinbauer, Department of Organic Chemistry, Graz University of Technology)

TABLE OF CONTENTS

<i>Acknowledgements</i>	V
<i>Abstract</i>	VIII
<i>Kurzfassung</i>	IX
<i>Dipeptidyl peptidase 3- an emerging player in the Renin-Angiotensin System</i>	1-17
Peptidases.....	2
Dipeptidyl peptidases.....	3
Dipeptidyl peptidase 3 (DPP3).....	4
DPP3 has unique sequence attributes.....	5
Structure, catalytic mechanism and mode of substrate binding in DPP3.....	6
Substrates and inhibitors of DPP3.....	8
DPP3 in pain modulation.....	10
DPP3 in oxidative stress.....	11
DPP3 in the renin-angiotensin system (RAS).....	12
References.....	14
<i>Knock-out of DPP3 in mice unravel its involvement in the metabolic regulation of the renin angiotensin system</i>	18-44
Abstract.....	21
Introduction.....	22
Results.....	24
Discussion.....	33
Materials and Methods.....	35
References.....	41
<i>Efficient inhibition of a metallopeptidase by hydroxyethylene transition state peptidomimetics</i>	45-90
Abstract.....	48
Introduction.....	49
Results.....	51
Discussion.....	57
Materials and Methods.....	58
References.....	89

Novel methods for the quantification of Dipeptidyl Peptidase 3 (DPP3) concentration and activity in human blood samples.....91-115

Abstract.....	94
Introduction.....	95
Results.....	97
Discussion.....	104
Materials and Methods.....	106
References.....	113

Peptidomics based approach to identify endogenous substrates of DPP3.....116-128

Abstract.....	119
Introduction.....	120
Results.....	121
Discussion.....	121
Materials and Methods.....	123
References.....	127

Appendix.....129-165

Oxidative stress induced structural changes in the microtubule-associated flavoenzyme Irc15p from Saccharomyces cerevisiae.....130-161

Abstract.....	132
Introduction.....	133
Results.....	136
Discussion.....	147
Materials and Methods.....	150
References.....	158

Curriculum Vitae.....162

List of Publications.....164

List of Posters and Oral Presentations.....165

Chapter 1

Dipeptidyl peptidase 3- an emerging player in the Renin- Angiotensin System

Peptidases

Peptidases are a complex group of enzymes with immense physiological significance found ubiquitously in nature. These enzymes influence crucial metabolic functions and ultimately the survival of a cell via peptide hydrolysis. The process of peptide hydrolysis is substrate specific and a site directed action that directly affects the synthesis, composition, size, shape, turnover and finally destruction of proteins (1). The term “peptidase” encompasses all the proteolytic enzymes, proteases, and proteinases in general. Their hydrolytic activity ensures that peptides and proteins are transported to the correct cellular or extracellular locations, are activated or inactivated when required, and that biologically important peptide products are formed. These enzymes hydrolyze the peptide bonds of proteins and/or peptides. Peptidases regulate several important physiological processes such as total protein turnover in the cell, tissue remodeling, blood-pressure control, water and fluid homeostasis, signaling cascades and interactive pathways.

Peptidases are divided into endopeptidases and exopeptidases, depending on if they cut in the middle or at the ends of their substrates, respectively. Exopeptidases can further be classified into aminopeptidases and carboxypeptidases, which cleave off N-terminal and C-terminal amino acids, respectively. The carboxypeptidases are further assigned to three groups on the basis of catalytic mechanism: the serine-type carboxypeptidases, the metallo-carboxypeptidases, and the cysteine-type carboxypeptidases. Other types of exopeptidases are specific for dipeptides (dipeptidases), acting on peptides containing modified amino acids (omega peptidases). The endopeptidases are classified based on the element which is vital for catalysis. These are the sub-subclasses of serine endopeptidases, cysteine endopeptidases, aspartic endopeptidases, metalloendopeptidases and threonine endopeptidases (Table 1).

Proteolytic enzymes require very intricate levels of regulation to ensure proper functioning and to avoid any unwanted activity. Therefore, these enzymes are controlled either at the transcriptional level or through post-translational modifications. There are a plethora of other regulatory mechanisms which exist to control the activity of proteolytic enzymes; some of these include synthesis of these enzymes in the form of inactive zymogens that require further activation, substrate availability and specificity, cofactor binding and presence of physiological inhibitors. Any aberration in the regulatory mechanisms can result in

pathologies like cardiovascular diseases, tumor and tumor-associated oxidative stress angiogenesis, neurological disorders or inflammatory disorders. Because of their involvement in a multitude of diverse pathophysiological processes, peptidases are regarded as promising drug targets, and therefore studies are necessary to better understand their structural and functional mechanisms at the molecular level (2).

Subclass	Peptidase	Number of entries
EC 3.4.11	Aminopeptidases	26
EC 3.4.13	Dipeptidases	12
EC 3.4.14	Dipeptidyl peptidases and tripeptidyl peptidases	9
EC 3.4.15	Peptidyl dipeptidases	4
EC 3.4.16	Serine-type carboxypeptidases	4
EC 3.4.17	Metallo-carboxypeptidases	20
EC 3.4.18	Cysteine-type carboxypeptidases	1
EC 3.4.19	Omega peptidases	9
EC 3.4.21	Serine endopeptidases	97
EC 3.4.22	Cysteine endopeptidases	58
EC 3.4.23	Aspartic endopeptidases	40
EC 3.4.24	Metallic endopeptidases	81
EC 3.4.25	Threonine endopeptidases	2
	Total	363

Table 1 Classification of peptidases EC system

Dipeptidyl peptidases

Dipeptidyl peptidases (DPPs) comprise of a unique family of proteolytic enzymes that perform site-specific cleavage of dipeptides from the N-terminus of oligopeptides. They are classified under EC 3.4.14 belonging to a protease family in the Nomenclature Committee of the International Union of Biochemistry and Molecular Biology. Eight different DPPs have been identified in the mammalian species till now. DPPs have broad substrate specificity and mostly catalyze the degradation of bioactive peptides including neurotransmitters, peptide hormones and chemokines (Figure 1). In the past two decades, extensive research has been done on dipeptidyl peptidase 4 (DPP4) that modulates glucose metabolism, signal

transduction and apoptosis. An increasing number of pharmacological inhibitors against DPP4 have been developed and they are mostly used in the treatment of type 2 diabetes and obesity. Recently, another enzyme from this family, dipeptidyl peptidase 3 (DPP3) has been in focus of researchers, due to its purported involvement in the regulation of a plethora of physiological and pathological functions. In this chapter, we provide an overview about the pathophysiological functions of DPP3, and discuss the future potential of this enzyme from a pharmacological perspective.

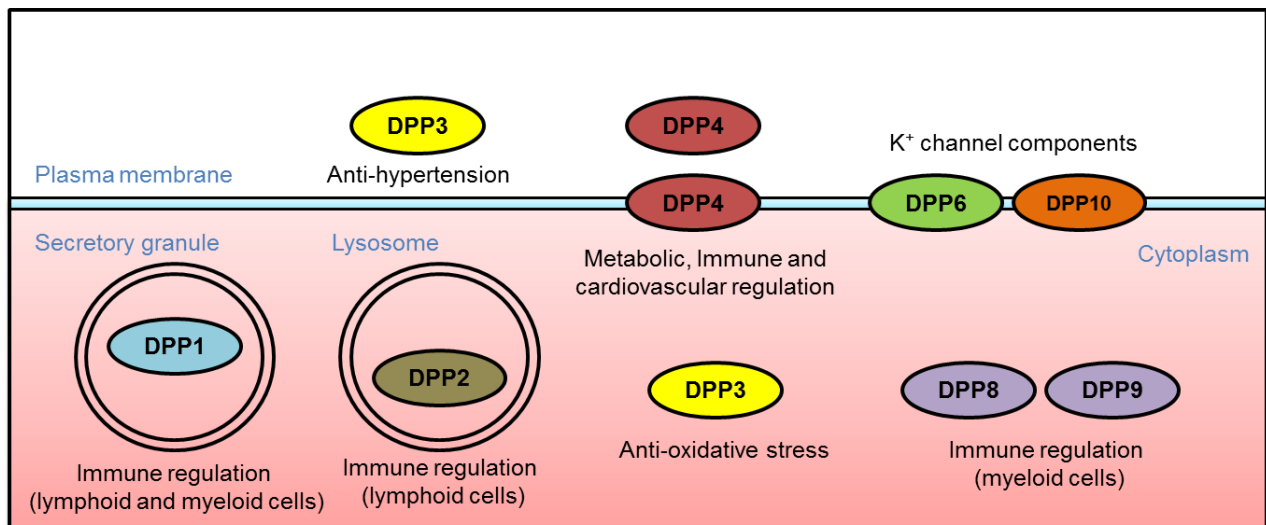


Figure 1 Location and function of different dipeptidyl peptidases (adapted from (3))

Dipeptidyl peptidase 3 (DPP3)

DPP3 (EC 3.4.14.4) was purified from bovine pituitary for the first time (4). It was assigned this name on virtue of being the third dipeptidyl peptidase to be discovered. Subsequently, it has been purified from many other tissues and organisms ranging from lower to higher eukaryotes. By virtue of its affinity for different types of bioactive peptides and synthetic substrates, it was named enkephalinase B (5), red cell angiotensinase (6), dipeptidyl aminopeptidase 3 (5) and dipeptidyl arylamidase 3 (4). DPP3 is a zinc-dependent metallopeptidase and cleaves dipeptides sequentially from the N-terminus of oligopeptides ranging from 4-12 amino acids in length. Even though DPP3 was identified and kinetically characterized as early as in the year 1967 (4), further research was slow, mainly due to the lack of knowledge about substrate specificity and unavailability of crystal structure. However, in the recent years, DPP3 research has gained momentum due to its implications in

pathophysiology such as ovarian carcinoma (7), pain modulation (8-10), Nrf2 mediated oxidative stress (11, 12) and blood pressure regulation (13, 14). In the meantime, X-ray crystal structures of DPP3 from yeast (15) and human (16) origin have been resolved. This introductory chapter elucidates the involvement of DPP3 in cellular physiology and the catalytic mechanism of substrate hydrolysis, which may eventually help in identification of the new physiological substrates.

DPP3 has unique sequence attributes

Members of the metallopeptidase clan (clan MA) of the protease family are characterized by the presence of a signature motif HEXXH essential for catalysis. The two His residues of this motif coordinate the divalent metal ion (mostly Zn^{2+} , rarely Mn^{2+} , Co^{2+} , Ni^{2+} or even Cu^{2+}). The metal ion and the amino acid residues in the surrounding environment contact a nucleophilic water molecule. DPP3 contains a similar but unique catalytic motif HEXXGH, which is distinguishable from other metallopeptidases. The two His residues of this motif along with the Glu residue of a second conserved motif EEXRAE/D have been proposed to coordinate the Zn^{2+} ion binding (Figure 2). Owing to the presence of the unique catalytic motif HEXXGH, DPP3 is assigned to a novel metallopeptidase family M49. Yeast (*Saccharomyces cerevisiae*) DPP3 (yDPP3), which shares 36% sequence identity with its human counterpart has been assigned as the prototype of this family. Even though there exist significant variations in catalytic motifs of yDPP3 and hDPP3, residues which are important for catalysis are conserved.

Based upon their strong inhibition by serine peptidase inhibitors, mammalian DPP3s were previously assumed to belong to the serine peptidase clan. However, recent analysis of DPP3 crystal structure revealed that Glu461 (in yeast) and Glu451 (in mammals) acts as a base in a general acid-base type catalytic reaction to deprotonate the water molecule, thereby resulting in its activation (15, 16). Consequently, this Glu residue is considered to be critical for the enzymatic activity. The importance of the Glu residue was experimentally validated by mutagenesis studies of this residue which led to a 15000-fold reduction in yDPP3 catalytic activity (15). Mutation of the corresponding Glu residue in rat DPP3 (Glu451) to alanine or aspartic acid resulted in a complete inactivation of the enzyme. Logically, DPP3 is now considered to be a member of the zinc metallopeptidase clan rather than a serine peptidase.

	580	590	600	610	620	630	640	650	660
<i>H.sapiens</i>	FDVQVGL	HE LLGH	SGKLFVQDEKGFNFDQE	TVINPETGEQIQ	SWYRSGETWDSKFSTIASSY	EECRAE	SVGLYLCLHP		
<i>N.leucogenys</i>	FDVQVGL	HE LLGH	SGKLFVQDEKGFNFDQE	TVINPETGEQIQ	SWYRSGETWDSKFSTIASSY	EECRAE	SVGLYLCLHP		
<i>M.mulatta</i>	FDVQVGL	HE LLGH	SGKLFVQDEKGFNFDQE	TVINPETGEQIQ	SWYRSGETWDSKFSTIASSY	EECRAE	SVGLYLCLHP		
<i>O.gamettii</i>	FDVQVGL	HE LLGH	SGKLFVQDEKGFNFDQE	TVINPETGEQIQ	SWYRSGETWDSKFSTIASSY	EECRAE	SVGLYLCLHP		
<i>E.caballus</i>	FDVQVGL	HE LLGH	SGKLFVQDEKGFNFDQE	TVINPETGEQIQ	SWYRSGETWDSKFSTIASSY	EECRAE	SVGLYLCLHP		
<i>B.taurus</i>	FDVQVGL	HE LLGH	SGKLFVQDEKGFNFDQE	TVINPETGEQIQ	SWYRSGETWDSKFSTIASSY	EECRAE	SVGLYLCLHP		
<i>A.melanoleuca</i>	FDVQVGL	HE LLGH	SGKLFVQDEKGFNFDQE	AVINPETGEQIQ	SWYRSGETWDSKFSTIASSY	EECRAE	SVGLYLCLDP		
<i>O.cuniculus</i>	FDVQVGL	HE LLGH	SGKLFVQDEKGFNFDQE	TVINPETGEQIQ	SWYRSGETWDSKFSTIASSY	EECRAE	SVGLYLCLHP		
<i>C.i.familiaris</i>	FDVQVGL	HE LLGH	SGKLFVQDEKGFNFDQE	TVINPETGEQIQ	SWYRSGETWDSKFSTIASSY	EECRAE	SVGLYLCLHP		
<i>F.catus</i>	FDVQVGL	HE LLGH	SGKLFVQDEKGFNFDQE	TVINPETGEQIQ	SWYRSGETWDSKFSTIASSY	EECRAE	SVGLYLCLHP		
<i>S.harrisii</i>	FEVQVGL	HE LLGH	SGKLFVQDEKGFNFDQN	TVINPETGEQIR	SWYRSGETWDSKFSTIASSY	EECRAE	SVGLYLCLHP		
<i>M.domestica</i>	FEVQVGL	HE LLGH	SGKLFVQDDKGFNFDQN	TVINPETGEQIS	SWYRSGETWDSKFSTIASSY	EECRAE	SVGLYLCLHP		
<i>M.furo</i>	FDVQVGL	HE LLGH	SGKLFVQDEKGFNFDQE	TVINPETGEQIQ	SWYRSGETWDSKFSTIASSY	EECRAE	SVGLYLCLHP		
<i>I.tridecemlineatus</i>	FDVQVGL	HE LLGH	SGKLFVQDEKGFNFDQE	TVINPETGEQIQ	SWYRSGETWDSKFSTIASSY	EECRAE	SVGLYLCLHP		
<i>R.norvegicus</i>	FDVQVGL	HE LLGH	SGKLFVQDEKGFNFDQE	TVINPETGEQIQ	SWYRSGETWDSKFSTIASSY	EECRAE	SVGLYLCLHP		
<i>C.jacchus</i>	FDVQVGL	HE LLGH	SGKLFVQDEKGFNFDQE	TVINPETGEQIQ	SWYRSGETWDSKFSTIASSY	EECRAE	SVGLYLCLHP		
<i>C.porcillus</i>	FDVQVGL	HE LLGH	SGKLFVQDEKGFNFDQE	TVINPETGEQIQ	SWYRSGETWDSKFSTIASSY	EECRAE	SVGLYLCLHP		
<i>M.musculus</i>	FDVQVGL	HE LLGH	SGKLFVQDEKGFNFDQE	TVINPETGEQIQ	SWYRSGETWDSKFSTIASSY	EECRAE	SVGLYLCLHP		
<i>M.auratus</i>	FDVQVGL	HE LLGH	SGKLFVQDEKGFNFDQE	TVINPETGEQIQ	SWYRSGETWDSKFSTIASSY	EECRAE	SVGLYLCLHP		
<i>M.lucifugus</i>	FDVQVGL	HE LLGH	SGKLFVQDEKGFNFDQE	TVINPETGEQIQ	SWYRSGETWDSKFSTIASSY	EECRAE	SVGLYLCLHP		
<i>A.carolinensis</i>	FEVQVGL	HE LLGH	SGKLFVQDEKGFNFDQE	AVINPETGEQIR	SWYRSGETWDSKFSTIASSY	EECRAE	CVGLYLCLNK		
<i>X.laervis</i>	FEVQVGL	HE LLGH	SGKLFVQDEKGFNFDQE	TVINPETGEQIR	SWYRSGETWDSKFSTIASSY	EECRAE	CVGLYLCLNK		
<i>D.rerio</i>	FEVQVGL	HE LLGH	SGKLFVQDDKGFNFDQD	AVRNPETGELIS	SWYRSGETWDSKFSTIASSY	EECRAE	CVGLYLCLSK		
<i>O.niloticus</i>	FEVQVGL	HE LLGH	SGKLFVQDDKGFNFDQD	KVINPETGEPVS	SWYRSGETWDSKFSTIASSY	EECRAE	CVGLYLCLNK		
<i>N.vectensis</i>	FEVQVGL	HE LLGH	SGKLFVQDDKGFNFDQD	SVVNTETGEKIQ	SWYRSGETWDSKFSTIASSY	EECRAE	CVGLYLCLNK		
<i>B.dorsalis</i>	FEVQVGL	HE LLGH	SGKLFVQDDKGFNFDQD	NTKNLITGEPK	SWYRSGETWDSKFSTIASSY	EECRAE	AVGSLYLSLQA		
<i>D.melanogaster</i>	FEVQVGL	HE LLGH	SGKLFVQDDKGFNFDQD	NTKNLVTGEPIT	SWYRSGETWDSKFSTIASSY	EECRAE	AVGSLYLSLQR		
<i>S.japonicum</i>	FELQVGL	HE LLGH	SGKLFVQDDKGFNFDQD	STKDLITGGPIL	SWYRSGETWDSKFSTIASSY	EECRAE	CVGLYLCLNLP		
<i>S.cerevesiae</i>	FEVQVGL	HE LLGH	SGKLFVQDDKGFNFDQD	NPPGLDGGKPV	SWYRSGETWDSKFSTIASSY	EECRAE	VIMFLLTNK		
<i>T.cucumeris</i>	FDVQVAN	HE LLGH	SGKLFVQDDKGFNFDQD	KTINPLTGERVV	SWYRSGETWDSKFSTIASSY	EECRAE	CVGLYLGNR		
<i>S.stiptis</i>	FEVQVGL	HE LLGH	SGKLFVQDDKGFNFDQD	KVNTK	SWYRSGETWDSKFSTIASSY	EECRAE	LVALYLILKKI		
<i>C.thermophilum</i>	FEVQVGL	HE LLGH	SGKLFVQDDKGFNFDQD	TVINPETGEQIQ	SWYRSGETWDSKFSTIASSY	EECRAE	LVAMHLSCEF		
<i>N.crassa</i>	FEVQVGL	HE LLGH	SGKLFVQDDKGFNFDQD	TVINPETGEQIQ	SWYRSGETWDSKFSTIASSY	EECRAE	LVAMHLSCEF		
<i>D.discoidium</i>	FELQVGL	HE LLGH	SGKLFVQDDKGFNFDQD	EVINPLTNKPIDPKTEVYKFGETYDSVFKSLGSPM	EECRAE	CCGIYLSLPE			

Figure 2 Multiple sequence alignment of DPP3s from various species. HEXXGH is the characteristic catalytic motif of the M49 family of peptidases, whereas EECRAE is the second highly conserved motif of the family.

Structure, catalytic mechanism and mode of substrate binding in DPP3

The crystal structures of bacterial (PDB: 5NA7) (btDPP3), yeast (PDB: 3CSK) and human (PDB: 3FVY) DPP3 have been reported (15-17). All the structures contain two domains, an upper domain rich in α -helices and a lower domain with mixed α - and β -fold with a five-stranded β -barrel forming the structural core of this domain. The two domains are separated by a wide cleft, which has been proposed to be the substrate binding site (15). The two domains are interconnected by a helical loop extending from the lower domain. The catalytic motif (HEXXGH) and the secondary motif (EECRAE/D) are part of the upper domain, and are conserved in all DPP3 homologs. In case of yDPP3 and hDPP3, despite of having only 36% sequence identity, both the structures show an RMSD of 1.4 Å of their superimposed protein backbone. However, the superimposed protein backbones of btDPP3 and hDPP3 structures gave rise to an RMSD value of 4.41 Å (the same differences between bacterial and yeast DPP3 are observed). This is because the length of the spacer region between the two

evolutionarily conserved active-site motifs is much shorter in the bacterial protein, compared to eukaryotic DPP3s (15-17).

A catalytically critical zinc ion is observed in the conserved binding site in the upper domain. In hDPP3, Glu508, His455 and His450 are the residues involved in the coordination bond formation with zinc. These residues are also conserved in bacterial and yeast DPP3. In both human and yeast DPP3, a conserved water molecule is observed coordinating the zinc ion in a tetrahedral coordination. Glu461 (in yDPP3) and Glu451 (in hDPP3) side chains essential for peptide bond hydrolysis, are in turn hydrogen bonded to the conserved water molecule. In contrast, the coordination of the zinc ion in btDPP3 is square pyramidal with two water molecules in the remaining positions. Interestingly, in the case of btDPP3, the corresponding Glu449 does not point toward either of the two zinc-coordinated water molecules (17).

The proposed catalytic mechanism of hDPP3 is similar to other metalloenzymes like thermolysin (18) and neprilysin (19). A clear electron density for a water molecule coordinated to zinc was observed and therefore water-mediated catalysis is suggested to be the likely mechanism. It is further suggested that nucleophilicity of the Zn ion coordinated water molecule is enhanced by Glu451, a general base in the vicinity. The activated water molecule attacks the carbonyl carbon of scissile peptide bond, resulting in its hydrolysis. The leaving amino group is then protonated by the same Glu451, which in turn gets restored to its original form. As in the proposed mechanisms of thermolysin and neprilysin, the hydrogen bond between His568 and the carbonyl group of the scissile peptide bond (P1, Val2) likely provides additional stabilization of the tetrahedral intermediate.

The first co-crystal structure of human DPP3 with the opioid peptide tynorphin (VVYPW), revealed a large conformational change leading to the closure of the cleft separating the upper and lower domain (Figure 3). Peptide binding to DPP3 was shown to be driven by a change in the entropy and the release of ordered water molecules from the binding cleft is proposed to be mainly responsible for the increase in entropy. The peptide itself primarily interacts via its main chain with the lower domain (especially with the five-stranded β -barrel) and the domain motion is necessary to bring the scissile peptide group in proximity to the catalytic machinery of the enzyme (16, 20).

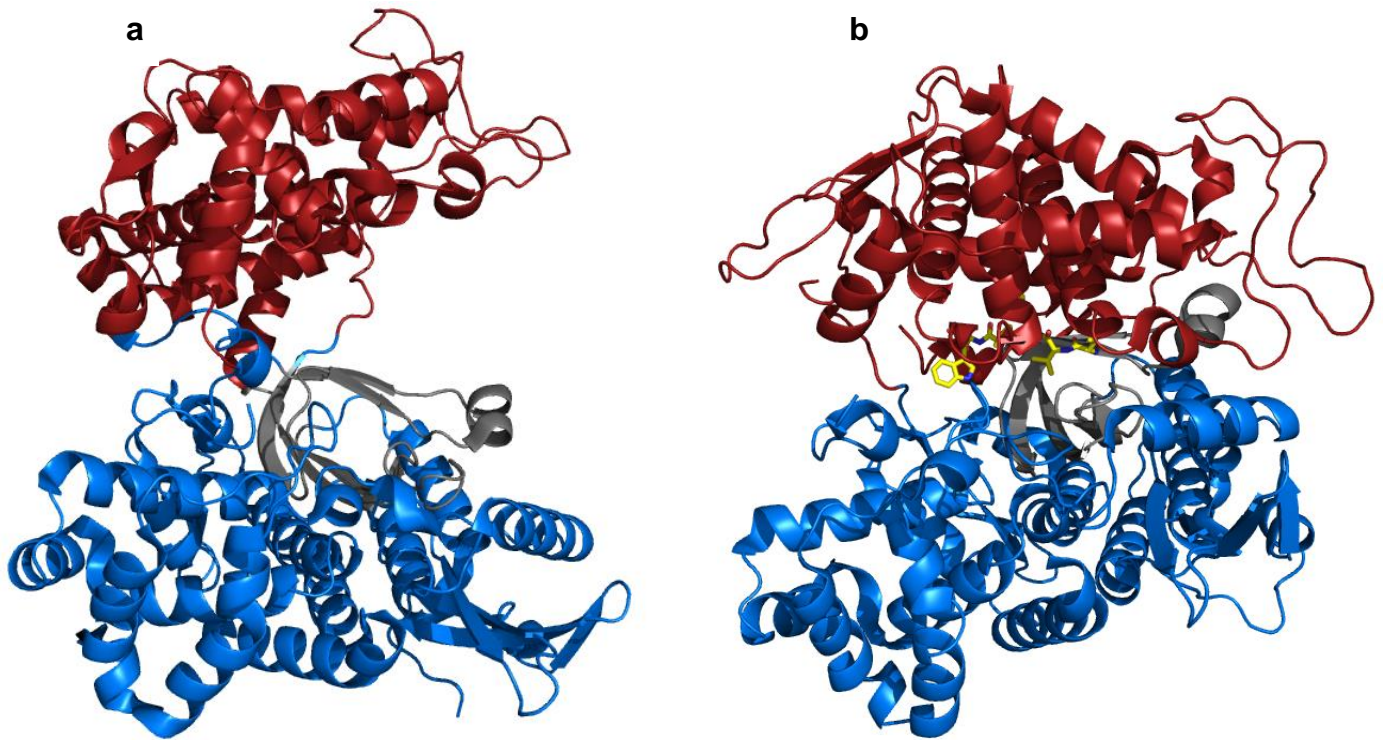


Figure 3 (a) Cartoon representation of the structure of the unbound hDPP3. The upper lobe is shown in red, the lower lobe in blue and the five-stranded β -core in grey. (b) Cartoon representation of the closed conformation of hDPP3. The bound peptide is shown in yellow. The figure was prepared using the program PyMol (<http://www.pymol.org/>).

Substrates and inhibitors of DPP3

A number of publications have reported characterization of DPP3 of bovine, porcine, monkey, rat, human, insect, yeast and other organisms, and determined its activity with important endogenous peptide substrates. In all of the relevant studies, a competitive inhibition assay using the standard Arg-Arg-amide substrates was used to provide a quantitative measure of affinity to the enzyme (Table 2). DPP3 sequentially cleaves dipeptides from a wide range of peptides with unsubstituted N-terminus. Tetrapeptides to octapeptides are considered to be the best substrates. It can be confirmed that DPP3 has good affinities to angiotensins and opioid peptides. This suggests a plausible role of DPP3 in the opioid signaling processes and regulation of cardiovascular events in connection to the renin-angiotensin system. Interestingly, the affinities of DPP3 towards angiotensins are an order of magnitude higher than the values for opioid peptides, thereby emphasizing the potential role of DPP3 more in the direction of blood pressure regulation.

Physiological peptide substrate	AA composition	Activity (K_i , μM)	Reference
<u>Angiotensins</u>			
Angiotensin II	Asp-Arg- -Val-Tyr-Ile-His-Pro-Phe	0.34, 3.6	(5, 21)
Angiotensin III	Arg-Val- -Tyr-Ile-His-Pro-Phe	0.22, 0.05	(5, 21)
Proctolin (insect neuropeptide)	Arg-Tyr- -Leu-Pro-Thr	1.2	(21)
<u>Enkephalins (δ-opioid receptor agonists)</u>			
Leu-enkephalin	Tyr-Gly- -Gly-Phe-Leu	6.6, 125.5, 3.65	(5, 8, 21)
Met-enkephalin	Tyr-Gly- -Gly-Phe-Met	9.2	(5, 21)
<u>Endomorphins (μ-opioid receptor agonists)</u>			
Endomorphin-1	Tyr-Pro- -Trp-Phe-NH ₂	5.00	(8)
Endomorphin-2	Tyr-Pro- -Phe-Phe-NH ₂	2.49	(8)
Human β -casomorphin	Tyr-Pro- -Phe-Val-Glu-Pro-Ile	0.56	(8)
<u>Dipeptidyl amides for assays</u>			
Standard DPP3 assay substrate	Arg-Arg- - β NA	-	(4)
	Arg-Arg- -NH-Mec	-	(22)

Table 2 Physiologically important DPP3 substrates. Cleavage site is indicated with a vertical line. K_i values were obtained from competitive substrate inhibition assays, measuring fluorescence in the hydrolysis of test substrates of Arg-Arg-amide type.

Most of the known non-peptide inhibitors of DPP3 are nonselective and non-specific. They comprise of general cysteine (4, 6, 23, 24), serine (22, 24-28), and aminopeptidase inhibitors (6, 23, 24), heavy metals (23-25, 29, 30) and metal chelating agents (4, 22-27, 29). Some general enkephalinase inhibitors have also been developed. Although some of them inhibit DPP3, they were mainly used for the inhibition of aminopeptidase N and neprilysin (31). Apart from these, a number of peptide inhibitors have been developed against enkephalinases (including DPP3) (Table 3). Spinorphin, found in bovine spinal cord, was characterized as a potent peptide inhibitor of enkephalin degrading peptides (32). Inspired by the potency of spinorphin in inhibition of enkephalinases, research was performed in order to find spinorphin/haemorphin derivatives that are specifically inhibiting DPP3. Subsequent efforts of designing inhibitors against DPP3 led to the discovery of further peptide derivatives like tynorphin and tynorphin-related pentapeptides. However, it was later observed that these

compounds are rather slow substrates than inhibitors of DPP3, getting degraded by the enzyme over a period of time (9, 33).

Competitive peptide inhibitor	AA composition	Activity (K_i , μM)	Reference
Spinorphin (VVYPWT)	Leu-Val- Val-Tyr-Pro-Trp-Thr	6.67, 2.42	(9, 33)
Tynorphin (VVYPW)	Val-Val- Tyr-Pro-Trp	2.67, 0.075	(9, 33)
LVYPW	Leu-Val- Tyr-Pro-Trp	1.35	(9)
YVYPW	Tyr-Val- Tyr-Pro-Trp	0.42	(9)
FVYPW	Phe-Val- Tyr-Pro-Trp	0.28	(9)
WVYPW	Trp-Val- Tyr-Pro-Trp	0.24	(9)
IVYPW	Ile-Val- Tyr-Pro-Trp	0.16	(9)
Valorphin (VVYPWTQ)	Val-Val- Tyr-Pro-Trp-Thr-Gln	0.049	(8)

Table 3 Haemorphin/Spinorphin derived peptide inhibitors of DPP3. Cleavage site is indicated with a vertical line. The affinity was quantified indirectly from competitive substrate inhibition, measuring fluorescence in the hydrolysis of standard test substrates of Arg-Arg-amide type. Rat DPP3 was used for all assays.

Pathophysiological implications of DPP3

DPP3 in pain modulation

Enkephalins are naturally occurring opioid-like peptides which resemble morphine structurally. Enkephalinergic cells of the neuroendocrine system synthesize enkephalins and they elicit pain killing or opiate activity upon binding to δ -opioid receptors. It was reported that DPP3 is co-localized with enkephalinergic neurons at the synaptic membrane localization of mice brain (9). DPP3 can preferably hydrolyse enkephalins at physiological pH thereby suggesting the involvement of this peptidase in pain modulation (5). Endomorphins (EM-1 and EM-2) are another class of endogenous opioid peptides whose turnover can be altered by DPP3 (8). Endomorphins reduce the perception of pain by specifically binding G-protein coupled μ -opioid receptors with high affinity. They are widely distributed in the mammalian central nervous system, especially in the brain, and have also been detected in spleen, thymus, blood plasma, immune cells and pituitary gland. This implicates that DPP3 can potently modulate perception of pain, stress and complex functions such as reward, arousal and vigilance. This was supported by a study showing that DPP3 activity for human CSF in

patients with acute pain was significantly lower compared with that in patients without pain (10). In addition, it was observed that the expression of DPP3 is downregulated in cortical lipid rafts of the 3xTgAD murine model of Alzheimer's disease, in comparison to the wild-type control (34). This implicates its involvement in the pathogenesis of this disease and other neurodegenerative disorders.

DPP3 in oxidative stress

Transcription factor Nrf2 or NF-E2 (Nuclear Factor Erythroid-derived 2) related factor 2 is a basic leucine zipper protein. Under basal cellular conditions, Nrf2 amount and activity are maintained at low levels through ubiquitin-dependent proteasomal degradation upon binding to an ubiquitin ligase called Keap1 (Kelch-like ECH-associated protein 1). An amino-terminal DLG and ETGE motif within Nrf2 is responsible for the association of the transcription factor to Keap1. In the events of high cellular oxidative stress, modification of reactive cysteines within Keap1 induces a conformational change, thus making the position of Nrf2 unfavourable for ubiquitination. Under such circumstances, Nrf2 translocates to the nucleus where it activates transcription of genes encoding for phase II detoxifying enzymes like NAD(P)H:quinone oxidoreductase 1 (NQO1). It was reported that DPP3 harbours the similar ETGE motif and as a consequence, competes to bind with Keap1, thereby resulting in a continuous nuclear migration of Nrf2 (11). This condition has been reported in neuroblastoma cells (IMR-32 cells) in response to overexpression of DPP3. It was also found that DPP3 overexpression efficiently attenuates the toxic effects of H₂O₂ and rotenone, demonstrating the cytoprotective effect of DPP3 against oxidative stress (35). Expression of DPP3 has been reported to increase with the histological aggressiveness of human ovarian primary carcinomas (7). In ovarian cancer cells tumor induced release of H₂O₂ transcriptionally upregulates the expression of Ets-1, a critical regulator of DPP3 expression (36, 37). A recent proteomic analysis of Keap1 interaction network and comparison to genomic profiles of 178 squamous cell lung carcinomas revealed amplification and mRNA overexpression of the DPP3 gene in tumors with high Nrf2 activity (11). The findings support that DPP3 modulates the Keap1-Nrf2 pathway, which is responsible for maintaining the redox homeostasis in the cell.

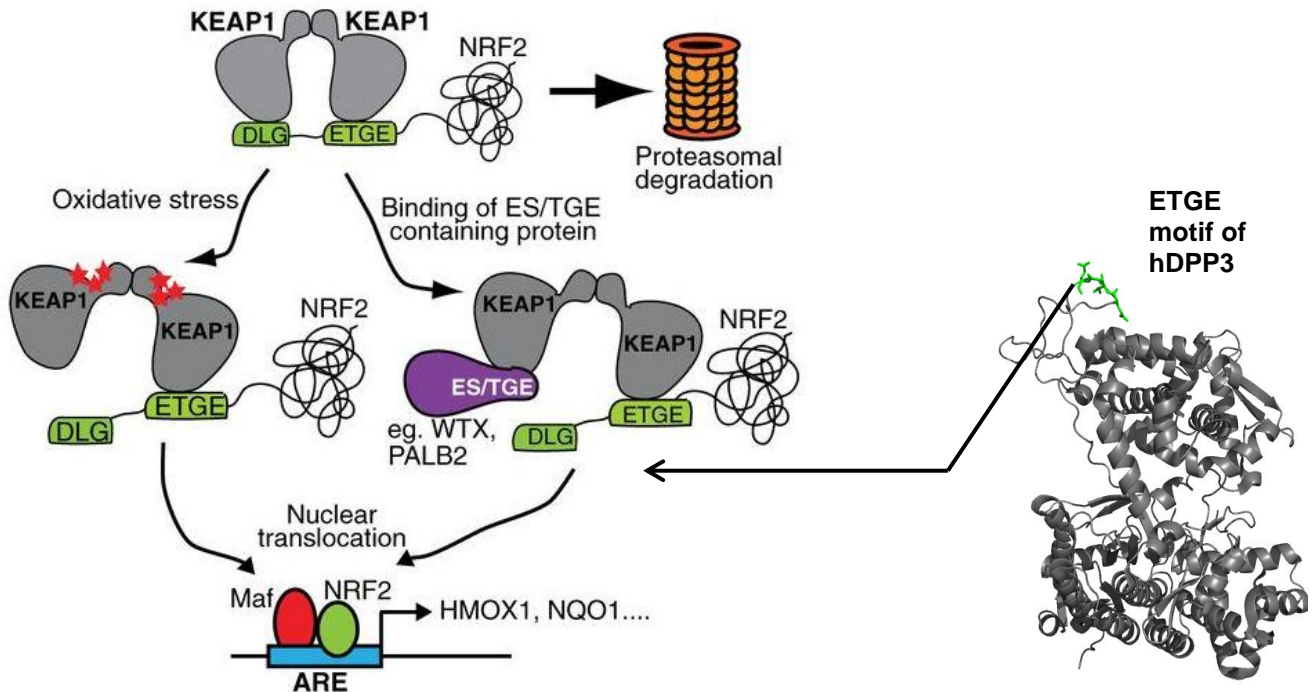


Figure 4 Regulation of the Keap1-Nrf2 pathway by DPP3 (Adapted from (11))

DPP3 in the renin-angiotensin system (RAS)

There are increasing evidences suggesting a strong role of DPP3 in regulation of the RAS. Angiotensins (Ang) are the key peptide players of the rennin– angiotensin system (RAS) and have vasoactive properties. Ang II is the major effector of the classical RAS pathway which plays a critical role in hypertension. Although the functions of RAS are distinct within different tissues, the kidney is the primary target for Ang II, where it regulates fluid content and blood pressure. Ang II directly stimulates the reabsorption of sodium along the nephron and increases constriction of the renal vasculature to reduce the filtration rate. Ang II also stimulates the release of anti-diuretic hormone (ADH or vasopressin) extra-renally from the pituitary gland to cause increased water reabsorption in the collecting duct of the kidneys, and stimulates the release of aldosterone. These events relayed by Ang II result in increased Na^+ reabsorption, blood volume and blood pressure (38). In addition, Ang II has also been known to mediate reactive oxygen species (ROS) production, contributing to cellular oxidative stress (39).

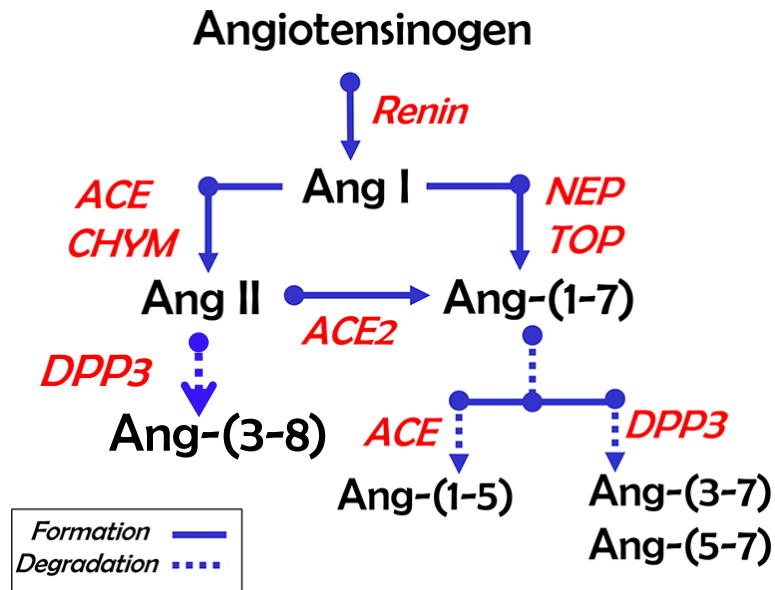


Figure 5 Regulation of the RAS pathway by DPP3 (adapted from (40))

DPP3 has been demonstrated to have especially high activity towards Ang II which suggests its involvement in the RAS. High DPP3 activity in blood plasma was shown to scavenge Ang II, III and IV, with a plausible blood pressure lowering effect. Interestingly, dipeptides released by DPP III mediated hydrolysis of its substrates are inhibitory to angiotensin-converting enzyme (41, 42). Recent transcriptomic analysis has revealed that DPP3 is one of the Ang-metabolizing enzymes upregulated in human atheroma (43).

References

1. Rawlings ND, Barrett AJ. Peptidases. In: eLS. American Cancer Society; 2014.
2. Cerdà Costa N, Xavier Gomis R, Rüth F. Architecture and function of metallopeptidase catalytic domains. *Protein Science*. 2014 Feb;23(2):123-44.
3. Pathophysiological Implications of Dipeptidyl Peptidases [Internet].; 2017 [updated /07/31; cited Oct 19, 2018]. Available from: <http://www.eurekaselect.com/151178/article>.
4. Ellis S, Nuenke JM. Dipeptidyl arylamidase III of the pituitary. Purification and characterization. *J Biol Chem*. 1967 Oct 25;242(20):4623-9.
5. Lee CM, Snyder SH. Dipeptidyl-aminopeptidase III of rat brain. Selective affinity for enkephalin and angiotensin. *J Biol Chem*. 1982 Oct 25;257(20):12043-50.
6. Abramić M, Zubanović M, Vitale L. Dipeptidyl peptidase III from human erythrocytes. *Biol Chem Hoppe-Seyler*. 1988 Jan;369(1):29-38.
7. Simaga S, Babić D, Osmak M, Ilić-Forko J, Vitale L, Milčić D, et al. Dipeptidyl peptidase III in malignant and non-malignant gynaecological tissue. *Eur J Cancer*. 1998 Feb;34(3):399-405.
8. Barsun M, Jajcanin N, Vukelić B, Spoljarić J, Abramić M. Human dipeptidyl peptidase III acts as a post-proline-cleaving enzyme on endomorphins. *Biol Chem*. 2007 Mar;388(3):343-8.
9. Chiba T, Li Y, Yamane T, Ogikubo O, Fukuoka M, Arai R, et al. Inhibition of recombinant dipeptidyl peptidase III by synthetic hemorphin-like peptides. *Peptides*. 2003 May;24(5):773-8.
10. Sato H, Kimura K, Yamamoto Y, Hazato T. [Activity of DPP III in human cerebrospinal fluid derived from patients with pain]. *Masui*. 2003 Mar;52(3):257-63.
11. Hast BE, Goldfarb D, Mulvaney KM, Hast MA, Siesser PF, Yan F, et al. Proteomic analysis of ubiquitin ligase KEAP1 reveals associated proteins that inhibit NRF2 ubiquitination. *Cancer Res*. 2013 Apr 01;73(7):2199-210.
12. Lu K, Alcivar AL, Ma J, Foo TK, Zywea S, Mahdi A, et al. NRF2 Induction Supporting Breast Cancer Cell Survival Is Enabled by Oxidative Stress-Induced DPP3-KEAP1 Interaction. *Cancer Res*. 2017 06 01;77(11):2881-92.
13. Local Angiotensin Pathways in Human Carotid Atheroma: Towards a Systems Biology Approach [Internet].: Hindawi; 2015 [cited Oct 19, 2018]. Available from: <https://www.hindawi.com/journals/cpis/2015/593086/>.
14. Cruz-Diaz N, Wilson BA, Pirro NT, Brosnihan KB, Marshall AC, Chappell MC. Identification of dipeptidyl peptidase 3 as the Angiotensin-(1-7) degrading peptidase in human HK-2 renal epithelial cells. *Peptides*. 2016 -9;83:29-37.

15. Baral PK, Jajcanin-Jozić N, Deller S, Macheroux P, Abramić M, Gruber K. The first structure of dipeptidyl-peptidase III provides insight into the catalytic mechanism and mode of substrate binding. *J Biol Chem*. 2008 Aug 08;283(32):22316-24.
16. Bezerra GA, Dobrovetsky E, Viertlmayr R, Dong A, Binter A, Abramić M, et al. Entropy-driven binding of opioid peptides induces a large domain motion in human dipeptidyl peptidase III. *PNAS*. 2012 -04-24 00:00:00;109(17):6525-30.
17. Sabljic I, Meštrović N, Vukelić B, Macheroux P, Gruber K, Luić M, et al. Crystal structure of dipeptidyl peptidase III from the human gut symbiont *Bacteroides thetaiotaomicron*. *PLoS ONE*. 2017;12(11):e0187295.
18. Matthews BW. Thermolysin. In: *Handbook of Metalloproteins*. American Cancer Society; 2006.
19. Dale GE, Oefner C. Neprilysin. In: *Encyclopedia of Inorganic and Bioinorganic Chemistry*. American Cancer Society; 2011.
20. Kumar P, Reithofer V, Reisinger M, Wallner S, Pavkov-Keller T, Macheroux P, et al. Substrate complexes of human dipeptidyl peptidase III reveal the mechanism of enzyme inhibition. *Scientific reports*. 2016 Mar 30;6(1):10.
21. Abramić M, Zubanović M, Vitale L. Dipeptidyl peptidase III from human erythrocytes. *Biol Chem Hoppe-Seyler*. 1988 Jan;369(1):29-38.
22. Smyth M, O'Cuinn G. Dipeptidyl Aminopeptidase III of Guinea-Pig Brain: Specificity for Short Oligopeptide Sequences. *Journal of Neurochemistry*. 1994 -10-01;63(4):1439-45.
23. Ohkubo I, Li Y, Maeda T, Yamamoto Y, Yamane T, Du PG, et al. Molecular cloning and immunohistochemical localization of rat dipeptidyl peptidase III. *Forensic Sci Int*. 2000 Sep 11;113(1-3):147-51.
24. Abramić M, Schleuder D, Dolovcak L, Schröder W, Strupat K, Sagi D, et al. Human and rat dipeptidyl peptidase III: biochemical and mass spectrometric arguments for similarities and differences. *Biol Chem*. 2000 Dec;381(12):1233-43.
25. Vanha-Perttula T. Dipeptidyl peptidase III and alanyl aminopeptidase in the human seminal plasma: origin and biochemical properties. *Clin Chim Acta*. 1988 Oct 14;177(2):179-95.
26. Dhanda S, Singh H, Singh J, Singh TP. Isolation, purification and characterization of a DPP-III homologue from goat brain. *Protein Expr Purif*. 2007 Apr;52(2):297-305.
27. Fukasawa K, Fukasawa KM, Kanai M, Fujii S, Hirose J, Harada M. Dipeptidyl peptidase III is a zinc metallo-exopeptidase. Molecular cloning and expression. *The Biochemical journal*. 1998 Jan 15;329 (Pt 2)(2):275-82.
28. Lynn KR. The isolation and some properties of dipeptidyl peptidases II and III from porcine spleen. *Int J Biochem*. 1991;23(1):47-50.

29. Mazzocco C, Fukasawa KM, Auguste P, Puiroux J. Characterization of a functionally expressed dipeptidyl aminopeptidase III from *Drosophila melanogaster*. *Eur J Biochem*. 2003 Jul;270(14):3074-82.
30. Shimamori Y, Watanabe Y, Fujimoto Y. Purification and characterization of dipeptidyl aminopeptidase III from human placenta. *Chem Pharm Bull*. 1986 Aug;34(8):3333-40.
31. Thanawala V, Kadam VJ, Ghosh R. Enkephalinase inhibitors: potential agents for the management of pain. *Curr Drug Targets*. 2008 Oct;9(10):887-94.
32. Honda M, Okutsu H, Matsuura T, Miyagi T, Yamamoto Y, Hazato T, et al. Spinorphin, an endogenous inhibitor of enkephalin-degrading enzymes, potentiates leu-enkephalin-induced anti-allodynic and antinociceptive effects in mice. *Jpn J Pharmacol*. 2001 Dec;87(4):261-7.
33. Yamamoto Y, Hashimoto J, Shimamura M, Yamaguchi T, Hazato T. Characterization of tynorphin, a potent endogenous inhibitor of dipeptidyl peptidase III. *Peptides*. 2000 Apr;21(4):503-8.
34. Chadwick W, Brennehan R, Martin B, Maudsley S. Complex and multidimensional lipid raft alterations in a murine model of Alzheimer's disease. *Int J Alzheimers Dis*. 2010 Dec 02;2010:604792.
35. Liu Y, Kern JT, Walker JR, Johnson JA, Schultz PG, Luesch H. A genomic screen for activators of the antioxidant response element. *Proc Natl Acad Sci U S A*. 2007 Mar 20;104(12):5205-10.
36. Wilson LA, Gemin A, Espiritu R, Singh G. ets-1 is transcriptionally up-regulated by H₂O₂ via an antioxidant response element. *FASEB J*. 2005 Dec;19(14):2085-7.
37. Shukla AA, Jain M, Chauhan SS. Ets-1/Elk-1 is a critical mediator of dipeptidyl-peptidase III transcription in human glioblastoma cells. *FEBS J*. 2010 Apr;277(8):1861-75.
38. Crowley SD, Gurley SB, Herrera MJ, Ruiz P, Griffiths R, Kumar AP, et al. Angiotensin II causes hypertension and cardiac hypertrophy through its receptors in the kidney. *Proc Natl Acad Sci U S A*. 2006 Nov 21;103(47):17985-90.
39. Su-Mi Kim, Yang-Gyun Kim, Kyung-Hwan Jeong, Sang-Ho Lee, Tae-Won Lee, Chun-Gyoo Ihm, et al. Angiotensin II-Induced Mitochondrial Nox4 Is a Major Endogenous Source of Oxidative Stress in Kidney Tubular Cells. *PLoS One*. 2012 Jul 1;7(7):e39739.
40. Cruz-Diaz N, Wilson BA, Chappell MC. Peptidases and the Renin-Angiotensin System: The Alternative Angiotensin-(1-7) Cascade. *Enzyme Inhibitors and Activators*. 2017.
41. Sentandreu MA, Toldrà Vilardell F. Generation of ACE inhibitory dipeptides by pork muscle dipeptidyl peptidases I and III. 2005 Aug 7,.
42. Allard M, Simonnet G, Dupouy B, Vincent JD. Angiotensin II inactivation process in cultured mouse spinal cord cells. *J Neurochem*. 1987 May;48(5):1553-9.

43. Nehme A, Cerutti C, Zibara K. Transcriptomic Analysis Reveals Novel Transcription Factors Associated With Renin-Angiotensin-Aldosterone System in Human Atheroma. *Hypertension*. 2016 12;68(6):1375-84.

Chapter 2

Knock-out of DPP3 in mice unravel its involvement in the metabolic regulation of the renin-angiotensin system

Knock-out of DPP3 in mice unravel its involvement in the metabolic regulation of the renin-angiotensin system

Shalinee Jha,¹ Ulrike Taschler,² Oliver Domenig,³ Marko Poglitsch,³ Benjamin Bourgeois,⁴ Tobias Madl,⁴ Karl Gruber,² Rolf Breinbauer,⁴ Robert Zimmermann,² and Peter Macheroux¹

¹Institute of Biochemistry, Graz University of Technology, Austria

²Institute of Molecular Biosciences, University of Graz, Austria

³Attoquant Diagnostics GmbH, Austria

⁴Institute of Molecular Biology and Biochemistry, Medical University of Graz, Austria

⁴Institute of Organic Chemistry, Graz University of Technology, Austria

Author contributions

P.M. initiated the project; P.M., R.Z., K.G., R.B., T.M., M.P., S.J., and U.T. designed research; S.J., U.T., O.D., B.B., and M.P. performed research; S.J., U.T., O.D., M.P., B.B., and T.M. analyzed data and interpreted experimental results; S.J., U.T., and P.M. wrote the manuscript.

Keywords: Dipeptidyl peptidase 3, knockout mice, Renin-angiotensin system, Angiotensin II, oxidative stress

Abbreviations:

DPP3, Dipeptidyl Peptidase-3; WT, Wild-type; RAS, Renin-Angiotensin Pathway; Ang II, Angiotensin II; Ang 1-7, Angiotensin 1-7; TCA, Tricarboxylic acid; NAD⁺, Oxidized nicotinamide adenine dinucleotide; ROS, Reactive oxygen species; LC-MS/MS, Liquid Chromatography-tandem Mass Spectrometry; NMR, Nuclear Magnetic Resonance; PCA, Principal Component analysis; OPLS-DA, Orthogonal Projections to Latent Structures Discriminant Analysis; SIRT3, Sirtuin-3; PARP, Poly (ADP-ribose) polymerase; NAMPT, Nicotinamide phosphoribosyltransferase

Abstract

DPP3 is a zinc-dependent hydrolase involved in degrading oligopeptides with 4–12 amino acid residues. It has been associated with several pathophysiological processes, including blood pressure regulation, pain signaling and enhancement of cancer cell defense against oxidative stress. An important objective is to identify the cellular pathways that are potentially targeted by DPP3 to mediate these effects. Here, we investigated the impact of DPP3 deficiency on metabolic behavior and susceptibility to oxidative stress in mice. Mice lacking the gene encoding for DPP3 (DPP3^{-/-}) exhibited significant weight loss, impaired cellular metabolism and aggravated renal oxidative stress in comparison to the WT mice when fed on a regular chow diet. Additionally, pair-feeding and indirect calorimetry measurements revealed that the DPP3^{-/-} mice have higher water intake and increased energy expenditure. LC-MS based profiling of angiotensin peptides indicate that elevated levels of hypertensive hormone angiotensin II (Ang II) and a concurrent increase in the production of cellular reactive oxygen species (ROS) accounted for the oxidative damage in DPP3^{-/-} mice. Furthermore, we observed that NAD⁺, a cofactor which plays a pivotal role in the regulation of stress resistance and cell repair, to be depleted in the DPP3^{-/-} mice, while NAD⁺ precursors nicotinamide and nicotinamide riboside are augmented. This metabolic response suggest that the DPP3^{-/-} mice resort to the compensatory salvage pathway of NAD⁺ biosynthesis to enhance energy metabolism and evade cell death. Taken together, these observations demonstrate that deletion of DPP3 gene has a profound impact on energy homeostasis. It also validates that DPP3 regulates the RAS pathway by orchestrating the Ang II-induced ROS generation. This is mostly found upstream of several cardiovascular and renal disorders and can be exploited as a potential therapeutic intervention.

Introduction

The renin-angiotensin system (RAS) plays a pivotal role in pathophysiological modulation of renal and cardiovascular processes (1, 2). Angiotensin II (Ang II) is the principal effector of the RAS and is responsible for maintaining homeostasis in the heart and kidney (3). In addition, Ang II is a potent stimulator of NAD(P)H oxidase, which augments formation of reactive oxygen species (ROS) in various tissues. Ang II-mediated ROS production has been associated to cell growth, apoptosis, cell migration and expression of inflammatory and extracellular matrix genes (4). An imbalance between the production of ROS and the antioxidant defenses to eliminate these toxic intermediates leads to oxidative stress. There is a plethora of evidence demonstrating the importance of oxidative stress in Ang II-induced metabolic disorders like hypertension, diabetes mellitus and chronic kidney disease (5-8). Although blockade of the RAS is the most commonly adopted strategy to slow progression of cardiovascular and associated renal diseases, a better understanding of the novel aspects of the RAS is of paramount importance for the development of innovative therapies that target pathologies inflicted by anomalies of this pathway.

Dipeptidyl peptidase 3 (DPP3) is a metalloprotease that specifically cleaves dipeptides at the N-terminus. A variety of small peptides, such as Met-enkephalin and angiotensin (I and II), are targets of the enzyme although the full range of substrate peptides remains undefined (9). In addition, DPP3 exhibits a moonlighting activity in the Keap1-Nrf2 signaling pathway, which plays a crucial role in stress responses through transcriptional regulation of the antioxidant response element (10). Despite this intriguing involvement of DPP3 in peptide processing and signaling as well as the response to oxygen stress, its physiological role and potential involvement in disease-related processes is currently unknown. DPP3 is part of the central human proteome, *i.e.* it belongs to a set of proteins ubiquitously and abundantly expressed in all human cells. This suggests that the enzyme exerts a general as well as tissue-specific role, *i.e.* it may affect the levels of some peptides in the whole organism and, equally, of peptides confined to certain cells. Recently, it was reported that DPP3 administration to Ang II-induced hypertensive mice could significantly diminish systolic blood pressure, cardiac hypertrophy, and myocardial fibrosis in an extent at par with the effect of the angiotensin receptor blocker candesartan. It was also observed that DPP3 effectively reduced urine albumin excretion, kidney damage, and the renal protein levels of the pro-inflammatory molecule monocyte chemo-attractant protein-1 and the pro-coagulant platelet activator inhibitor (11). Taken together, the enzyme's ability to degrade various bioactive peptides,

DPP3-deficiency may have complex effects and influence basic physiological processes, such as blood pressure and renal function. Yet, the precise molecular mechanisms contributing to the cardio- and renoprotective role of DPP3 *in vivo* is not fully characterized. To address this lacuna, we developed DPP3 knockout mice. Evaluation of DPP3^{-/-} mice revealed pertinent metabolic deficits arising due to the absence of this enzyme.

Results

Generation of DPP3 knockout mice

To investigate the *in vivo* function of the *dpp3*, we targeted the *dpp3* gene in mice by replacing exon 6 and neomycin cassette with a lacZ reporter gene. This targeting construct was aimed at creating a frame-shift that would knockout the *dpp3* gene (Figure 1A). The absence of *dpp3* was verified by tail-tip PCR genotyping. Western blotting confirmed the absence of DPP3 protein (Figure 1B). A comparison of DPP3 activity in various tissues taken from WT mice control and the DPP3^{-/-} mice clearly demonstrated the absence of DPP3 activity in the knockouts (Figure 1C).

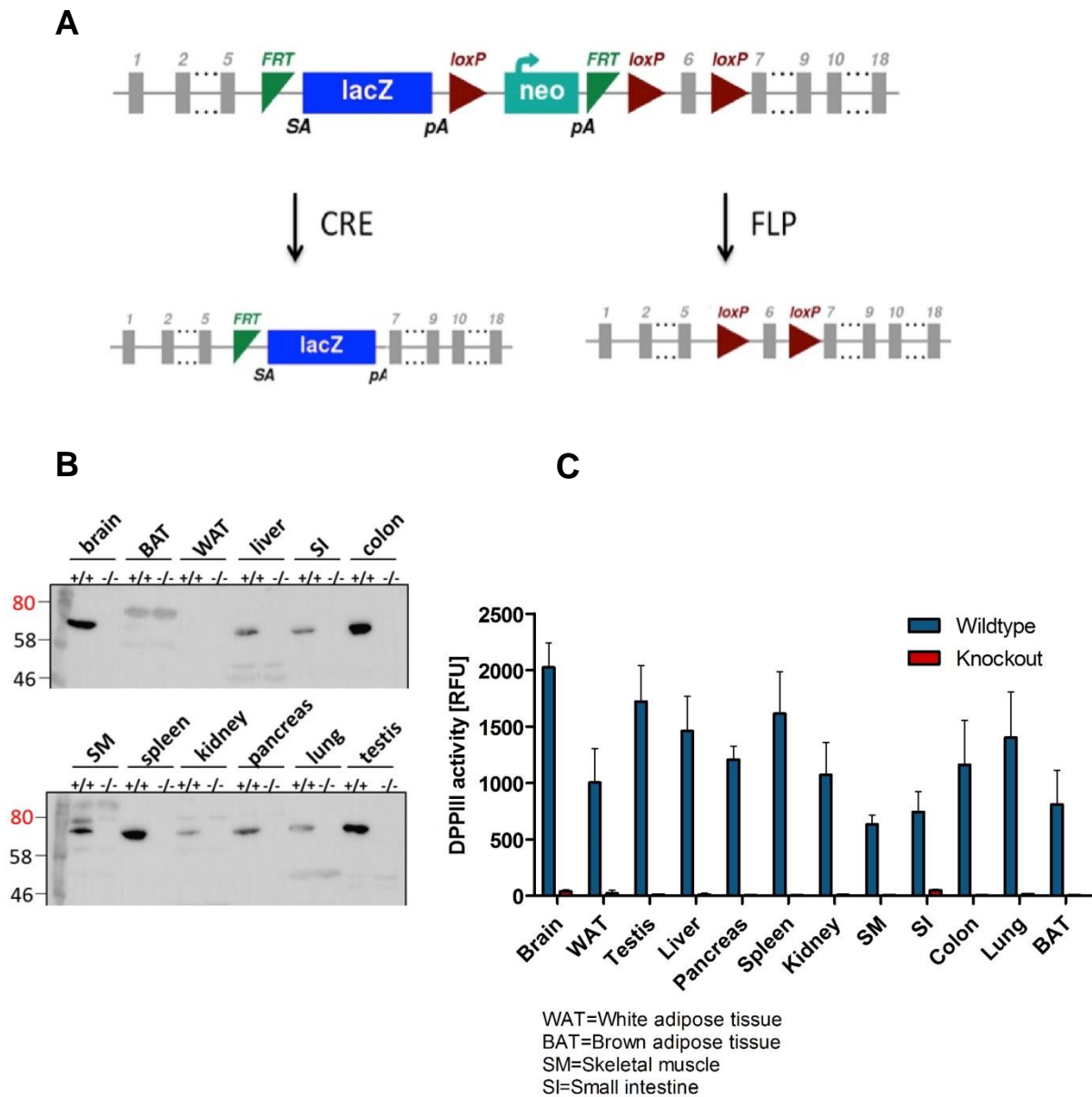


Figure 1 Generation of DPP3 knockout mice. Strategy for the generation of *dpp3*-knockout mice (A), Demonstration of the lack of DPP3 in *dpp3*-knockout mice (-/-). Panel B shows a Western blot and panel C demonstrates activity assays using Arg-Arg-naphthylamide as an artificial substrate (BAT = brown adipose tissue; SI = small intestine; SM = skeletal muscle; WAT = white adipose tissue).

DPP3 deficiency leads to changes in metabolic behavior

Chow-fed DPP3^{-/-} mice weighed less (Figure 2A) and accumulated less fat mass than DPP3^{+/+} litter-mates (Figure 2B), despite eating significantly more during the active dark phase (Figure 2C). During indirect calorimetry, DPP3^{-/-} mice consumed more O₂ and produced more CO₂ (Figure 2D), suggestive of higher energy expenditure (EE). Resting EE was not different, indicating that the increase was prominently because of changes at night, when the mice are most active. In addition, the respiratory quotient was also higher in DPP3^{-/-} mice during the dark phase, indicating enhanced glucose oxidation during the feeding period. Under basal conditions, with free access to drinking water, DPP3^{-/-} mice exhibited pronounced polydipsia with significantly greater fluid consumption (Figure 2E) in comparison to the WT control mice.

DPP3 acts as a modulator of the RAS

The Renin-Angiotensin-System (RAS) is critically involved in the regulation of cardiovascular and renal function. The peptide hormone system comprises of multiple enzymes, giving rise to a network of effector peptides. The angiotensin peptides bind to their specific receptors to ultimately elicit an integrated physiological response (2). Ang II, a crucial component of the classical RAS pathway, is a potent vasoconstrictor, thereby responsible for regulating blood pressure. It is a powerful dipsogenic and modulates salt and fluid homeostasis (12). The excessive thirst demonstrated by DPP3^{-/-} mice during the metabolic cage studies prompted us to perform a detailed analysis of RAS and measure circulating angiotensin levels. We generated a serum “RAS-fingerprint” for 10 different angiotensin peptides using ultra-pressure-liquid chromatography-tandem mass spectrometry (LC-MS/MS). Serum derived from pair-fed mice revealed that the DPP3^{-/-} animals had higher concentrations of virtually all the angiotensins (Figure 3), except Ang 1-7. Importantly, Serum Ang II levels were drastically elevated in the DPP3^{-/-} mice. Ang 1-7, which is the main metabolite of the alternate RAS pathway, is also not altered in the knockouts. It has already been established that Ang 1-7 is an important modulator of the RAS and acts as a physiologic

antagonist of angiotensin II having vasodilatory and antihypertensive properties (13). These results indicate knocking out DPP3 has an influence on the overall RAS activity.

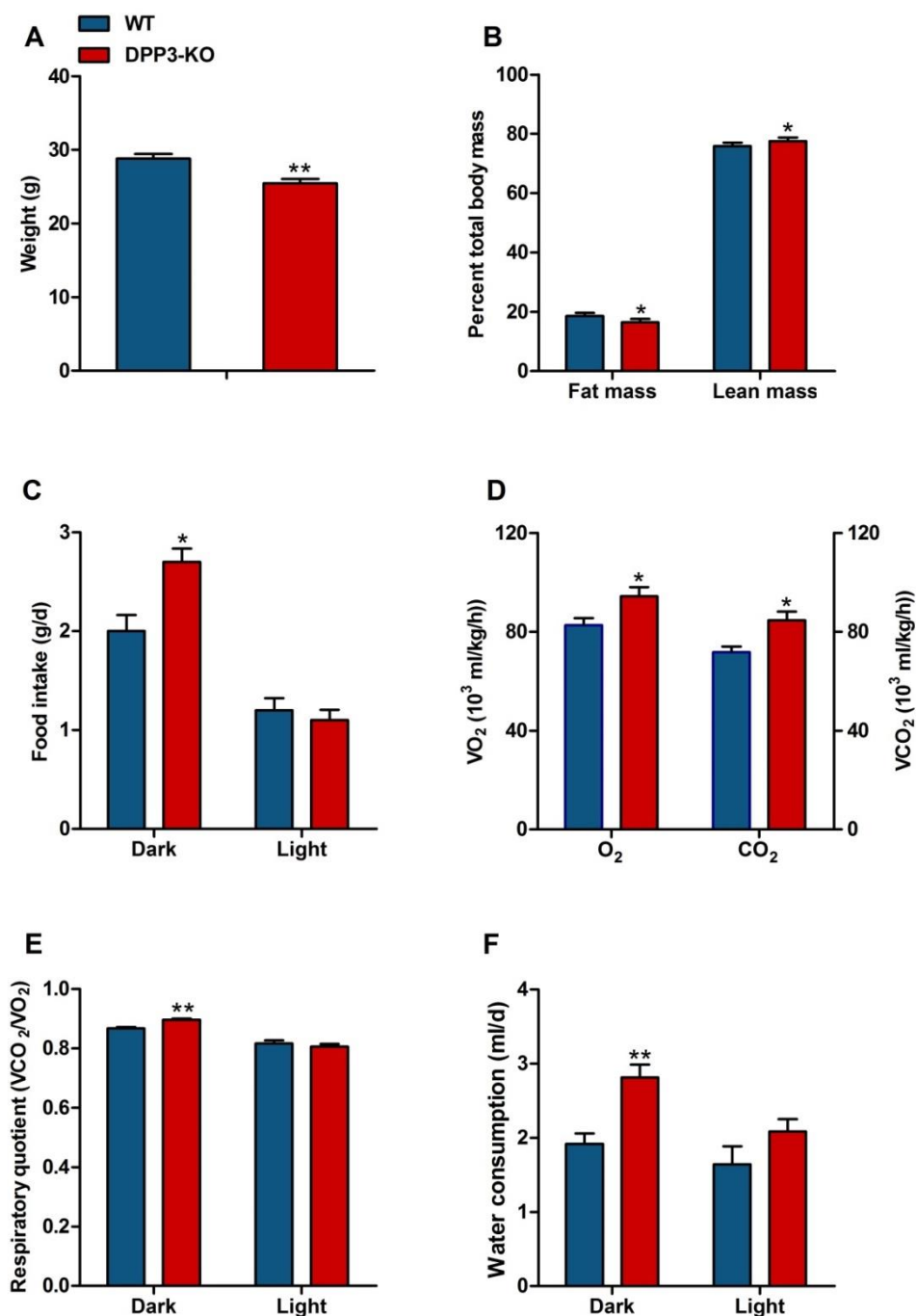
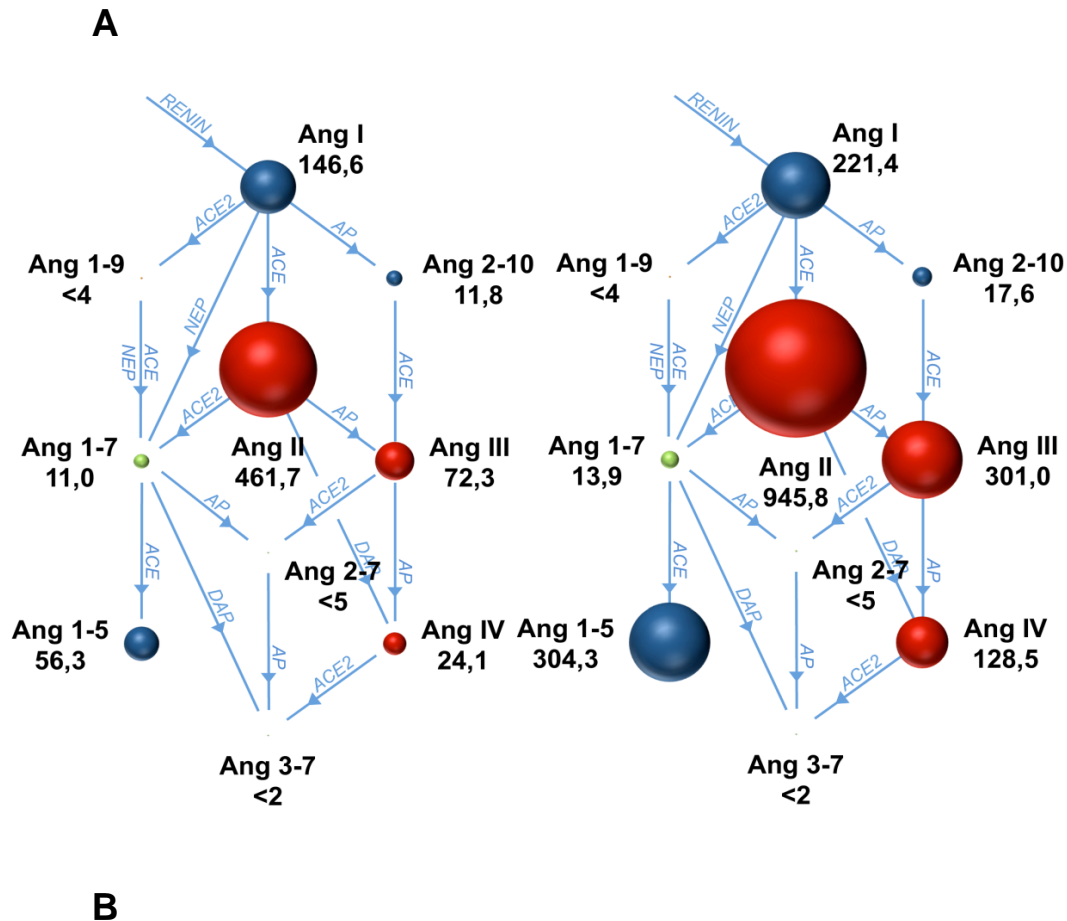


Figure 2 Comparison of Body weight, body composition and metabolic parameters of DPP3-knockout and WT control mice. Body weight (A) and body composition (B) of 12-16 weeks old male mice fed with the regular chow diet (n=6/group). Mean food intake (C), oxygen consumption and carbon-dioxide production (D), respiratory quotient (E), and Mean total

water consumption (*F*) was measured in metabolic cages over the light and dark phases in *DPP3*^{-/-} (*DPP3*-KO) and *DPP3*^{+/+} (wildtype) male mice (12-16 weeks of age; *n*=6/group) fed with the regular chow diet. **p*<0.05, ***p*<0.01, ****p*<0.001 versus WT mice based on unpaired two-sided Student's *t*-test. Data represents mean ± SEM.



RAS-Fingerprint (Plasma Equilibrium) (Angiotensin levels in pg/ml)										
	Ang II (1-8)	Ang (1-7)	Ang (1-9)	Ang I (1-10)	Ang III (2-8)	Ang (3-7)	Ang (1-5)	Ang IV (3-8)	Ang (2-7)	Ang (2-10)
WT	461.7	11.0	<4	146.6	72.3	<2	56.3	24.1	<5	11.8
DPP3-KO	945.8**	13.9	<4	221.4*	301.0***	<2	304.3***	128.5***	<5	17.6

Figure 3 Effect of *DPP3* knockout on serum angiotensin levels. RAS peptides in serum measured by liquid chromatography-mass spectrometry in *DPP3*^{-/-} (*DPP3*-KO) and *DPP3*^{+/+} (WT) male mice (*n* = 8/group). Panel A shows RAS peptides in serum. Diameter of spheres reflects the mean concentration of the respective peptides in serum from WT control (left) and *DPP3*^{-/-} mice (right). Peptide levels (pg/ml) are provided next to each sphere. The amino acid

*sequence annotation of each angiotensin metabolite is based on the decapeptide Ang I (1-10) that is cleaved by the proteases (blue arrows) connecting their substrates and products (AP, aminopeptidases; NEP, neutral endopeptidase; DAP, di-aminopeptidase; ACE, angiotensin converting enzyme; ACE2, angiotensin converting enzyme 2). Table in panel B shows means values for serum level of various angiotensin peptides. * $p < 0.05$, ** $p < 0.01$, *** $p < 0.001$ versus WT mice based on unpaired two-sided Student's *t*-test. Data represents mean \pm SEM.*

Loss of DPP3 represses the flux through the TCA cycle

Urine metabolites are indicative of whole body metabolism, and NMR-based metabolomics on urine has previously been used to investigate endogenous markers in patho-physiological conditions (14-18). To further elucidate how DPP3 deletion could induce a phenotype with augmented water consumption, we utilized an explorative analysis of the urine by ^1H NMR spectroscopy using supervised OPLS-DA between the DPP3^{-/-} and DPP3^{+/+} reference. A color-coded OPLS-DA coefficient plot was used to investigate the difference in the metabolite profile between the two groups. In the plot, negative peaks indicate lower metabolite levels in the urine of the DPP3^{-/-} mice compared to the WT mice, while positive peaks indicate higher metabolite levels. The urine from DPP3^{-/-} mice contained lower concentrations of three TCA cycle intermediates- citrate, succinate and 2-oxoglutarate, when compared to their control WT counterparts (Figure 4A, Table 1). This is consistent with our observation of increased glucose oxidation by DPP3^{-/-} mice in the metabolic cage as excess glucose can cause repression of TCA cycle genes. In addition, the knockout mice also showed relatively lower levels of uremic toxins indoxyl sulfate and hippurate (Figure 4B, Table 1). Indoxyl sulfate is derived from the degradation of dietary tryptophan into indole by intestinal microbiota. Indole is then absorbed into the blood from the intestine, and is metabolized to indoxyl sulfate in the liver and is normally excreted into urine. Low renal clearance of indoxyl sulfate is suggestive of an increased risk of chronic kidney disease (CKD) progression and cardiovascular disease (CVD) development (19-22). Hippurate is an endogenous urinary metabolite and is commonly used as a measure of renal clearance (23). These data, when taken together, imply that loss of DPP3 leads to a metabolic block of the TCA cycle and insufficient removal of toxic metabolites.

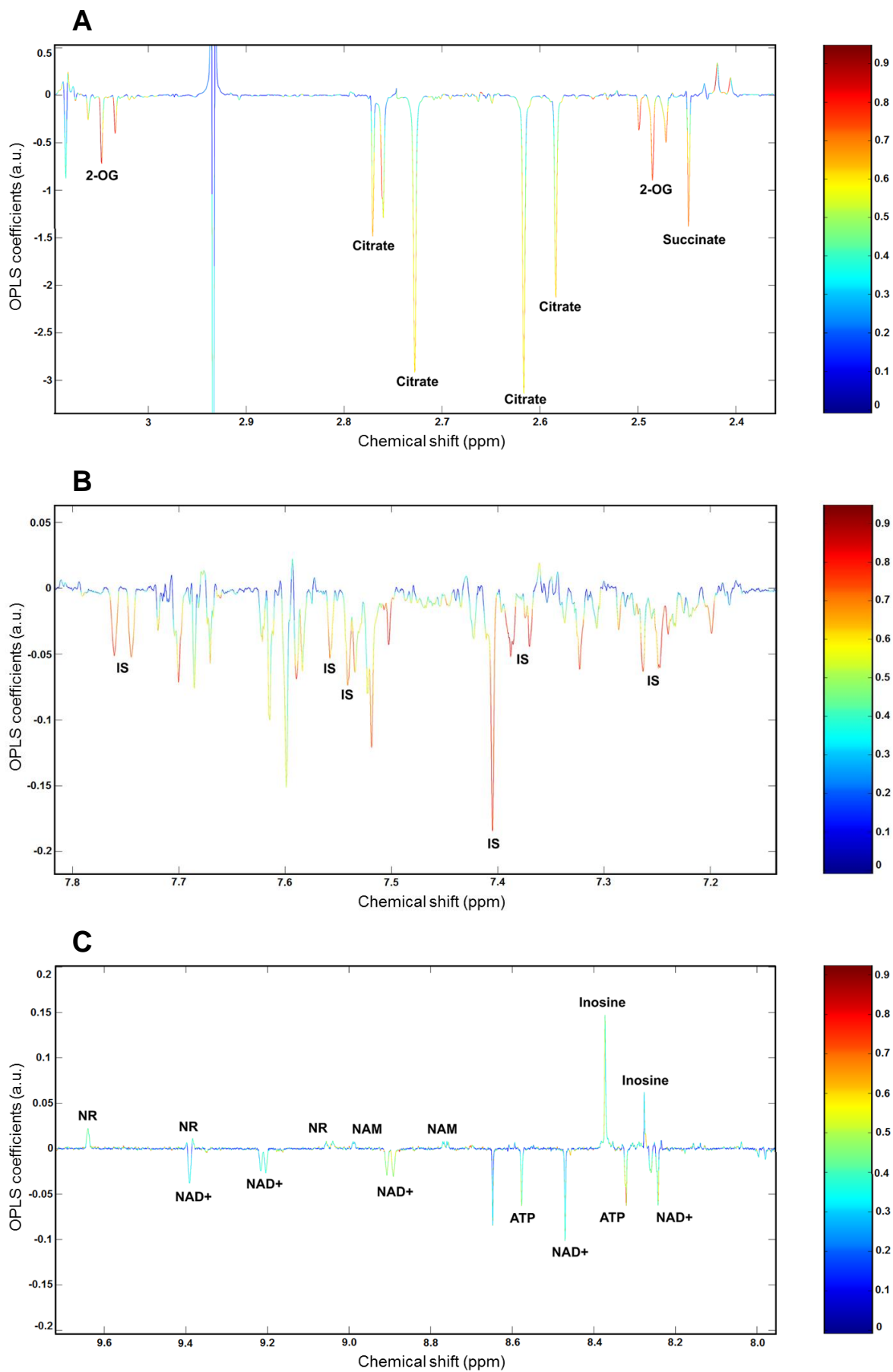


Figure 4 ^1H NMR spectra derived from DPP3 knockout and WT mice. OPLS-DA color-coded correlation coefficient loading plots of key metabolites in the urine (A and B) and kidneys (C), demonstrating discrimination of key metabolite levels between DPP3^{-/-} and DPP3^{+/+} (WT) male mice ($n = 6/\text{group}$). The color map shows the significance of metabolite variations between the two genotypes (significance increasing from blue towards red). The peaks in the positive direction indicate the metabolites that are more abundant in the DPP3^{-/-} mice, while the metabolites that are decreased in the DPP3^{-/-} mice compared to the WT control are presented as peaks in the negative direction. (Keys: 2-OG: 2-oxoglutarate; IS: indoxyl sulfate; NAD⁺: nicotinamide adenine dinucleotide; ATP: adenosine triphosphate; NAM: nicotinamide; NR: nicotinamide riboside)

DPP3^{-/-} mice have depleted NAD⁺ levels and activation of salvage pathway

Next, we sought to determine the effect of DPP3 deletion on the metabolite profile of kidney tissue in DPP3^{-/-} and DPP3^{+/+} mice. To examine intrinsic variations between the two data sets, PCA was initially performed using ^1H NMR data followed by an OPLS-DA model generation. The DPP3^{-/-} kidney samples were characterized by diminished levels of NAD⁺ and ATP. A concomitantly elevated level of NAD⁺ precursors like nicotinamide and nicotinamide-riboside was observed (Figure 4C, Table 1). These precursors are majorly responsible for replenishing cellular NAD⁺ through salvage pathway. NAD⁺ and its reduced form NADH are crucial molecules involved in energy generation through redox reactions in the TCA cycle (24). However, NAD⁺ is also a co-substrate in multiple antioxidant and repair enzymes such as sirtuins and PARP (25-29). We postulate that enhanced Ang II in the DPP3^{-/-} mice results in greater ROS production and therefore, increased oxidative stress in these animals. This activates the antioxidant enzymes leading to the consumption and thus depletion of cellular NAD⁺ pool. This is corroborated by the impeded TCA cycle and consequent reduction in the generation of ATP in the DPP3^{-/-} mice. We performed quantitative-PCR to compare the levels of detoxification enzymes SIRT3 and PARP, and of NAMPT, which catalyzes the rate limiting step of NAD⁺ salvage biosynthesis, in the kidneys of DPP3^{-/-} and DPP3^{+/+} mice. The DPP3^{-/-} mice displayed marginally higher levels of all these three enzymes; however the differences were not significant (data not shown).

Quantification of ¹ H NMR metabolites (Intensity; A.U.)		
Metabolites	DPP3 ^{+/+}	DPP3 ^{-/-}
<i>Urine</i>		
3-Indoxylsulfate	1.3 ± 0.2	0.7 ± 0.1**
Hippurate	1.6 ± 0.1	1.2 ± 0.1**
Citrate	18.1 ± 3.5	6.5 ± 2.6**
succinate	9.4 ± 1.3	5.2 ± 1.0*
2-oxoglutarate	4.7 ± 0.6	3.3 ± 1.7
<i>Kidney</i>		
NAD ⁺	0.35 ± 0.03	0.24 ± 0.04*
ATP	0.05 ± 0.01	0.04 ± 0.01
Nicotinamide	0.03 ± 0.0	0.04 ± 0.01
Nicotinamide-riboside	0.06 ± 0.02	0.11 ± 0.01*

Table 1 Quantification of ¹H NMR metabolites in the kidneys and urine of DPP3^{-/-} and DPP3^{+/+} (WT) male mice (n = 6/group). *p<0.05, **p<0.01, ***p<0.001 versus wildtype mice based on unpaired two-sided Student's t-test. Data represents mean ± SEM.

Inhibition of DPP3 enhances oxidative stress insult in mice

To further validate the occurrence of Ang II induced oxidative stress, we examined putative stress markers in the kidney tissue homogenates of DPP3^{-/-} and WT control mice. Ang II is known to promote ROS production, and so we determined the generation of reactive oxygen intermediates using 2',7'-dichlorodihydrofluorescein diacetate (H₂DCFDA). Abrogation of DPP3 function led to a significantly enhanced fluorescence signal from the ROS reporter dye H₂DCFDA in the knockout mice (Figure 5A). Accumulation of ROS in the DPP3^{-/-} mice also triggered a higher extent of lipid peroxidation, which was evident from marked increase in the amount of malondialdehyde (MDA), a product of lipid peroxidation, formed in the kidneys of knockout animals (Figure 5B). To investigate the potential role of catalase in protecting the DPP3^{-/-} mice from ROS damage, the level of catalase activity were determined in the kidneys of knockout and WT mice. As expected, the catalase activity increased significantly in the DPP3^{-/-} mice, indicating that the homogenates from the knockout mice consumed notably more H₂O₂ than the WT mice (Figure 5C).

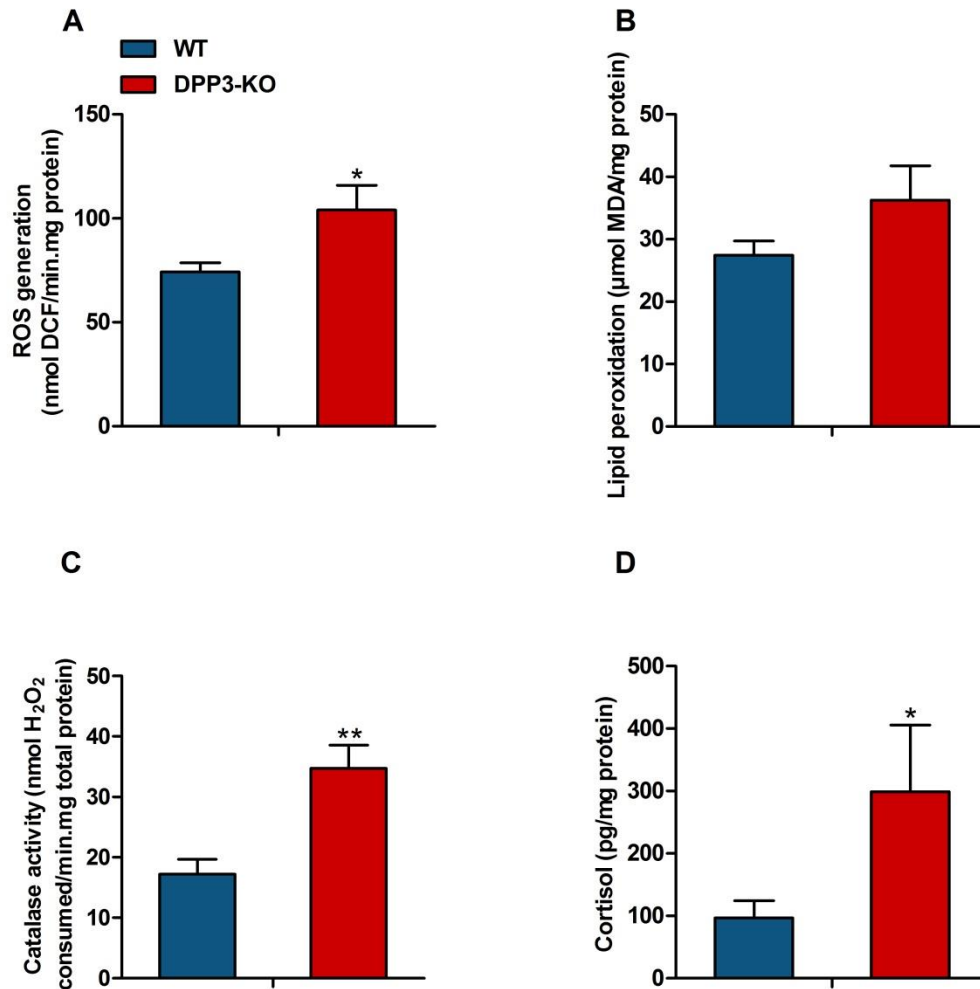


Figure 5 Susceptibility of DPP3 knockout mice to oxidative stress. Quantification of ROS production (A), Lipid peroxidation (B), catalase activity (C) and cortisol level (D) in $DPP3^{-/-}$ (DPP3-KO) and $DPP3^{+/+}$ (WT) male mice ($n = 5/\text{group}$). * $p < 0.05$, ** $p < 0.01$, *** $p < 0.001$ versus wildtype mice based on unpaired two-sided Student's *t*-test. Data represents mean \pm SEM.

To further substantiate the involvement of DPP3 in metabolic dysfunction, we assessed the cortisol levels in kidney tissue homogenates. Kidneys are the primary sites for most active cortisol metabolism and it is suggested that cortisol might influence the renal functions directly by regulating the renal blood flow and glomerular filtration rate. Excessive cortisol is also implicated in the genesis of essential hypertension. Quantification of cortisol using ELISA showed an acute increase of the steroid hormone in the kidneys of $DPP3^{-/-}$ mice, insinuating its improper clearance by the peripheral enzymes (Figure 5D). These results buttress our working hypothesis that loss of DPP3 has a central and pronounced role in oxidative damage in mice.

Discussion

In this study, we have demonstrated that genetic deletion of DPP3 in mice causes altered metabolic behaviour. The DPP3^{-/-} mice have significantly higher food intake than their wild-type littermates. The reduction in DPP3 activity is also associated with a decreased accumulation of body fat. The decreased body fat in DPP3^{-/-} mice is independent of food intake and apparently due to a high energy expenditure related to shift in metabolic preference towards glucose (30). Furthermore, lack of DPP3 also results in increased water consumption in mice. This large increase in water intake is characteristic in mouse models lacking genes associated with the RAS like angiotensin converting enzyme (ACE) or angiotensinogen, as they have diminished ability to concentrate urine due to impaired renal development (31, 32).

The DPP3^{-/-} mice displayed an increased level of circulating angiotensin peptides including Ang II. Although several other angiotensins were also found to be reduced in the DPP3^{-/-} mice, not so much is known about the function of these peptides. Ang II is an integral part of the RAS and mediates various physiological responses. However, acute increase in the Ang II levels leads to vasoconstriction and thereby, severe hypertension (6, 8, 33). Ang II also increases reactive oxygen species and oxidative stress and depresses mitochondrial energy metabolism (4, 5, 7, 8, 34). There are several reports suggesting that high circulating Ang II concentration is a stimulus for thirst in a variety of species which is consistent with our findings with the DPP3^{-/-} mice (3, 12, 35).

NMR-based urinary metabolite analysis demonstrated that the DPP3^{-/-} mice had significantly lower urinary excretion of indoxyl sulfate, which is involved in aromatic amino acid catabolism, and citric acid (TCA) cycle metabolites, namely, citrate, 2-oxoglutarate and succinate. Evidence from mouse model studies suggest that both acute and chronic Ang II infusion causes decreased expression of mitochondrial metabolic genes, particularly those for the TCA cycle and electron transport chain (36). Downregulation of TCA cycle intermediates is also reported to be characteristic of mitochondrial dysfunction in both non-diabetic (37) as well as type-2 diabetic (14) chronic kidney disease (CKD) patients. The disruption of the TCA cycle in DPP3^{-/-} mice is accompanied by a decline in the production of ATP and NAD⁺. At the same time, there is an accumulation of the NAD⁺ precursors like nicotinamide and nicotinamide-riboside. These results are indicative of suppression of cellular metabolism in the knockout mice (24).

Since both Ang II (5, 7, 33, 34, 38, 39) and indoxyl sulfate (40, 41) mediate ROS production which can contribute to oxidative stress, we measured putative stress markers in the mice. Consistent with our findings, the level of ROS generation, lipid peroxidation, catalase activity and cortisol production were elevated in the knockouts. These results confirm our hypothesis that increased Ang II creates oxidative stress in the DPP3^{-/-} mice. Several proteins involved in defense against oxidative stress like sirtuins and PARP1, use NAD⁺ in the form of substrate or cofactor, thereby consuming the cellular pool of NAD⁺. In the cell, NAD⁺ play pivotal roles in the TCA and mitochondrial electron transport chain, serving as a cofactor for some of the rate-limiting enzymes in the TCA cycle (24, 26, 29, 42, 43). Depletion of NAD⁺ therefore correlates with an energy deficit in the cell which is evident from the decreased TCA cycle intermediates as well as low ATP levels in the DPP3^{-/-} mice. In order to compensate for the decreased cell metabolism and prevent cell death, the knockout mice activate salvage pathways as a survival mechanism against ROS-induced damage.

Thus our work has shown that DPP3 has an influence on the overall RAS pathway in accordance with previous reports (9, 11, 13). The metabolic characterization of DPP3 opens up avenues of research involving the RAS system and its therapeutical exploitation. Although further studies are required to define the plausible role of DPP3 role in the development of renal stress, our work provides the basis to understand the involvement of DPP3 in the renal-cardiovascular circuit.

Materials and Methods

Ethics Statement

All animal experiments were formally approved by the *Ethics Committee of the University of Graz* and the *Austrian Federal Ministry of Science and Research*.

Animals and generation of DPP3 knockout mice

All studies were conducted in age-matched DPP3^{-/-} and WT control male mice on C56BL/6J background. Mice were bred and maintained at regular housing temperatures (23 °C) and 14-h light/10-h dark cycle. Animals had ad libitum access to water and chow diet (4.5% fat, 34% starch, 5.0% sugar, and 22.0% protein; Ssniff Spezialdiäten). Breeding and genotyping were done according to standard procedures. For generation of DPP3 KO mice, targeted mutant ES cells were obtained from EUCOMM and injected into blastocytes of C57BL/6 mice. Chimeric animals with a high degree of coat color chimerism were bred with C57BL/6 mice. The construct containing a β -galactosidase cassette (lacZ) and a promoter-driven selection cassette (neo) was inserted into the *dpp3* gene. Additionally, the construct contained two flippase recognition target (FRT) sites for flippase recombination enzyme (FLP)-mediated recombination flanking lacZ and neo. The selection cassette and exon 6 (essential for DPP3 function), flanked by loxP sites, were removed by breeding with transgenic C57BL/6 mice expressing cre-recombinase (CMV-Cre). Cre-lox recombination resulted in deletion of neo and exon 6 leaving the lacZ reporter gene intact. Mice totally lacking *dpp3* were bred by crossing mice heterozygous for the mutant *dpp3* allele lacking neo and exon 6.

Serum and tissue lysate preparation

Animals were anesthetized with isoflurane using the bell jar method and blood was collected from the retro-orbital plexus. Immediately following collection, blood was placed on ice and allowed to clot, and serum was isolated by centrifugation. For tissue collection, mice were killed by cervical dislocation and tissues were surgically removed and washed with PBS. Homogenization was performed on ice in solution A (0.25M sucrose, 1 mM EDTA, 20 μ M dithiothreitol, 0.1% Triton X-100, 20 μ g/mL leupeptin, 2 μ g/mL antipain, 1 μ g/mL pepstatin, pH 7.0) using an Ultra Turrax (IKA, Staufen, Germany). 20 000 \times g infranatants were used for further experiments. Protein concentrations in the tissue lysates were estimated using the Protein Assay Dye Reagent (Bio-Rad, Munich, Germany) using bovine serum albumin as the standard. Serum and tissue samples were stored at -80°C until further analysis.

DPP3 activity assay in mice tissue lysates

The DPP3 activity in mice tissue lysates were determined by fluorometrically measuring (excitation, 332 nm; emission, 420 nm) the liberation of 2-naphthylamine at 37°C in a mixture containing 25 µl of 200µM Arg-Arg-2-naphthylamide as substrate in 1X TBS buffer (50 mM Tris, 100 mM NaCl, pH 8.2) and tissue lysate equivalent to 20 µg of total protein in a reaction mixture of 235 µl (White, Tissue Culture treated Krystal 2000 96-well plate from Porvair sciences, Norfolk, UK). The activity assay was performed by continuous measurement of fluorescence of 2-naphthylamine for 30 min (Fluorescent plate reader from Molecular Devices, Sunnyvale CA, USA). The reaction was started by the addition of the substrate. The samples were measured in triplicate.

SDS PAGE and western blotting

Tissue lysates were diluted in Laemmli's sample buffer, and 20 µg of total protein/lane was subjected to sodium dodecyl sulfate-polyacrylamide gel electrophoresis (SDS-PAGE) using 10% SDS-polyacrylamide gels. The resolved proteins were transferred onto polyvinylidene difluoride (PVDF) membranes (VWR, Pennsylvania, USA) using a Trans-Blot SD transfer cell (Bio-Rad, CA, USA). Following transfer, membranes were washed with Tris-buffered saline containing 0.01% Tween-20 (TBST) and then blocked in 5% non-fat milk for 1 h at room temperature. The membranes were then incubated overnight with anti-DPP3 rabbit polyclonal antibody (1:1500, Proteintech Europe, Manchester, UK) in TBST containing 5% non-fat milk at 4°C. After washing three times for 10 min in TBST, membranes were incubated with peroxidase-labeled secondary antibody (1:5000; Cell Signaling Technology®, Danvers, MA, USA) for 1 h at room temperature. The immunoblots were developed using enhanced chemiluminescent western blotting substrate solution (Pierce-Thermo Fisher Scientific, Waltham, MA, USA).

Body composition and Indirect calorimetry measurements

Lean and fat mass of mice were analyzed by NMR (the minispec, NMR Analyzer, Bruker, Ettlingen, Germany). Indirect calorimetry (spontaneous physical activity, O₂ consumption, CO₂ production, and food intake) were monitored in metabolic cages allowing continuous measurement of these parameters (LabMaster, TSE Systems GmbH, Bad Homburg, Germany). For measurements of energy balance, animals were familiarized with these cages for at least 72 hours before data collection.

Analysis of angiotensin peptides in serum

Serum conditioning was performed at 37°C followed by stabilization by addition of an enzyme inhibitor cocktail (Attoquant Diagnostics) (PMID 25757657). Stable isotope-labeled internal standards for each Ang metabolite [Ang I, Ang II, Ang-(1-7), Ang-(1-5), Ang-(2-8), Ang-(3-8), Ang-(1-9), Ang-(3-7), Ang-(2-7), Ang-(2-10)] were added to stabilized serum samples at a concentration of 200 pg/mL, while the concentration of the internal standard of Aldosterone (deuterated Aldosterone D4) was spiked at a concentration of 500 pg/mL. Following C18-based solid-phase-extraction and fractionated elution of aldosterone and angiotensins, samples were subjected to LC-MS/MS analysis using a reversed-phase analytical column (Acquity UPLC® C18, Waters, USA) operating in line with a XEVO TQ-S triple quadrupole mass spectrometer (Waters Xevo TQ/S, Milford, Massachusetts, USA) in multiple reaction monitoring modes. The internal standard was used to correct for analyte recovery across the sample preparation procedure in each sample. Analyte concentrations were calculated from integrated chromatograms considering the corresponding response factors determined in appropriate calibration curves in serum matrix, on condition that integrated signals exceeded a signal-to-noise ratio of 10.

Analysis of metabolites by NMR spectroscopy

Phosphate-buffered solution was prepared by dissolving 5.56 g anhydrous NaH₂PO₄, 0.4 g 3(trimethylsilyl)propionic acid-2,2,3,3-d₄ sodium salt (TSP), and 0.2 g NaN₃ in 400 ml deionized water and was adjusted to pH 7.4 with 1 M NaOH and HCl. Upon addition of deionized water to a final volume of 500 ml, the pH was readjusted to pH 7.4 with 1 M NaOH and HCl. For the serum samples, mixture of 200 µl serum and 400 µl methanol were incubated at -20°C for 30 min and centrifuged at 18,000 x g for 30 min to pellet proteins. Supernatants were dried and re-dissolved in 500 µl phosphate buffer and transferred to 5 mm NMR tubes. For the urine samples, mixture of 200 µl urine and 300 µl phosphate buffer were transferred to 5 mm NMR tubes. For the kidney samples, the dried metabolites were dissolved in 500 µl phosphate buffer and transferred to 5 mm NMR tubes. NMR experiments were performed at 310 K on a Bruker Avance III 500MHz spectrometer equipped with a TXI probe head. The one-dimensional (1D) CPMG (Carr–Purcell–Meiboom–Gill) pulse sequence (cpmgrp1d, 73728 points in F1, 12019.230 Hz spectral width, 2048 transients, recycle delay 4 s), with water suppression 8 using presaturation, was used for ¹H 1D NMR experiments. Metabolite reference chemical shifts were taken from the Madison-Qingdao Metabolomics

Consortium Database (<http://mmcd.nmrfa.wisc.edu/>) [5] and all metabolites were cross-checked using reference compounds. Bruker Topspin version 3.1 (Rheinstetten, Germany) and MestReNova version 10.0 (<http://mestrelab.com>) software packages were used for NMR data acquisition, processing, and analyses. Metabolite concentrations were determined using TSP as internal standard.

Measurement of biomarkers for oxidative stress in kidney tissue

(i) Reactive Oxygen Species (ROS) generation

The intracellular ROS level was detected by using 2',7'-dichlorodihydrofluorescein diacetate (H₂DCFDA) (Sigma Aldrich). H₂DCFDA is a cell-permeable indicator for ROS that is nonfluorescent until the acetate groups are removed by intracellular esterases and oxidation occurs within the cell. When oxidized by various active oxygen species, it is irreversibly converted to the fluorescent form, DCF (44, 45). ROS in kidney tissue was estimated by diluting tissue lysate equivalent to 100 µg of total protein in ice-cold 40 mM Tris-HCl buffer (pH 7.4). The samples were divided into two equal fractions. In one fraction 40 µl of 10 µM H₂DCFDA in methanol was added for ROS estimation. Another fraction with 40 µl of methanol was used as a control for tissue auto-fluorescence. All samples were incubated at 37 °C for 15 min and fluorescence was determined at 485 nm excitation and 525 nm emission using a fluorescence plate reader (Molecular Devices, Sunnyvale CA, USA). To quantitate ROS levels, relative dichlorofluorescein fluorescence was used as a standard.

(ii) Detection of Lipid Peroxidation Activity

Lipid peroxidation is a well-established mechanism of cellular damage and is used as an indicator of oxidative stress. The extent of lipid peroxidation in kidney was assessed using Thiobarbituric acid reactive substances (TBARS) as an index. Malondialdehyde (MDA), a product of lipid peroxidation, reacts with two molecules of thiobarbituric acid (TBA) at high temperature and low pH to form a pink-colored complex which can be measured spectrophotometrically (46, 47). For the assay, kidney tissue equivalent to 1 mg of total protein was incubated with 20% TCA and 0.67% TBA. The reaction mixture was heated at 100°C for 30 min and then cooled in an ice-bath for 10 min. The samples were then centrifuged at 3000 rpm for 15 min. The supernatant was collected to measure absorbance at 532 nm. The formation of TBARS was expressed using MDA equivalent as a standard.

(iii) Catalase activity

Catalase is a strong antioxidant enzyme and plays a major role in scavenging ROS (48). Catalase activity was measured by following its ability to split H₂O₂. Briefly, kidney tissue equivalent to 1 mg of total protein in 0.01 M PBS was incubated with 0.2 M H₂O₂. The reaction was stopped by adding 5% dichromate solution at 30 sec intervals. The samples were heated at 60°C for 10 min where the blue precipitate formed was decomposed to a green solution. Consumption of H₂O₂ was determined by recording absorbance at 570 nm. A standard curve containing 0 to 100 μmol of H₂O₂ was prepared to determine the amount of H₂O₂ present in each sample.

(iv) Cortisol assay

Cortisol is the cardinal glucocorticoid hormone, contributing to homeostatic maintenance of basal metabolism and salt and water balance, and modulating the response to stress (49, 50). Intracellular cortisol concentration in kidney tissues was measured using an ELISA kit according to the manufacturer's instructions (Phoenix Pharmaceuticals).

Statistical analysis

All data are expressed as mean ± SEM. Results were assessed using two-tailed unpaired Student's *t* test (GraphPad Prism 5, San Diego, USA). A *P* value less than 0.05 was considered significant.

Acknowledgements

This work was supported by a grant from the Austrian Science Foundation (FWF) through grants W901 (Doctoral Program “Molecular Enzymology”) to KG, PM, RB and RZ. The authors are also grateful for the support by the interuniversity program in natural sciences (NAWI Graz). We thank Emilia Strandback, Karin Koch, Chaitanya R. Tabib and Jakov Ivkovic for experimental advice and discussions. This work was supported by the Bavarian Ministry of Sciences, Research and the Arts (Bavarian Molecular Biosystems Research Network, to T.M.), the President’s International Fellowship Initiative of CAS (No.2015VBB045, to T.M.), the National Natural Science Foundation of China (No. 31450110423, to T.M.), the Austrian Science Fund (FWF: P28854 and I3792 to T.M.), the Austrian Research Promotion Agency (FFG: 864690), the Integrative Metabolism Research Center Graz, the Austrian infrastructure program 2016/2017, BioTechMed/Graz, the OMICS center Graz as well as the Deutsche Forschungsgemeinschaft (DFG) with the grant MA5703/1-1 (to T.M.).

References

1. Brewster UC, Setaro JF, Perazella MA. The renin-angiotensin-aldosterone system: cardiorenal effects and implications for renal and cardiovascular disease states. *Am J Med Sci.* 2003 Jul;326(1):15-24.
2. Perazella MA, Setaro JF. Renin-angiotensin-aldosterone system: fundamental aspects and clinical implications in renal and cardiovascular disorders. *J Nucl Cardiol.* 2003 Mar-Apr;10(2):184-96.
3. Daniels D, Mietlicki EG, Nowak EL, Fluharty SJ. Angiotensin II stimulates water and NaCl intake through separate cell signalling pathways. *Exp Physiol.* 2008 Aug 22;94(1):130-7.
4. Nguyen Dinh Cat A, Montezano AC, Burger D, Touyz RM. Angiotensin II, NADPH oxidase, and redox signaling in the vasculature. *Antioxid Redox Signal.* 2013 Oct 01;19(10):1110-20.
5. Hitomi H, Kiyomoto H, Nishiyama A. Angiotensin II and oxidative stress. *Current Opinion in Cardiology.* 2007 July;22(4):311.
6. Crowley SD, Gurley SB, Herrera MJ, Ruiz P, Griffiths R, Kumar AP, et al. Angiotensin II causes hypertension and cardiac hypertrophy through its receptors in the kidney. *Proc Natl Acad Sci U S A.* 2006 Nov 21;103(47):17985-90.
7. Sachse A, Wolf G. Angiotensin II-induced reactive oxygen species and the kidney. *Journal of the American Society of Nephrology : JASN.* 2007 Sep;18(9):2439-46.
8. de Cavanagh EMV, Inserra F, Ferder M, Ferder L. From Mitochondria to Disease: Role of the Renin-Angiotensin System. *American Journal of Nephrology.* 2007 Oct;27(6):545-53.
9. Prajapati SC, Chauhan SS. Dipeptidyl peptidase III: a multifaceted oligopeptide N-end cutter. *FEBS J.* 2011 Sep;278(18):3256-76.
10. Hast BE, Goldfarb D, Mulvaney KM, Hast MA, Siesser PF, Yan F, et al. Proteomic analysis of ubiquitin ligase KEAP1 reveals associated proteins that inhibit NRF2 ubiquitination. *Cancer Res.* 2013 Apr 01;73(7):2199-210.
11. Pang X, Shimizu A, Kurita S, Zankov DP, Takeuchi K, Yasuda-Yamahara M, et al. Novel Therapeutic Role for Dipeptidyl Peptidase III in the Treatment of Hypertension. *Hypertension.* 2016 09;68(3):630-41.
12. J. T. FITZSIMONS. Angiotensin, Thirst, and Sodium Appetite. *Physiological Reviews.* 1998 Jan 7;78(3):583-686.
13. Cruz-Diaz N, Wilson BA, Chappell MC. Peptidases and the Renin-Angiotensin System: The Alternative Angiotensin-(1-7) Cascade. *Enzyme Inhibitors and Activators.* 2017.

14. Liu J, Liu S, Gurung RL, Ching J, Kovalik J, Tan TY, et al. Urine tricarboxylic acid (TCA) cycle metabolites predict progressive chronic kidney disease in type 2 diabetes. *J Clin Endocrinol Metab*.
15. Dona AC, Kyriakides M, Scott F, Shephard EA, Varshavi D, Veselkov K, et al. A guide to the identification of metabolites in NMR-based metabolomics/metabonomics experiments. *Comput Struct Biotechnol J*. 2016;14:135-53.
16. Stec DF, Wang S, Stothers C, Avance J, Denson D, Harris R, et al. Alterations of urinary metabolite profile in model diabetic nephropathy. *Biochem Biophys Res Commun*. 2015 Jan 09;456(2):610-4.
17. Wojtowicz W, Zabek A, Deja S, Dawiskiba T, Pawelka D, Glod M, et al. Serum and urine ¹H NMR-based metabolomics in the diagnosis of selected thyroid diseases. *Sci Rep*. 2017 Aug 22;7(1):9108.
18. Slupsky CM. NMR-based analysis of metabolites in urine provides rapid diagnosis and etiology of pneumonia. *Biomark Med*. 2010 Apr;4(2):195-7.
19. Watanabe K, Tominari T, Hirata M, Matsumoto C, Hirata J, Murphy G, et al. Indoxyl sulfate, a uremic toxin in chronic kidney disease, suppresses both bone formation and bone resorption. *FEBS Open Bio*. 2017 Aug;7(8):1178-85.
20. Tan X, Cao X, Zou J, Shen B, Zhang X, Liu Z, et al. Indoxyl sulfate, a valuable biomarker in chronic kidney disease and dialysis. *Hemodial Int*. 2017 04;21(2):161-7.
21. Hung S, Kuo K, Wu C, Tarng D. Indoxyl Sulfate: A Novel Cardiovascular Risk Factor in Chronic Kidney Disease. *J Am Heart Assoc*. 2017 Feb 07;6(2).
22. Barreto FC, Barreto DV, Liabeuf S, Meert N, Glorieux G, Temmar M, et al. Serum Indoxyl Sulfate Is Associated with Vascular Disease and Mortality in Chronic Kidney Disease Patients. *Clin J Am Soc Nephrol*. 2009 -10;4(10):1551-8.
23. Pallister T, Jackson MA, Martin TC, Zierer J, Jennings A, Mohny RP, et al. Hippurate as a metabolomic marker of gut microbiome diversity: Modulation by diet and relationship to metabolic syndrome. *Scientific reports*. 2017 Oct 20;7(1):13670-9.
24. Cantó C, Menzies K, Auwerx J. NAD⁺ Metabolism and the Control of Energy Homeostasis: A Balancing Act between Mitochondria and the Nucleus. *Cell Metabolism*. 2015 Jul 7;22(1):31-53.
25. Nady Braidy, Gilles J Guillemin, Hussein Mansour, Tailoi Chan-Ling, Anne Poljak, Ross Grant. Age Related Changes in NAD⁺ Metabolism Oxidative Stress and Sirt1 Activity in Wistar Rats. *PLoS One*. 2011 Apr 1;6(4):e19194.
26. Lina Du, Xiaopeng Zhang, Yong Y. Han, Nancy A. Burke, Patrick M. Kochanek, Simon C. Watkins, et al. Intra-mitochondrial Poly(ADP-ribosylation) Contributes to NAD⁺ Depletion and Cell Death Induced by Oxidative Stress. *Journal of Biological Chemistry*. 2003 May 16;278(20):18426-33.

27. Marie-France Langelier, Levani Zandarashvili, Pedro M Aguiar, Ben E Black, John M Pascal. NAD⁺ analog reveals PARP-1 substrate-blocking mechanism and allosteric communication from catalytic center to DNA-binding domains. *Nature Communications*. 2018 Feb 1,;9(1):1-13.
28. Alano CC, Garnier P, Ying W, Higashi Y, Kauppinen TM, Swanson RA. NAD⁺ depletion is necessary and sufficient for PARP-1 – mediated neuronal death. *J Neurosci*. 2010 Feb 24,;30(8):2967-78.
29. Hassina Massudi, Ross Grant, Gilles J Guillemin, Nady Braidy. NAD⁺ metabolism and oxidative stress: the golden nucleotide on a crown of thorns. 2012 January 1,;17(1):28-46.
30. Jayasooriya AP, Mathai ML, Walker LL, Begg DP, Denton DA, Cameron-Smith D, et al. Mice lacking angiotensin-converting enzyme have increased energy expenditure, with reduced fat mass and improved glucose clearance. *PNAS*. 2008 -05-06 00:00:00;105(18):6531-6.
31. Kihara M, Umemura S, Sumida Y, Yokoyama N, Yabana M, Nyui N, et al. Genetic deficiency of angiotensinogen produces an impaired urine concentrating ability in mice. *Kidney Int*. 1998 Mar;53(3):548-55.
32. Klein JD, Le Quach D, Cole JM, Disher K, Mongiu AK, Wang X, et al. Impaired urine concentration and absence of tissue ACE: involvement of medullary transport proteins. *Am J Physiol Renal Physiol*. 2002 Sep;283(3):517.
33. Benigni A, Cassis P, Remuzzi G. Angiotensin II revisited: new roles in inflammation, immunology and aging. *EMBO Mol Med*. 2010 Jul;2(7):247-57.
34. Su-Mi Kim, Yang-Gyun Kim, Kyung-Hwan Jeong, Sang-Ho Lee, Tae-Won Lee, Chun-Gyoo Ihm, et al. Angiotensin II-Induced Mitochondrial Nox4 Is a Major Endogenous Source of Oxidative Stress in Kidney Tubular Cells. *PLoS One*. 2012 Jul 1,;7(7):e39739.
35. Eric Lazartigues, Puspha Sinnayah, Ginette Augoyard, Claude Gharib, Alan Kim Johnson, Robin L. Davisson. Enhanced water and salt intake in transgenic mice with brain-restricted overexpression of angiotensin (AT1) receptors. *American Journal of Physiology - Regulatory, Integrative and Comparative Physiology*. 2008 Nov 1,;295(5):1539-45.
36. Jennie E. Larkin, Bryan C. Frank, Renee M. Gaspard, Irena Duka, Haralambos Gavras, John Quackenbush. Cardiac transcriptional response to acute and chronic angiotensin II treatments. *Physiological Genomics*. 2004 Jan 1,;18(2):152-66.
37. Hallan S, Afkarian M, Zelnick LR, Kestenbaum B, Sharma S, Saito R, et al. Metabolomics and Gene Expression Analysis Reveal Down-regulation of the Citric Acid (TCA) Cycle in Non-diabetic CKD Patients. *EBioMedicine*. 2017 Dec;26:68-77.
38. Oxidative Stress and Vascular Damage in Hypertension: Role of Angiotensin II [Internet].: Hindawi; 2011 [cited Aug 31, 2018]. Available from: <https://www.hindawi.com/journals/ijhy/2011/916310/>.

39. Wen H, Gwathmey JK, Xie L. Oxidative stress-mediated effects of angiotensin II in the cardiovascular system. *World journal of hypertension*. 2012 Aug 23;2(4):34.
40. Watanabe K, Tominari T, Hirata M, Matsumoto C, Hirata J, Murphy G, et al. Indoxyl sulfate, a uremic toxin in chronic kidney disease, suppresses both bone formation and bone resorption. *FEBS Open Bio*. 2017 08;7(8):1178-85.
41. Dias GF, Bonan NB, Steiner TM, Tozoni SS, Rodrigues S, Nakao LS, et al. Indoxyl Sulfate, a Uremic Toxin, Stimulates Reactive Oxygen Species Production and Erythrocyte Cell Death Supposedly by an Organic Anion Transporter 2 (OAT2) and NADPH Oxidase Activity-Dependent Pathways. *Toxins*. 2018 Jul 5;10(7).
42. Harlan BA, Pehar M, Sharma DR, Beeson G, Beeson CC, Vargas MR. Enhancing NAD⁺ Salvage Pathway Reverts the Toxicity of Primary Astrocytes Expressing Amyotrophic Lateral Sclerosis-linked Mutant Superoxide Dismutase 1 (SOD1). *The Journal of biological chemistry*. 2016 May 13;291(20):10836-46.
43. Weihai Ying. Roles of NAD⁺, PARP-1, and Sirtuins in Cell Death, Ischemic Brain Injury, and Synchrotron Radiation X-Ray-Induced Tissue Injury. *Scientifica*. 2013;2013:691251-11.
44. Pavelescu LA. On reactive oxygen species measurement in living systems. *Journal of medicine and life*. 2015;8 Spec Issue(Spec Issue):38-42.
45. Dikalov S, Griendling KK, Harrison DG. Measurement of Reactive Oxygen Species in Cardiovascular Studies. *Hypertension*. 2007 Apr 1;49(4):717-27.
46. Esterbauer H, Cheeseman KH. Determination of aldehydic lipid peroxidation products: malonaldehyde and 4-hydroxynonenal. *Meth Enzymol*. 1990;186:407-21.
47. Coudray C, Richard MJ, Favier AE. Determination of primary and secondary lipid peroxidation products: Plasma lipid hydroperoxides and thiobarbituric acid reactive substances. In: *Analysis of Free Radicals in Biological Systems*. Birkhäuser Basel; 1995. p. 185-200.
48. Sinha AK. Colorimetric assay of catalase. *Anal Biochem*. 1972 Jun;47(2):389-94.
49. Hannibal KE, Bishop MD. Chronic Stress, Cortisol Dysfunction, and Pain: A Psychoneuroendocrine Rationale for Stress Management in Pain Rehabilitation. *Phys Ther*. 2014 -12;94(12):1816-25.
50. Aschbacher, Kirstin O'Donovan, Aoife Wolkowitz, Owen M. Dhabhar, Firdaus S. Su, Yali Epel, Elissa. Good stress, bad stress and oxidative stress: Insights from anticipatory cortisol reactivity. *Psychoneuroendocrinology*. 2013;38(9):1698-708.

Chapter 3

Efficient inhibition of a metallopeptidase by hydroxyethylene transition state peptidomimetics

**Efficient inhibition of a metallopeptidase by hydroxyethylene transition state
peptidomimetics**

**Jakov Ivkovic,¹ Shaline Jha,² Christian Lembacher-Fadum,¹ Peter Macheroux² and
Rolf Breinbauer,¹**

¹Institute of Organic Chemistry, Graz University of Technology, Graz, Austria

²Institute of Biochemistry, Graz University of Technology, Graz, Austria

Author contributions

P.M. and R.B. initiated the project; P.M., R.B., J.I., S.J., and C.L.F. designed research; J.I., S.J., and C.L.F. performed research; J.I., S.J., and C.L.F. analyzed data and interpreted experimental results; J.I., S.J., P.M. and R.B. wrote the manuscript.

Keywords: Dipeptidyl peptidase 3, Hydroxyethylene isostere, peptidomimetics, *HER*, *SHE*.

Abbreviations:

hDPP3, human Dipeptidyl Peptidase-3; *HER*, (*R*)-hydroxyethylene; *SHE*, (*S*)-hydroxyethylene; Boc, *tert*-Butyl-oxycarbonyl; DIBAL-H, Diisobutylaluminium Hydride; GC-FID, Gas Chromatography-Flame Ionization Detector; TLC, Thin Layer Chromatography; THF, Tetrahydrofuran; HPLC-MS, High Performance Liquid Chromatography – Mass Spectrometry; ESI, Electrospray Ionization; HSQC, Heteronuclear Single Quantum Coherence; HMBC, Heteronuclear Multiple Bond Correlation, COSY, Correlation Spectroscopy; HRMS, High Resolution Mass Spectrometry; LiHDMS, Lithium Hexamethyldisilazide; HBTU, 2-(1*H*-Benzotriazol-1-yl)-1,1,3,3-tetramethyluronium hexafluorophosphate; TFA, Trifluoroacetic Acid; EDTA, Ethylenediaminetetraacetic acid; IPTG, Isopropyl-1-Thio-D-Galactopyranoside; TCEP, Tris(2-CarboxyEthyl)Phosphine; DMSO, Dimethyl sulfoxide; PBS, Phosphate Buffer Saline;

Abstract

The most commonly used drugs as pain medication are opiates, such as morphine or surrogates. However, their long term use can have significant deleterious effects. The mechanism of action of opiates is similar to that of endogenous opioid peptides like enkephalin. They exist within the central and peripheral nervous system and function as neurotransmitters and neuromodulators. Similar to their exogenous counterparts, endogenous opioid peptides afford potent analgesic relief by acting on opioid receptors. The analgesic response elicited by enkephalins is strong but brief due to their rapid inactivation by a class of enzymes called enkephalinases. The main enkephalin-degrading enzymes are neutral endopeptidase, aminopeptidase N and DPP3. To date, DPP3 remains the only known enkephalin-degrading enzyme with no dedicated inhibitor designed for it.

The most effective inhibitor reported for DPP3 is a pentapeptide called tynorphin (VVYPW). However, it rather functions as a slow substrate, getting degraded by the enzyme itself. In the present study we used tynorphin as a template for peptidomimetic design of pseudopeptide inhibitors of DPP3, directed by observations of preferred non-covalent interactions in the crystal structure of the tynorphin-hDPP3 complex. In order to convert tynorphin from a slow substrate to a true inhibitor of DPP3, a noncleavable hydroxyethylene isostere was used to replace the scissile peptide bond. Kinetic and thermodynamic characterization of the resulting inhibitors confirmed their inhibitory properties on hDPP3. In addition, we compared the best inhibitor (HER) to tynorphin as a function of time to demonstrate the superior performance of the novel peptidomimetic.

The insights gained by the characterization of this new class of inhibitors will provide a starting point for the design of molecular tools specific for inhibiting hDPP3 and pave the way to exploit this enzyme as a potential drug target for pain intervention strategies. These inhibitors might offer alternatives to conventional treatments in the nociceptive field, especially the use of new opioid receptor agonists to replace morphine and its derivatives, which possess severe side effects.

Introduction

The lack of inhibitors targeting DPP3 and the need for supporting tools to the efforts in DPP3 enzymology, prompted us to develop small-molecule inhibitors specifically for this enzyme. Since the structure of DPP3 has been determined relatively recently, most the inhibitors tested for DPP3 are the general protease inhibitors. Inhibitors reported till date are not specific for DPP3. These inhibitors can be categorized in several groups- general cysteine, serine and aminopeptidase inhibitors, metal chelators, heavy metals, peptides and microbial broth constituents (1). The substrate inhibitor peptides are being degraded by the enzyme itself and have very short lifetimes in blood serum (2-5). Two fluostatins which are moderate, nonselective inhibitors of DPP3 have been discovered in screening of activity of microbial broths (6), however, their mode of inhibition is still not known. There was one attempt of design of specific inhibitors. However, the design was not structure-guided and the inhibitors inactivate the enzyme via an unknown mechanism (7).

The structure of human DPP3 in complex with the pentapeptide tynorphin has been determined, revealing large conformational changes upon binding, and indicating the very challenging plasticity of its relatively big binding site. We have made the assessment of the binding mode of the peptide ligand in the cocrystal structure, and the crucial interactions that it makes with the binding subsites (2). Major objective of this work was to use tynorphin as a template for peptidomimetic design of pseudopeptide inhibitors of hDPP3, guided by the specific interactions displayed in the cocrystal structure of tynorphin-hDPP3 complex. In order to translate tynorphin from substrate into a true inhibitor of human dipeptidyl peptidase-3, noncleavable peptide bond isosteres are envisioned to replace the corresponding second *N*-terminal peptide bond which is subject to catalytic hydrolysis by the enzyme.

We have proposed the use of hydroxyethylene transition state mimetic isostere as it offers several advantages: it resembles the transient stereoelectronic features of the tetrahedral intermediate which is well recognized and stabilized by the favorable binding action of the enzyme; additionally, use of other transition state mimetics would involve generally much more polar isosteres like sulfonamides, phosphoramidites or phosphinates, and they would cause more undesirable polar peptide-like properties, which need to be gradually removed according to the principles of peptidomimetics (in respect to the desolvation penalty upon binding, and lower bioavailability of peptides and finally, in contrast to chelating zinc-binding functions which are very often used in metallopeptidase inhibitor design, hydroxyethylene

provides only one oxygen atom as a coordinating bond donor, which can be carefully placed in the design, to maximize the cooperative interactions with zinc ion and the neighboring structural features in the binding site (8-10).

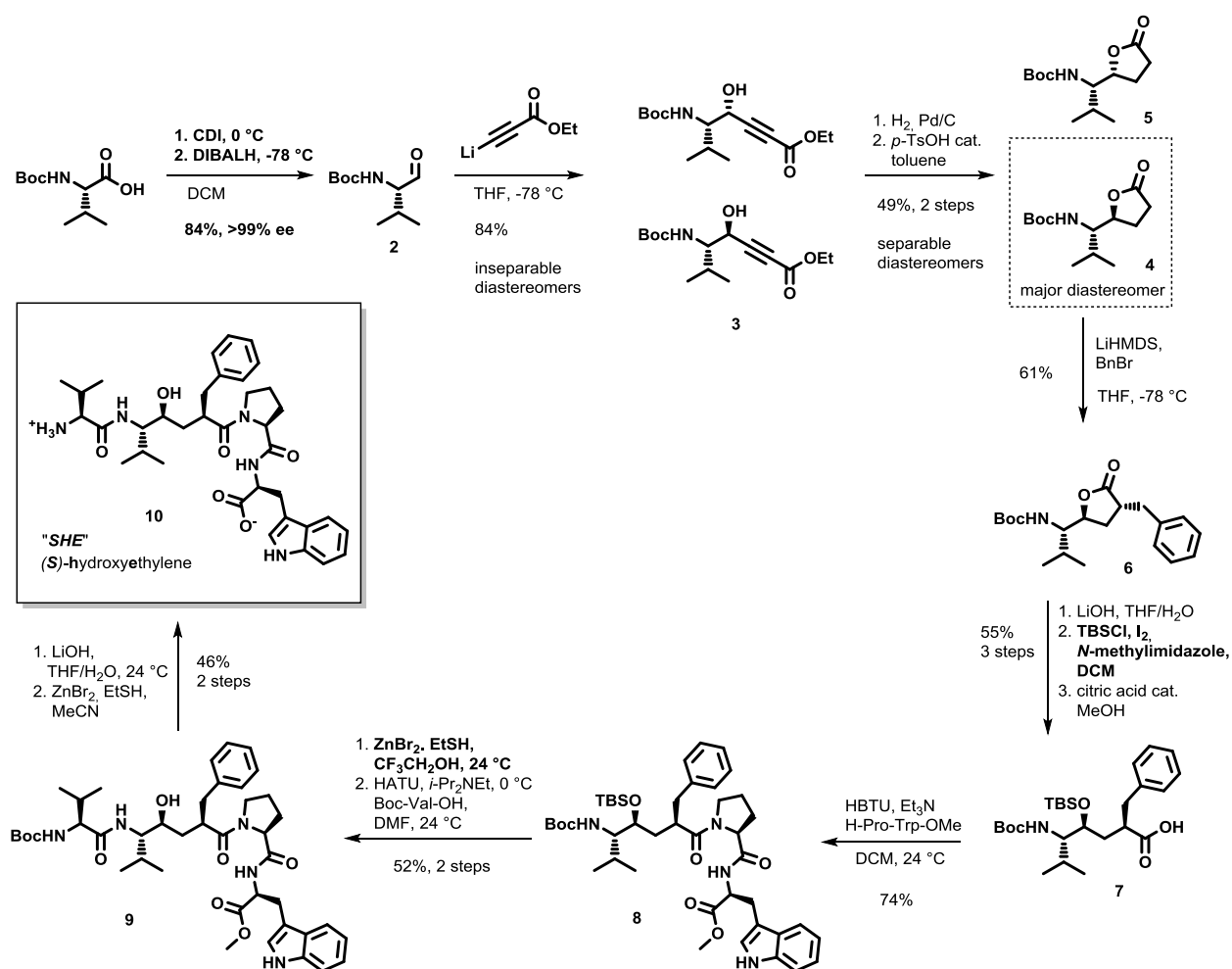
An additional objective was the optimization of inhibitor design in the direction of bioavailable molecules. This should be accomplished by exchanging the peptide structural features for nonpeptidic ones, in accordance with the peptidomimetic principles and the structure-activity relationship information generated throughout the project, together with biologists who will perform *in vivo* studies. The ultimate goal of this work is to find a potent, selective and bioavailable inhibitor of human DPP3, suitable for use as a tool in dose-dependent and time-dependent studies of chemical interference with the role of the enzyme *in vivo*, which will provide a better understanding of the biological role of hDPP3.

Results

Structure-based Design of Inhibitors of hDPP3

(i) Synthesis of (*S*)-Hydroxyethylene Pseudopeptide (*SHE*)

SHE was synthesized in fourteen steps using Boc-protection compatible chemistry (Scheme 1). The chiral pool synthesis started from protected L-valine, from which diastereoselective formation of the two crucial stereogenic centers in the central pseudodipeptide fragment was controlled.



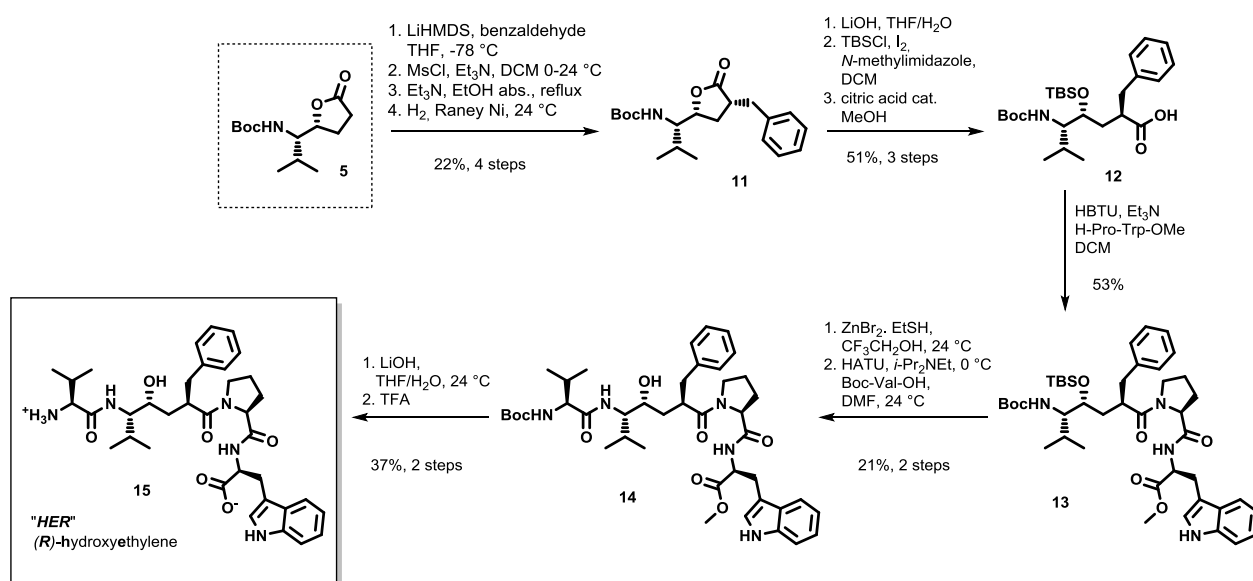
Scheme 1 Summary of the synthesis of *SHE*.

The poor stereoselectivity of addition of the lithiopropiolate to the aldehyde **2** provided also the lactone **5**, which is properly configured for use in the synthesis of the (*R*)-hydroxyethylene epimer. Diastereoselective enolate alkylation afforded lactone **6**, which was opened and

protected to yield the stable pseudodipeptide acid **7**, setting the stage for peptide coupling with the Pro-Trp fragment. Careful development of simultaneous Boc and TBS deprotections shortened the synthesis. Additional peptide coupling with Boc-valine provided the desired scaffold **9**. The target compound **10** was obtained via consecutive C-terminal methyl ester saponification and N-terminal Boc-deprotection.

(ii) Synthesis of (*R*)-Hydroxyethylene Pseudopeptide (*HER*)

SHE was synthesized in a three step shorter sequence, taking into account that we produced *HER* performing a considerably more demanding stereoselective alkylation of the γ -lactone **5** (Scheme 2). Formation of the desired topology of the alkylated lactone **11** required an aldol reaction and subsequent handling of a mixture of four aldol diastereomers through mesylation, elimination and diastereoselective hydrogenation. From that point on, the synthetic pathway through lactone opening, and two peptide couplings afforded the final molecule.



Scheme 2 Summary of the synthesis of *HER*.

Biochemical characterization of *SHE* and *HER*

(i) Hydroxyethylene Transition State Mimetics can inhibit active hDPP3

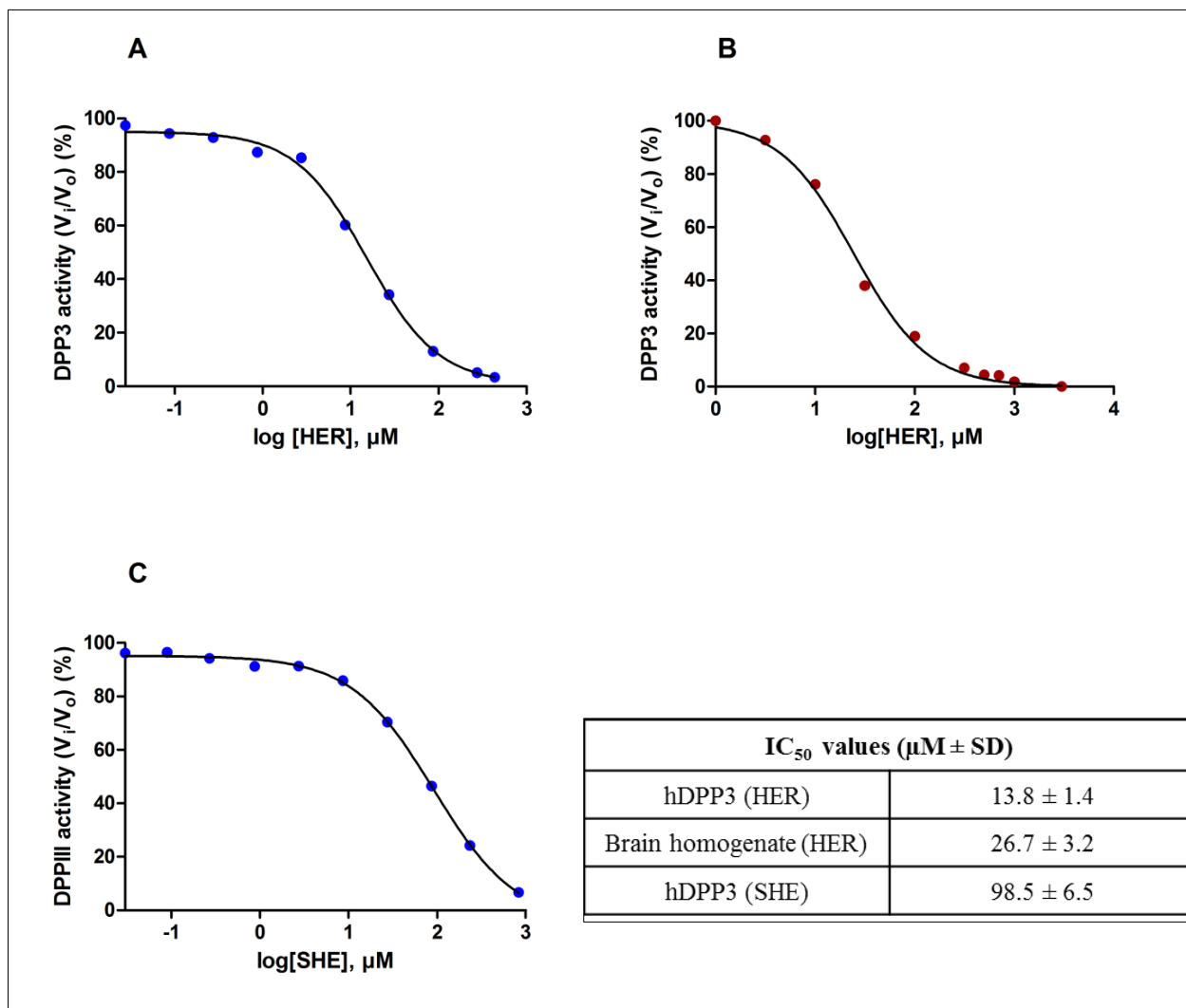


Figure 1 (A) *In vitro* and (B) *ex vivo* dose-response curves demonstrating DPP3 inhibition by *HER*. (C) Dose-response curve demonstrating DPP3 inhibition by *SHE*. Data is represented as mean values obtained from a minimum of three independent experiments with their standard deviations (SD).

Inhibition potencies of both *SHE* and *HER* were investigated via fluorescence-based competitive inhibition assay of degradation of the Arg-Arg-β-naphthylamide substrate. IC₅₀ values were calculated based on the resulting dose response curves. Both transition state mimetics inhibited hDPP3. *SHE* inhibited the enzyme with IC₅₀ = 98.5 µM, and inhibition with *HER* resulted in IC₅₀ = 13.8 µM, making it 7-fold more potent than *SHE*. Importantly,

HER could also efficiently inhibit DPP3 in mouse brain homogenate without losing much of its potency. Difference in potency between **SHE** and **HER** is in line with the expectations proposed based on the structure based design, where structural motifs of both transition state mimetics were compared to the transition state of peptide cleavage. The (*S*)-hydroxyethylene was expected to bind to the zinc ion of the active site, and the (*R*)-hydroxyethylene was expected to strengthen its enthalpic binding term by the additional hydrogen bond to His568.

(ii) Isothermal titration calorimetry Assay confirms binding of compounds to hDPP3

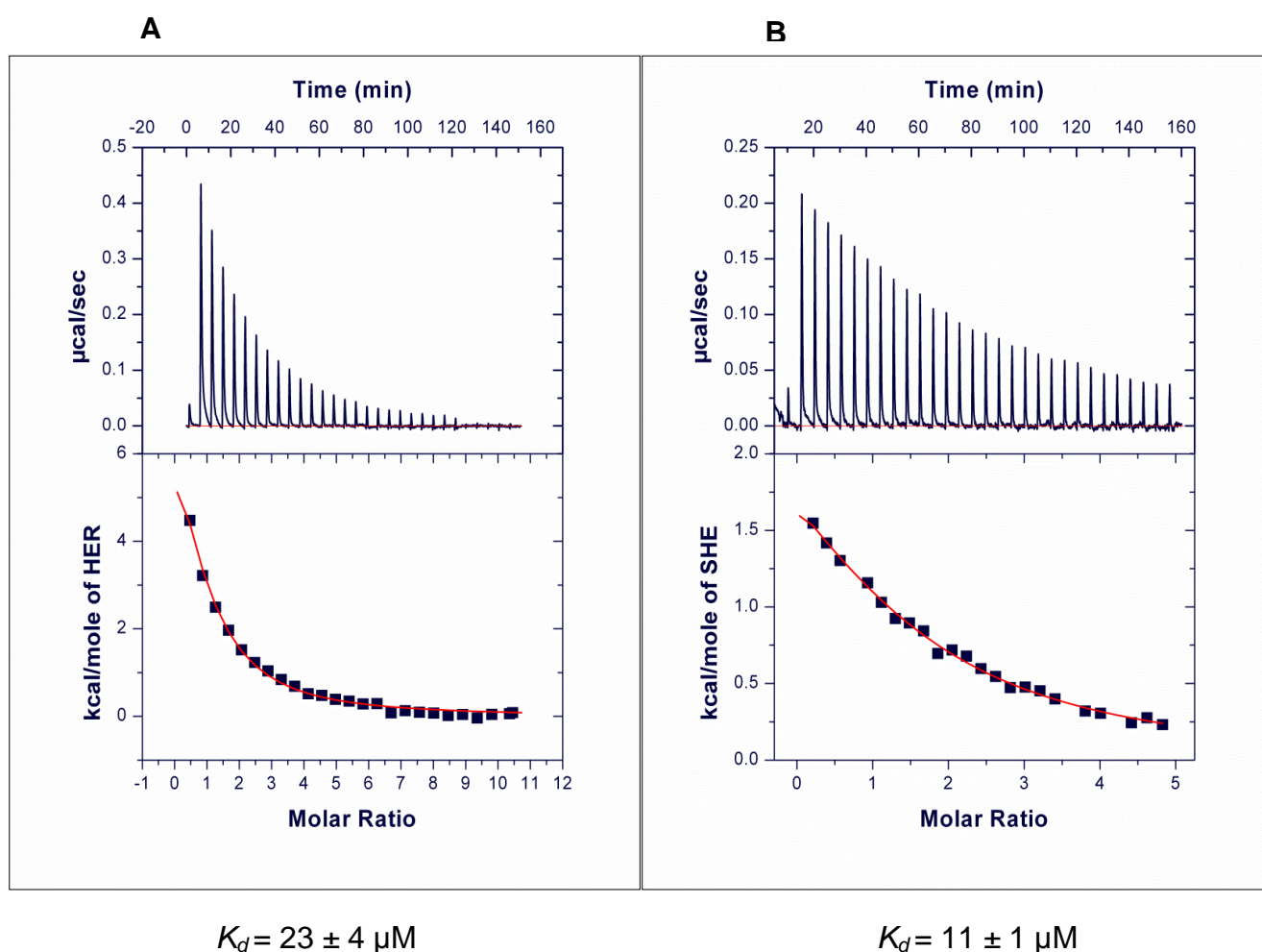


Figure 2 ITC measurement curves of DPP3 with (A) HER and (B) SHE

In ITC (isothermal titration calorimetry) measurements it was found that the ligand-hDPP3 binding process has an endothermic profile. Usually, the thermodynamics of peptide binding

to a protein is dominated by formation of hydrogen bonds between the ligand and complementary ordered H-bond donors/acceptors of the binding site.^[337] Formation of polar interactions is accompanied by favorable enthalpic change. The strongly endothermic profile of ligand binding to hDPP3 indicated that the entropy term dominates the process in this case, which is a rare phenomenon among peptidases. Based on structural observation of a large collapse of two domains upon binding, expelling up to 30 ordered molecules of water, it was rationalized that these water molecules provide an “entropy pool” which greatly outcompetes the positive enthalpic term. In order to investigate whether the hydroxyethylene transition state mimetics binds to hDPP3 and to compare the thermodynamic profile with the tynorphin binding event, hDPP3 was subjected to isothermal microcalorimetric titration with *SHE* and *HER*. We observed that both these compounds bind to hDPP3 displaying equivalent endothermic character (Figure X). While *SHE* could bind to purified hDPP3 enzyme with an affinity of 23 μ M, the binding of *HER* to hDPP3 was stronger with a K_d of 11 μ M. This corroborates the values obtained from the fluorescence-based assays.

(iii) *HER* can stably inhibit hDPP3 in a time-based manner

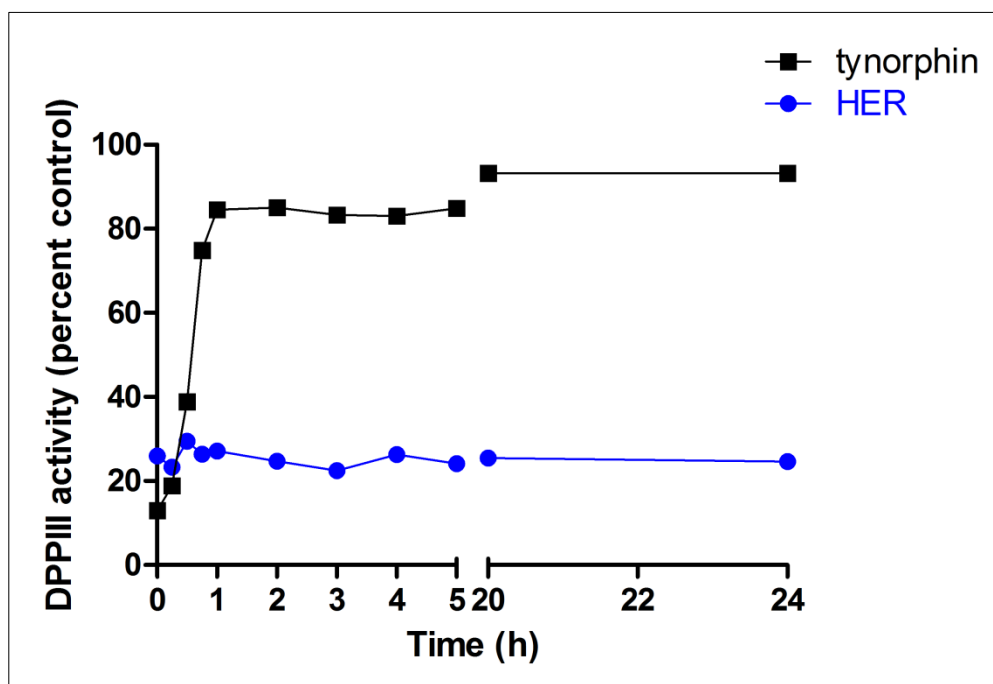
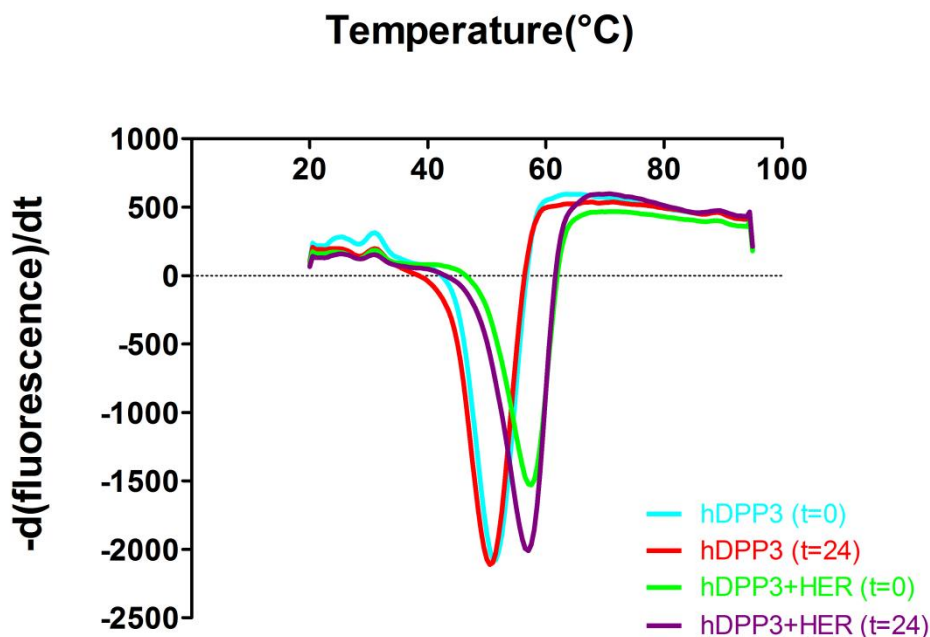


Figure 3 Time-dependent inhibition of DPP3 by tynorphin (black rectangles) and HER (blue circles). The x-axis represents incubation time in hours and the y-axis represents the percentage of DPP3 activity compared to control.



Melting temperature (T_m) (in °C)			
hDPP3 (t=0)	hDPP3+HER (t=0)	hDPP3 (t=24)	hDPP3+HER (t=24)
51.5	57.5	50.5	57

Figure 4 Thermal transitions (upper panel) and melting temperatures of hDPP3 in the presence and absence of **HER** (taken at two time points: 0 and 24 hours of incubation) determined by Thermofluor®

A comparison of time-dependent inhibition of hDPP3 by **HER** and tynorphin revealed that **HER** is not degraded by the peptidase and therefore can efficiently inhibit the activity over a period of 24 h. On contrary, tynorphin being a peptide inhibitor was purportedly cleaved by hDPP3 and thereby lost its efficacy within the first hour. This was also confirmed by the thermal stability assay where stabilization of structure due to binding of **HER**, indicated by an increase in the protein melting temperature was retained even after 24 h.

Discussion

The structural insights into the non-covalent interactions in the tynorphin-hDPP3 complex, presented this pentapeptide as a lead structure for structure-based inhibitor design. The next logical step to create a true inhibitor out of this slow converting substrate inhibitor was to make a modification which will render it immune to the action of hDPP3. We propose to incorporate a hydroxyethylene moiety instead of the cleavable peptide bond, as a noncleavable isostere resembling the transition state in the peptide bond hydrolysis. Hydroxyethylene has a tetrahedral geometry, equivalent to the geometry of the transition state complex. It has a stable chiral configuration, and it can be obtained in two different configurations, both viable for synthesis. We set out to produce both (*S*) and (*R*) epimers of hydroxyethylene transition state mimetics of tynorphin. Using the main tynorphin scaffold is expected to provide selectivity over other enkephalinases, as demonstrated in the research on endogenous peptides which inhibit DPP3 (3).

Here we show that both *SHE* and *HER* inhibit purified hDPP3 in the low micromolar concentration by using fluorescence-based and calorimetric assays, with *HER* being slightly better than *SHE*. Additionally, *HER* also inhibited the activity of DPP3 in the mouse brain homogenate, indicating that it is also effective *ex vivo*. In a time-dependent comparison of *HER* and tynorphin, it was clear that *HER* is much more efficient in inhibiting hDPP3 stably over a period of time. This confirms that the hydroxyethylene-based inhibitors are not degraded by the enzyme itself, as it was observed in the case of tynorphin (3). Although our attempts to get a co-crystal structure of hDPP3 and *HER* were not successful, an increase in thermal stability indicates that binding of *HER* is followed by closing of the upper and lower domain of hDPP3 leading to a more compact structure, as seen in the case of other reported ligands (1, 2).

In one of the greatest milestones in drug design, hydroxyethylene-based HIV-1 protease targeting drugs have been developed, indicating that hydroxyethylene is a privileged molecular feature in protease inhibitor design. Presently, some of the most attractive drug targets among metalloproteases are matrix metalloproteases. All of the drug development efforts on these zinc endopeptidases have failed so far, one of the major reasons being lack of selectivity (11). A new type of metallopeptidase inhibitors would provide fresh starting grounds in contrast to the metal chelating inhibitors, whose chelation ability often proves to be very problematic in terms of selectivity over metalloprotein off-targets.

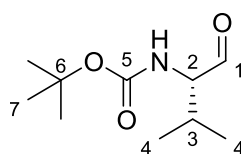
To the best of our knowledge, no hydroxyethylene transition state mimetic inhibitors have been previously reported as inhibitors of a metalloenzyme. Herein, we demonstrate the viability of hydroxyethylene transition state mimetics in the design of metallopeptidase inhibitors, and inspire confidence that the hydroxyethylene type inhibitors could be developed into metallopeptidase targeting drugs (e.g. neprilysin, matrix metalloproteases). The advantage of the hydroxyethylene inhibitors is their fundamental property of resistance to the action of the enzyme, which cannot cleave the C–C bond introduced instead of the peptide bond. The exact role of hDPP3 *in vivo* remains elusive. Investigation on a murine model, including the DPP3 knock-out specimens, is an ongoing effort. Access to smaller and easily synthesized inhibitors would provide an invaluable tool for studying activity of DPP3 in organisms and could provide a foundation to DPP3 targeting drug design.

Materials and Methods

Organic synthesis of SHE and HER

(i) Synthesis of SHE

tert-Butyl *N*-[(2*S*)-3-methyl-1-oxobutan-2-yl]carbamate (**2**) (12)



2

A 1000 mL two-neck round-bottom flask with a Schlenk adapter, a glass stopper and a magnetic stirring bar was heated, dried under vacuum and purged with N₂. Boc-L-Val-OH (10.864 g, 50.0 mmol, 1.0 eq) was added and dissolved in abs. dichloromethane (333 mL). The solution was cooled to 0 °C (ice bath) and 1,1'-carbonyldiimidazole (8.918 g, 55.0 mmol, 1.1 eq) was added. A gas bubbler was mounted instead of the glass stopper to allow pressure relief. After stirring for 60 min the gas bubbler was removed and the colorless reaction solution was cooled to -78 °C (CO₂/acetone bath) for 15 min. A septum was mounted instead of the glass stopper while maintaining a gentle counter flow of N₂. Subsequently, 1.0 M DIBAL-H solution in toluene (105 mL, 105 mmol, 2.1 eq) was added dropwise with a syringe through the septum throughout 110 min. The reaction mixture was stirred at -78 °C until TLC indicated quantitative conversion (45 min). The reaction mixture was quenched by the addition of EtOAc (335 mL). The acetone bath was removed, the gas bubbler was mounted, and 25% aqueous tartaric acid (222 mL) was added to the mixture under vigorous stirring. The mixture was warmed up by immersing the vessel into a water bath at RT and stirred vigorously for 15 min. The stirring was stopped and the layers were separated. The aqueous phase was extracted with EtOAc (333 mL) and the combined organic extracts were washed with 1 M HCl (222 mL), 0.8 M NaHCO₃ (222 mL) and brine (222 mL), dried over Na₂SO₄, filtered and concentrated under reduced pressure. The crude product was frozen in liquid nitrogen and was allowed to reach room temperature under high vacuum. The freeze-thaw procedure was repeated two times. Crude product (8.474 g, 42.10 mmol, 84 %) was furnished as a viscous colorless liquid, and used without further purification.

Yield: 8.474 g (42.10 mmol, 84 %), viscous colorless liquid.

$[\alpha]_D^{23} = +78.6^\circ$ (c = 1.07, CH₂Cl₂), lit. $[\alpha]_D^{20} = +82.1^\circ$ (c = 1, CH₂Cl₂).

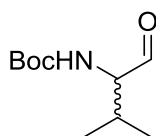
$R_f = 0.61$ (cyclohexane/ethyl acetate = 2:1 (v/v); staining: KMnO₄).

¹H NMR (300 MHz, CDCl₃) $\delta = 9.63$ (s, 1H, H-C1), 5.15-4.99 (m, 1H, NH), 4.33-4.15 (m, 1H, H-C2), 2.37-2.14 (m, 1H, H-C3), 1.44 (s, 9H, H-C7), 1.02 (d, ³J = 6.9 Hz, 3H, H-C4), 0.93 (d, ³J = 7.0 Hz, 3H, H-C4).

¹³C NMR (75 MHz, CDCl₃) $\delta = 200.5$ (s, 1C, C1), 156.0 (s, 1C, C5), 80.1 (s, 1C, C6), 64.8 (s, 1C, C2), 29.2 (s, 1C, C3), 28.4 (s, 3C, C7), 19.2 (s, 1C, C4), 17.7 (s, 1C, C4).

GC-FID (CP-Chirasil Dex): $t_R((S)-) = 9.0$ min, 100%; $t_R((R)-) = 9.2$ min, no abundance detected; ee > 99%.

Racemic *tert*-butyl *N*-[(2*S*)-3-methyl-1-oxobutan-2-yl]carbamate (*rac*-2)



***rac*-2**

A 10 mL Schlenk tube, a glass stopper and a magnetic stirring bar was heated, dried under vacuum and purged with N₂. Boc-DL-Val-OH (43 mg, 0.20 mmol, 1.0 eq) was added and dissolved in abs. dichloromethane (1.3 mL). The solution was cooled to 0 °C (ice bath) and 1,1'-carbonyldiimidazole (36 mg, 0.22 mmol, 1.1 eq) was added. A gas bubbler was mounted instead of the glass stopper to allow pressure relief. After stirring for 60 min the gas bubbler was removed and the colorless reaction solution was cooled to -78 °C (CO₂/acetone bath) for 15 min. A septum was mounted instead of the glass stopper while maintaining a gentle counter flow of N₂. Subsequently, 1.0 M DIBAL-H solution in toluene (0.42 mL, 0.42 mmol, 2.1 eq) was added dropwise with a syringe through the septum throughout 10 min. The reaction mixture was stirred at -78 °C until TLC indicated quantitative conversion (60 min). The reaction mixture was quenched by the addition of EtOAc (1.3 mL). The acetone bath was removed, the gas bubbler was mounted, and 25% aqueous tartaric acid solution (1.0 mL) was added to the mixture under vigorous stirring. The mixture was warmed up by immersing the

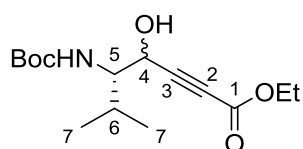
vessel into a water bath at RT and stirred vigorously for 15 min. The stirring was stopped and the layers were separated. The aqueous phase was extracted with EtOAc (1.3 mL) and the combined organic extracts were washed with 1 M HCl (1.0 mL), 0.8 M NaHCO₃ (1.0 mL) and brine (1.0 mL), dried over Na₂SO₄, filtered and concentrated under reduced pressure. The crude product was frozen in liquid nitrogen and was allowed to reach room temperature under high vacuum. The freeze-thaw procedure was repeated two times. The crude product (33 mg, 0.16 mmol, 80 %) was furnished as a colorless liquid.

Yield: 33 mg (0.16 mmol, 80 %), colorless liquid.

R_f = 0.61 (cyclohexane/ethyl acetate = 2:1 (v/v); staining: KMnO₄).

GC-FID (CP-Chiralsil Dex CP): t_R ((*S*-)) = 9.0 min; t_R ((*R*-)) = 9.2 min.

Ethyl (5*S*)-5-[(*tert*-butoxy)carbonylamino]-4-hydroxy-6-methylhept-2-ynoate (3) (13)



3

In an oven dried and nitrogen-purged 500 mL Schlenk vessel equipped with a Teflon[®]-coated magnetic stirring bar, 1-pentyne (7.87 mL, 79.8 mmol, 2.10 eq) was dissolved in 125 mL absolute THF and cooled to 0 °C in an ice bath. To the stirred solution 2.50 M *n*-BuLi in hexanes (30.40 mL, 76.0 mmol, 2.00 eq) was added dropwise via syringe and septum within 3 min. The yellow reaction solution was stirred and cooled for 15 min to -78 °C in an acetone/dry ice bath and subsequently ethyl propiolate (7.70 mL, 76.00 mmol, 2.00 eq) was added dropwise via syringe and septum. The orange reaction solution was stirred at -78 °C for 15 min and then a freshly prepared solution of aldehyde (7.648 g, 38.00 mmol, 1.00 eq) in absolute THF (65 mL) was added dropwise within 10 min via a cannula by applying a gentle nitrogen overpressure from the donor vessel. The reaction was stirred at -78 °C until TLC indicated full conversion of the aldehyde (60 min). The orange reaction mixture was quenched by the dropwise addition of a solution of AcOH (10 mL) in THF (20 mL) and was brought to RT by immersion in a water bath and stirring for 15 min. The mixture was diluted with EtOAc (380 mL) and washed with 5% NaHCO₃ (2x100 mL) and brine (50 mL). The organic extract was concentrated under reduced pressure. Flash chromatography (SiO₂,

cyclohexane/EtOAc 7:1) afforded a viscous orange liquid (9.515 g, 31.78 mmol, 84%) as a mixture of two diastereomers.

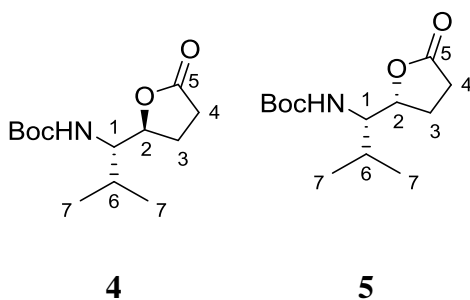
Yield: 9.515 g (31.78 mmol, 84%), viscous orange liquid.

R_f = 0.30 (cyclohexane/EtOAc 3:1 (v/v); staining: KMnO_4).

^1H NMR (300 MHz, CDCl_3 , mixture of 2 diastereomers, based on COSY and HSQC) δ = 4.91 and 4.69 (d, 3J = 8.6 Hz, 1H, HNCO), 4.58 (br s and d, 3J = 4.8 Hz, 1H, H-C4), 4.28–4.14 (m, 2H, CH_2CH_3), 3.69–3.56 and 3.51–3.36 (m, 1H, H-C5), 2.20–2.01 and 1.88–1.73 (m, 1H, H-C6), 1.46 and 1.44 (s, 9H, $(\text{CH}_3)_3$), 1.34–1.25 (m, 3H, CH_2CH_3), 1.03–0.89 (m, 6H, H-C7).

^{13}C NMR (75 MHz, CDCl_3 , mixture of 2 diastereomers, based on COSY and HSQC) δ = 157.6 and 157.1 (s, 1C, HNCO), 153.4 and 153.3 (s, 1C, C1), 86.2 and 84.8 (s, 1C, C3), 80.7 and 80.2 (s, 1C, $(\text{CH}_3)_3\text{C}$), 78.0 (s, 1C, C2), 64.9 and 64.0 (s, 1C, C4), 62.4 and 62.2 (s, 1C, CH_2CH_3), 61.4 and 60.8 (s, 1C, C5), 30.3 and 28.8 (s, 1C, C6), 28.4 (s, 3C, $(\text{CH}_3)_3$), 20.1 and 20.0 (s, 1C, C7), 19.2 and 18.5 (s, 1C, C7), 14.1 (CH_2CH_3).

***tert*-Butyl *N*-[(1*S*)-2-methyl-1-[(2*S*)-5-oxooxolan-2-yl]propyl]carbamate (4) and *tert*-butyl *N*-[(1*S*)-2-methyl-1-[(2*R*)-5-oxooxolan-2-yl]propyl]carbamate (5) (13)**



Hydrogenation: In a 250 mL round-bottom two-neck flask equipped with a Schlenk adapter, glass stopper and a Teflon[®]-coated magnetic stirring bar, **3** (9.400 g, 31.40 mmol, 1.00 eq) was dissolved in EtOAc (126 mL) and stirred at RT. The solution was degassed three times by alternate evacuation and filling with N_2 gas. 5% Pd/C (668 mg, 0.310 mmol, 0.01 eq) was added to the solution and a hydrogen balloon was mounted. The solution was purged three times by alternate evacuation and filling with H_2 gas. The black mixture was vigorously stirred in the H_2 -atmosphere until complete consumption of starting material was indicated by

TLC (20 h). The reaction flask was disconnected from the hydrogen balloon and purged with N₂. Under nitrogen atmosphere the content of the flask was transferred to the nitrogen-purged fritted Schlenk type funnel containing a 1.5 cm thick compressed bed of Celite. The product was eluted from the filter cake with EtOAc (3×13 mL). The Celite bed with the solid catalyst was washed with THF (5 mL) and water (5 mL), and stored under water in a container dedicated for catalyst waste. The product containing filtrate was concentrated under reduced pressure to furnish a yellow liquid residue.

Lactonization: In a 250 mL round-bottom flask equipped with a Teflon[®]-coated magnetic stirring bar, the yellow liquid residue was dissolved in toluene (126 mL) and *p*-TsOH×H₂O (60 mg, 0.31 mmol, 0.01 eq) was added. The pale yellow solution was stirred and heated at 50 °C (oil bath) for 2 h. The reaction solution was cooled to RT, washed with 5% NaHCO₃ (2×100 mL) and brine (100 mL), dried over Na₂SO₄ and concentrated under reduced pressure. Flash chromatography (SiO₂, cyclohexane/EtOAc 6:1 to 4:1) afforded two separated diastereomers: **4** (2.661 g, 10.34 mmol, 33%) as a viscous pale yellow liquid, and **5** (1.262 g, 4.904 mmol, 16%) as a pale yellow solid.

Characterization of tert-butyl N-[(1S)-2-methyl-1-[(2S)-5-oxooxolan-2-yl]propyl]carbamate (4):

Yield: 2.661 g (10.34 mmol, 33%, 2 steps), viscous pale yellow liquid.

$[\alpha]_D^{23} = -51.7^\circ$ (c = 0.56, CHCl₃).

R_f = 0.31 (cyclohexane/EtOAc 2:1 (v/v); staining: KMnO₄).

¹H NMR (300 MHz, CDCl₃, based on HSQC) δ = 4.76–4.64 (m, 1H, H–C2), 4.57 (d, ³J = 10.1 Hz, 1H, NH), 3.43 (m, 1H, H–C1), 2.50 (dd, ³J = 9.4 Hz, 7.4 Hz, 2H, H–C4), 2.28–1.98 (m, 2H, H–C3), 1.90–1.73 (m, 1H, H–C6), 1.42 (s, 9H, (CH₃)₃), 1.06–0.89 (m, 6H, H–C7).

¹³C NMR (75 MHz, CDCl₃, based on HSQC) δ = 177.5 (s, 1C, C5), 156.5 (s, 1C, HNCO), 80.0 (s, 1C, C2), 79.8 (s, 1C, Me₃C), 58.5 (s, 1C, C1), 31.5 (s, 1C, C6), 28.7 (s, 1C, C4), 28.4 (s, 3C, (CH₃)₃), 24.9 (s, 1C, C3), 19.8 (s, 1C, C7), 19.4 (s, 1C, C7).

Characterization of tert-butyl N-[(1S)-2-methyl-1-[(2R)-5-oxooxolan-2-yl]propyl]carbamate (5):

Yield: 1.262 g (4.904 mmol, 16%, 2 steps), pale yellow solid.

$[\alpha]_D^{23} = -7.6^\circ$ ($c = 1.00$, CHCl_3).

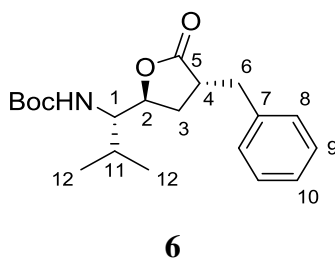
m.p. = 100–105 °C.

$R_f = 0.24$ (cyclohexane/EtOAc 2:1 (v/v); staining: KMnO_4).

^1H NMR (300 MHz, CDCl_3 , based on HSQC) $\delta = 4.43$ (d, $^3J = 9.5$ Hz, 1H, NH), 4.38–4.25 (m, 1H, H–C2), 3.74–3.51 (m, 1H, H–C1), 2.66–2.38 (m, 2H, H–C4), 2.36–1.94 (m, 3H, H–C3 and H–C6), 1.42 (s, 9H, $(\text{CH}_3)_3$), 1.06–0.75 (m, 6H, H–C7).

^{13}C NMR (75 MHz, CDCl_3 , based on HSQC) $\delta = 177.0$ (s, 1C, C5), 156.2 (s, 1C, HNCO), 79.9 (s, 1C, Me_3C), 79.8 (s, 1C, C2), 57.8 (s, 1C, C1), 28.4 (s, 3C, $(\text{CH}_3)_3$), 28.3–27.9 (m, 2C, C4 and C6), 25.2 (s, 1C, C3), 19.9 (s, 1C, C7), 15.7 (s, 1C, C7).

***tert*-Butyl *N*-[(1*S*)-1-[(2*S*,4*R*)-4-benzyl-5-oxooxolan-2-yl]-2-methylpropyl]carbamate (6)**
(13)



In an oven dried, argon purged 250 mL two-neck round-bottom flask, equipped with a dropping funnel, a gas valve adapter and a Teflon[®]-coated magnetic stirring bar, **4** (1.590 g, 6.228 mmol, 1.00 eq) was dissolved in THF (32.8 mL), stirred and cooled to -78 °C in an acetone/dry ice bath. 1.0 M LiHMDS solution in hexanes (12.8 mL, 12.8 mmol, 2.05 eq) was added dropwise within 5 min and the resulting solution was stirred for 30 min. A solution of benzyl bromide (741 μL , 6.23 mmol, 1.00 eq) in THF (32.8 mL) was charged into the dropping funnel, added dropwise to the reaction mixture within 10 min and the resulting orange reaction solution was stirred at -78 °C, until TLC indicated full conversion (55 min). The reaction mixture was poured into a vigorously stirred 3 M NH_4Cl aqueous solution (65.6 mL). The layers were separated and the aqueous layer was extracted with EtOAc (2 \times 66 mL). The combined organic extracts were washed with 0.1 M HCl (33 mL), NaHCO_3 (33 mL), brine (11 mL), dried over Na_2SO_4 , and concentrated and dried under reduced pressure. Flash

chromatography (SiO₂, cyclohexane/EtOAc 8:1 to 5:1) furnished **6** (1.330 g, 3.828 mmol, 61%) as a colorless viscous liquid.

Yield: 1.330 g (3.828 mmol, 61%), colorless viscous liquid.

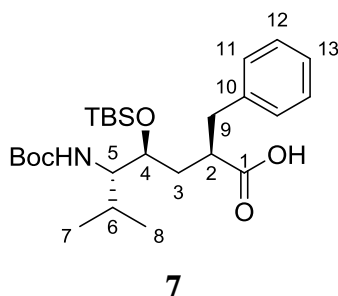
$[\alpha]_D^{23} = -13.0^\circ$ ($c = 1.0$, CHCl₃); lit. $[\alpha]$ not disclosed.

$R_f = 0.60$ (cyclohexane/EtOAc 2:1 (v/v); staining: KMnO₄).

¹H NMR (300 MHz, CDCl₃) $\delta = 7.40\text{--}7.11$ (m, 5H, H-C8, H-C9 and H-C10), 4.55 (d, ³ $J = 10.1$ Hz, 1H, NH), 4.48–4.38 (m, 1H, H-C2), 3.42–3.29 (m, 1H, H-C1), 3.14 (dd, ² $J = 13.5$ Hz, ³ $J = 4.2$ Hz, 1H, H_a-C6), 3.05–2.90 (m, 1H, H-C4), 2.82 (dd, ² $J = 13.5$ Hz, ³ $J = 8.9$ Hz, 1H, H_b-C6), 2.27–2.12 (m, 1H, H_a-C3), 2.11–1.96 (m, 1H, H_b-C3), 1.86–1.69 (m, 1H, H-C11), 1.42 (s, 9H, (CH₃)₃), 0.94 (d, ³ $J = 6.7$ Hz, 6H, H-C12).

¹³C NMR (75 MHz, CDCl₃) $\delta = 179.3$ (s, 1C, C5), 156.4 (s, 1C, HNCO), 138.1 (s, 1C, C7), 129.0 (s, 2C, H-C9), 128.8 (s, 2C, H-C8), 127.0 (s, 1C, H-C10), 79.8 (s, 1C, Me₃C), 78.2 (s, 1C, C2), 59.0 (s, 1C, C1), 41.4 (s, 1C, C4), 37.0 (s, 1C, C6), 31.06 (s, 1C, C3), 30.0 (s, 1C, C11), 28.4 (s, 3C, (CH₃)₃), 19.8 (s, 1C, C12), 19.3 (s, 1C, C12).

(2R,4S,5S)-2-Benzyl-5-[[(*tert*-butoxy)carbonyl]amino]-4-[[(*tert*-butyldimethylsilyl)oxy]-6-methylheptanoic acid (7**) (13)**



Lactone opening: In a 25 mL round-bottom flask, equipped with a Teflon[®]-coated magnetic stirring bar, **6** (500 mg, 1.44 mmol, 1.00 eq) was dissolved in THF (5.3 mL) and stirred vigorously. A 1 M solution of LiOH·H₂O (329 mg, 7.84 mmol, 4.00 eq) in H₂O (7.8 mL) was added dropwise from a syringe within 3 min. TLC indicated full conversion after 70 min. Et₂O (7.8 mL) was added and the biphasic mixture was cooled down to 0 °C in an ice bath. Under vigorous stirring the aqueous phase was carefully adjusted to pH = 4 with 25% aqueous citric acid. The layers were separated and the aqueous layer was extracted with Et₂O

(2×7.8 mL). The combined organic extracts were washed with H₂O (5.0 mL), dried over Na₂SO₄, and concentrated and dried under reduced pressure and temperatures <30 °C to furnish a white solid substance.

Silylation: In a nitrogen-purged 25 mL Schlenk tube equipped with a Teflon[®]-coated magnetic stirring bar, the isolated white solid and *N*-methylimidazole (941 μL, 11.8 mmol, 6.00 eq) were dissolved in absolute CH₂Cl₂ (7.8 mL) and stirred. The solution was cooled to 0 °C in an ice bath and iodine (2.990 g, 11.8 mmol, 6.00 eq) was added. After stirring for 15 min TBSCl (0.886 g, 5.88 mmol, 3.00 eq) was added in portions within 1 min and the cooling bath was removed. TLC indicated full conversion after 14 h. The dark red mixture was transferred into a separation funnel, diluted with Et₂O (25 mL) and treated with saturated aqueous Na₂S₂O₃ (7.8 mL). The organic phase was washed with 25% citric acid (7.8 mL) and brine, concentrated under reduced pressure and dried *in vacuo* to yield a yellow oil.

Silyl ester methanolysis: In a 10 mL round-bottom flask equipped with a Teflon[®]-coated magnetic stirring bar, the yellow oil was dissolved in MeOH (1.0 mL) and 25% citric acid (20 μL) was added. The mixture was stirred until TLC indicated full conversion (22 h). The mixture was concentrated under reduced pressure and purified via flash chromatography (SiO₂, cyclohexane/EtOAc 4:1 to 2:1) to furnish (383 mg, 0.798 mmol, 55% in 3 steps) as a colorless viscous liquid.

Yield: 383 mg (0.798 mmol, 55%, 3 steps), colorless viscous liquid.

$[\alpha]_D^{23} = -17.2^\circ$ (*c* = 1.0, CHCl₃); lit. $[\alpha]$ not disclosed.

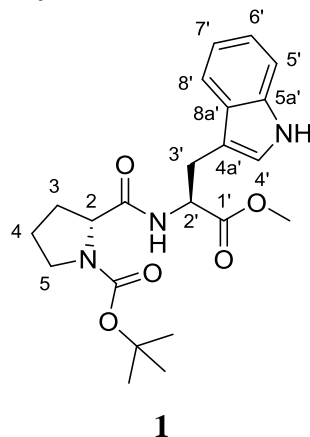
R_f = 0.47 (cyclohexane/EtOAc/AcOH 2:1:0.05 (v/v); staining: KMnO₄).

¹H NMR (300 MHz, CDCl₃, based on HSQC) δ = 7.36–7.10 (m, 5H, H–C11, H–C12 and H–C13), 4.70 (d, ³*J* = 10.1 Hz, 1H, NH), 3.89–3.78 (m, 1H, H–C4), 3.26–3.16 (m, 1H, H–C5), 3.11 (dd, ²*J* = 13.5 Hz, ³*J* = 7.3 Hz, 1H, H_a–C9), 2.87–2.76 (m, 1H, H–C2), 2.71 (dd, ²*J* = 13.5 Hz, ³*J* = 6.1 Hz, 1H, H_b–C9), 1.94–1.77 (m, 1H, H_a–C3), 1.72–1.54 (m, 2H, H_b–C3 and H–C6), 1.44 (s, 9H, (CH₃)₃CO), 0.92 (d, ³*J* = 6.6 Hz, 3H, H–C7), 0.86 (s, 9H, (CH₃)₃CSi), 0.80 (d, ³*J* = 6.6 Hz, 3H, H–C8), 0.04 (s, 3H, CH₃Si), 0.00 (s, 3H, CH₃Si).

¹³C NMR (75 MHz, CDCl₃, based on HSQC) δ = 177.0 (s, 1C, C1), 157.7 (s, 1C, HNCO), 139.4 (s, 1C, C10), 129.1 (s, 2C, H–C12), 128.8 (s, 2C, H–C11), 126.7 (s, 1C, H–C13), 80.3 (s, 1C, Me₃C), 69.6 (s, 1C, C4), 58.8 (s, 1C, C5), 44.0 (s, 1C, C2), 38.1 (s, 1C, C9), 37.6 (s,

1C, C3), 29.6 (s, 1C, C6), 28.6 (s, 3C, (CH₃)₃CO), 26.0 (s, 3C, (CH₃)₃CSi), 20.0 (s, 1C, C7), 18.2 (s, 1C, C8), -3.7 (CH₃Si), -4.5 (CH₃Si).

***tert*-Butyl-(2*S*)-2-[[*(2S)*-3-(1*H*-indol-3-yl)-1-methoxy-1-oxopropan-2-yl]carbamoyl]pyrrolidine-1-carboxylate (**1**) (**14**)**



A 250 mL three-neck round-bottom flask, equipped with a Schlenk adapter, a dropping funnel and a Teflon[®]-coated magnetic stirring bar, was purged with nitrogen. In the flask, Boc-Pro-OH (6.458 g, 30.00 mmol, 1.00 eq) was dissolved in DCM (50 mL), stirred and cooled to 0 °C in an ice bath. Diisopropylcarbodiimide (5.637 mL, 36.00 mmol, 1.20 eq) was added and the resulting mixture was stirred for 10 min. A solution of H-Trp-OMe×HCl (7.641 g, 30.00 mmol, 1.00 eq) and triethylamine (8.363 mL, 60.00 mmol, 2.00 eq) in DCM (50 mL) was added dropwise within 5 min. The reaction mixture was stirred for 2 h and then concentrated under reduced pressure. The residue was dissolved in EtOAc (250 mL) and washed with 1 M HCl (2×125 mL), 0.1 M NaOH (3×125 mL), H₂O (100 mL) and brine (50 mL). The organic phase was dried over Na₂SO₄ and stored in a sealed flask overnight at 4 °C. Subsequently, the solution was cooled to -20 °C for 30 min and filtered to remove a white precipitate. The filtrate was concentrated and dried *in vacuo* to furnish a white solid substance (7.560 g, 18.20 mmol, 61%).

Yield: 7.560 g (18.20 mmol, 61%), white solid.

m.p. = 97–100 °C; lit. m.p. not disclosed.

$[\alpha]_D^{23} = -33.1^\circ$ (c = 1.37, CHCl₃); lit. $[\alpha]$ not disclosed.

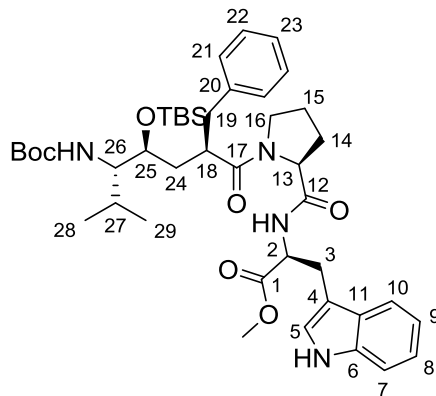
R_f = 0.26 (cyclohexane/EtOAc 1:1 (v/v); staining: KMnO₄).

^1H NMR (300 MHz, CDCl_3 , based on HSQC) δ = 8.37 (br s, 1H, indole NH), 7.52 (d, 3J = 7.7 Hz, 1H, H-C8'), 7.33 (d, 3J = 7.7 Hz, 1H, H-C5'), 7.23–6.89 (m, 3H, H-C5', H-C6' and H-C7'), 6.51 (br s, 1H, HNCO), 4.89 (br s, 1H, H-C2'), 4.34–4.09 (m, 1H, H-C2), 3.67 (s, 3H, CH_3O), 3.42–3.03 (m, 4H, H-C3' and H-C5), 2.31–1.52 (m, 4H, H-C3 and H-C4), 1.38 (s, 9H, $(\text{CH}_3)_3\text{CO}$).

^{13}C NMR (75 MHz, CDCl_3 , based on HSQC) δ = 172.2 (m, 2C, CONH and H-C1'), 154.8 (s, 1C, $\text{CO}_2t\text{-Bu}$), 136.3 (s, 1C, C5a'), 127.7 (s, 1C, C8a'), 122.8 (s, 1C, C4'), 122.3 (s, 1C, C6'), 119.7 (s, 1C, C7'), 118.5 (s, 1C, C8'), 111.4 (s, 1C, C5'), 110.1 (s, 1C, C4a'), 81.2–79.9 (m, 1C, Me₃C), 61.6–59.6 (s, 1C, C2), 53.7–52.5 (m, 1C, C2'), 52.4 (s, 1C, CH_3O), 47.0 (s, 1C, C5), 30.7 (br s, 1C, C3), 28.3 (s, 3C, $(\text{CH}_3)_3\text{CO}$), 27.9 (s, 1C, C3'), 25.1–22.9 (m, 1C, C4).

HPLC-ESI-MS (Agilent Poroshell120; method: fast_Poroshell120_001HCOOH_10to95): $t_R(\mathbf{1})$ = 5.41 min, 100%, $[\text{M} + \text{Na}]^+ = 438$, $[\text{M} + \text{K}]^+ = 454$.

Methyl (2S)-2-{[(2S)-1-[(2R,4S,5S)-2-benzyl-5-[(*tert*-butoxy)carbonyl]amino]-4-[(*tert*-butyldimethylsilyl)oxy]-6-methylheptanoyl]pyrrolidin-2-yl]formamido}-3-(1*H*-indol-3-yl)propanoate (8)



8

In a 5 mL glass vial equipped with a Teflon[®]-coated magnetic stirring bar, (200 mg, 0.481 mmol, 1.20 eq) was dissolved in TFA (1.10 mL). Ethanethiol (357 μL , 4.77 mmol, 1.19 eq) was added and the solution was stirred for 60 min at RT. The volatiles were evaporated, the residue was dried in high vacuum to constant mass to yield deprotected H-Pro-Trp-OMe.

In a nitrogen-purged 10 mL Schlenk tube equipped with a Teflon[®]-coated magnetic stirring bar, (189 mg, 0.400 mmol, 1.00 eq) and Hünig's base (69 μL , 0.40 mmol, 1.0 eq) were

dissolved in absolute DMF (1.60 mL). The solution was stirred, cooled to 0 °C in an ice bath and HBTU (180 mg, 0.47 mmol, 1.20 eq) was added. Immediately after 5 min of activation a solution of the freshly prepared H-Pro-Trp-OMe and Hünig's base (137 μ L, 0.793 mmol, 1.98 eq) in absolute DMF (1.00 mL) was added via syringe and septum. The ice bath was removed and the mixture was stirred for 120 min. Subsequently, brine (2.6 mL) and EtOAc (8.0 mL) were added and the mixture was stirred vigorously for 5 min. The layers were separated and the organic phase washed with brine (3 \times 2.6 mL), dried over Na₂SO₄, and concentrated under reduced pressure. After purification via flash chromatography (SiO₂, CH₂Cl₂/MeOH 80:1 to 20:1) **8** (231 mg, 0.297 mmol) was achieved as a white solid.

Yield: 231 mg (0.297 mmol, 74% from), white solid.

m.p. = 76–79 °C.

$[\alpha]_D^{23} = -22^\circ$ (c = 0.2, CHCl₃).

R_f = 0.38 (CH₂Cl₂/MeOH 20:1 (v/v); staining: KMnO₄).

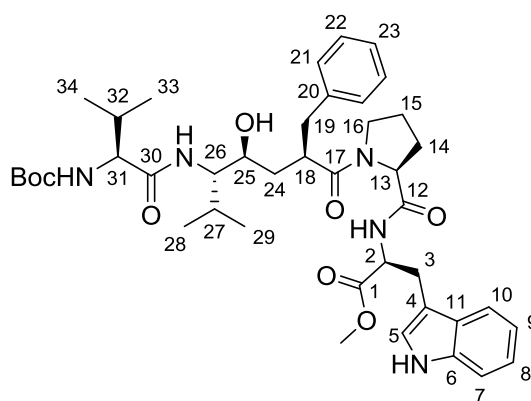
¹H NMR (300 MHz, CDCl₃, based on COSY and HSQC) δ = 8.42 (br s, 1H, indole NH), 7.49 (d, ³J = 7.6 Hz, 1H, H-C10), 7.35–6.98 (m, 10H, H-Ar and HNCO), 4.75–4.64 (m, 2H, HNCO₂ and H-C2), 4.57–4.54 (m, 1H, H-C13), 3.84 (dd, ³J = 9.3 Hz, 3.3 Hz, 1H, H-C25), 3.68 (s, 3H, CH₃O), 3.55–3.41 (m, 1H, H-C16), 3.31–3.20 (m, 2H, H-C3 and H-C26), 3.13 (dd, ²J = 14.6 Hz, ³J = 7.3 Hz, 1H, H-C26), 3.04–2.96 (m, 1H, H-C16), 2.86–2.83 (m, 1H, H-C18), 2.65 (dd, ²J = 13.4 Hz, ³J = 8.1 Hz, 1H, H-C19), 2.44 (dd, ²J = 13.4 Hz, ³J = 5.7 Hz, 1H, H-C19), 2.27–2.14 (m, 1H, H-C14), 1.87–1.55 (m, 6H, H₂-C15, H-C14, H₂-C24 and H-C27), 1.44 (s, 9H, (CH₃)₃C), 0.94 (d, ³J = 6.7 Hz, 3H, H-C28), 0.87 (s, 9H, (CH₃)₃CSi), 0.83 (d, ³J = 6.6 Hz, 3H, H-C29), 0.06 (s, 3H, CH₃Si), 0.02 (s, 3H, CH₃Si).

¹³C NMR (75 MHz, CDCl₃, based on COSY, HSQC and HMBC) δ = 174.9 (s, 1C, C=O), 172.5 (s, 1C, C=O), 171.1 (s, 1C, C=O), 156.7 (s, 1C, CO₂t-Bu), 139.5 (s, 1C, C20), 136.3 (s, 1C, C6), 129.0 (s, 2C, C22), 128.7 (s, 2C, C21), 127.6 (s, 1C, C11), 126.7 (s, 1C, C23), 123.7 (s, 1C, C5), 122.1 (s, 1C, C8), 119.5 (s, 1C, C9), 118.7 (s, 1C, C10), 111.3 (s, 1C, C7), 110.1 (s, 1C, C4), 79.1 (s, 1C, Me₃C), 69.4 (s, 1C, C25), 59.9 (s, 1C, C13), 58.5 (s, 1C, C26), 53.4 (s, 1C, C2), 52.3 (s, 1C, CH₃O), 47.1 (s, 1C, C16), 42.4 (s, 1C, C18), 38.2 (s, 1C, C19), 36.6 (s, 1C, 24), 30.2 (s, 1C, C27), 28.5 (s, 3C, (CH₃)₃CO), 27.7 (s, 1C, C3), 27.3 (s, 1C, C14),

26.0 (s, 3C, (CH₃)₃CSi), 24.8 (s, 1C, C15), 20.0 (s, 1C, C28), 19.8 (s, 1C, C29), 18.2 (s, 1C, (CH₃)₃CSi), -3.66 (CH₃Si), -4.61 (CH₃Si).

HRMS (ESI): m/z (%): 777.4620 (87%, [M + H]⁺, calcd for C₄₃H₆₅N₄O₇Si⁺: 777.4617), 799.4441 (100%, [M + Na]⁺, calcd for C₄₃H₆₄N₄NaO₇Si⁺: 799.4442), 815.4184 (100%, [M + K]⁺, calcd for C₄₃H₆₄KN₄O₇Si⁺: 815.4181).

Methyl (2S)-2-[[[(2S)-1-[(2R,4S,5S)-2-benzyl-5-[(2S)-2-[[[(tert-butoxy)carbonyl]amino]-3-methylbutanamido]-4-hydroxy-6-methylheptanoyl]pyrrolidin-2-yl]formamido]-3-(1H-indol-3-yl)propanoate (9)



9

Deprotection: In a 5 mL glass vial equipped with a Teflon[®]-coated magnetic stirring bar, **8** (132 mg, 0.170 mmol, 1.00 eq) was dissolved in 2,2,2-trifluoroethanol (1.7 mL). Ethanethiol (51 μL, 0.68 mmol, 4.0 eq) and ZnBr₂ were added, and the solution was stirred for 4 h at RT, accompanied with formation of a white precipitate. Subsequently, the reaction mixture was treated with 25% aqueous ammonia (0.80 mL). After EtOAc (5.1 mL) was added, the mixture was transferred into a 20 mL Erlenmeyer flask and stirred vigorously for 5 min. The layers were separated, and the aqueous layer was extracted with EtOAc (2×3.4 mL). The combined organic extracts were dried over Na₂SO₄, concentrated under reduced pressure and the residue was dried in high vacuum to constant mass to yield the crude deprotected intermediate as a white amorphous solid (97 mg).

Coupling: In an oven-dried, nitrogen-purged 10 mL Schlenk tube, equipped with a Teflon[®]-coated magnetic stirring bar, Boc-Val-OH (44 mg, 0.20 mmol, 1.2 eq) and Hünig's base (30 μL, 0.17 mmol, 1.0 eq) were dissolved in absolute DMF (0.70 mL) and stirred at RT. A solution of HATU (78 mg, 0.20 mmol, 1.2 eq) in abs. DMF (0.70 mL) was added and the

reaction solution was stirred for 1 min before a solution of the deprotected intermediate and Hünig's base (30 μ L, 0.17 mmol, 1.0 eq) in abs. DMF (1.00 mL) was added. After TLC indicated full conversion of the intermediate (15 min), the reaction was quenched by addition of brine (1.0 mL) and extracted with EtOAc (3 \times 3.6 mL). The combined organic extracts were washed with brine (3 \times 1.0 mL), dried over Na₂SO₄, and concentrated under reduced pressure. Purification via flash chromatography (SiO₂, CH₂Cl₂/MeOH 50:1 to 20:1) furnished (68 mg, 0.089 mmol) as a white solid.

Yield: 68 mg (0.089 mmol, 52%, 2 steps, from **8**), white solid.

m.p. = 90–93 °C.

$[\alpha]_D^{23} = -26.4^\circ$ (c = 0.23, CHCl₃).

R_f = 0.51 (CH₂Cl₂/MeOH 10:1 (v/v); staining: KMnO₄).

¹H NMR (300 MHz, CDCl₃, complex mixture of signals of 2 rotamers in 1.2:1 ratio, assigned based on COSY, HSQC, HMBC and EXSY) δ = 9.19 and 8.63 (br s, 1H, indole NH), 7.60–7.47 (m, 1H, H–C10), 7.46–6.97 (m, 7.5H, H–Ar and amide H from *cis*-rotamer's Trp), 6.54–6.31 (m, 1H, H–Ar), 6.12 (d, ³J = 7.3 Hz, 0.5H, amide H from *trans*-rotamer's Trp), 5.19–4.97 (m, 1H, carbamate H), 4.86–4.68 (m, 1H, H–C2), 4.58–4.27 (m and br s, 1.5H, H–C13 from one rotamer, and OH), 3.89–3.73 (m, 2H, H–C31 and H–C25), 3.76 and 3.68 (s, 3H, CH₃O), 3.56–2.38 (m, 8.5H, H₂–C3, H–C13 from one rotamer, H₂–C16, H–C18, H₂–C19, H–C26), 2.34–1.05 (m, 17H, H₂–C14, H₂–C15, H₂–C24, H–C27, H–C32 and (CH₃)₃C), 1.04–0.72 (m, 12H, H₃–C28, H₃–C29, H₃–C33 and H₃–C34).

¹³C NMR (75 MHz, CDCl₃, complex mixture of signals of 2 rotamers, assigned based on COSY, HSQC, HMBC and EXSY) δ = 176.2 and 175.2 (s, 1C, C17), 172.9, 172.5, 172.4, 172.2, 172.1 and 170.7 (s, 3C, 2 amide C=O and an ester C=O), 156.2–156.0 (m, 1C, carbamate C=O), 139.1 and 138.8 (s, 1C, C20), 136.5 and 136.4 (s, 1C, C6), 128.9 and 128.8 (s, 2C, C22), 128.6 (s, 2C, C21), 127.6 and 127.5 (s, 1C, C11), 126.7 and 126.6 (s, 1C, C23), 123.8 and 123.0 (s, 1C, C5), 122.4 and 122.1 (s, 1C, C8), 119.8 and 119.5 (s, 1C, C9), 118.5 and 118.1 (s, 1C, C10), 111.8 and 111.4 (s, 1C, C7), 109.7 and 109.5 (s, 1C, C4), 80.3–79.9 (m, 1C, Me₃C), 67.3 and 67.0 (s, 1C, C25), 61.1–60.6 (m, 1C, C31), 60.5 and 59.8 (s, 1C, C13), 60.0 and 59.7 (s, 1C, C26), 53.4 and 53.2 (s, 1C, C2), 52.8 and 52.4 (s, 1C, CH₃O), 47.5 and 46.4 (s, 1C, C16), 43.3 and 42.7 (s, 1C, C18), 40.0 and 37.8 (s, 1C, C19), 37.8 and 35.9

(s, 1C, 24), 31.3 and 27.5 (s, 1C, C14), 30.4, 30.1 and 29.8 (s, 2C, C27 and C32), 28.7–28.1 (m, 3C, (CH₃)₃CO), 27.6 and 26.9 (s, 1C, C3), 24.9 and 22.0 (s, 1C, C15), 20.2–20.0, 19.9–19.6, 19.3–19.2 and 18.0–17.7 (m, 4C, C33, C34, C28, C29).

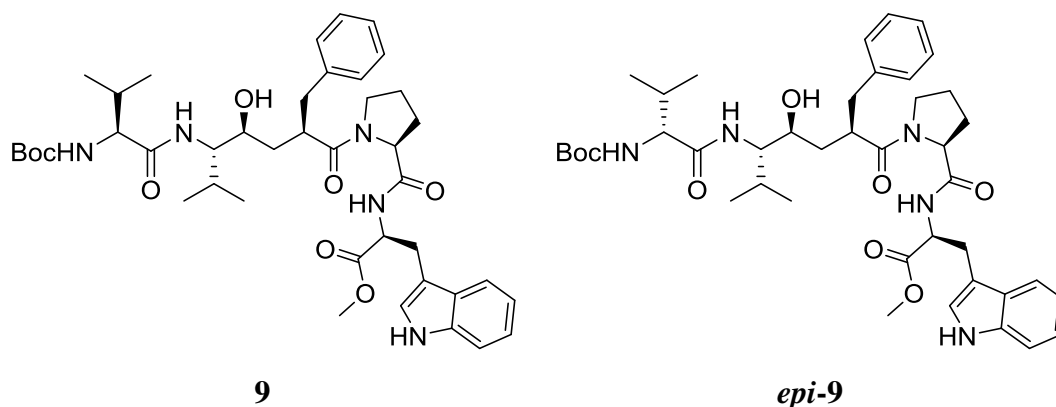
HPLC-ESI-MS (Agilent Poroshell120; method: SHE_Poroshell120_HCOOHMeCN_40_60_95): $t_R(\mathbf{9}) = 7.62$ min, 100%, $[M + Na]^+ = 785$, $[M + K]^+ = 801$; $t_R(\textit{epi-9}) = 7.79$ min, no abundance detected; de >99%, based on comparison to the HPLC-ESI-MS trace of reference epimer mixture (*vide infra*).

HRMS (ESI): m/z (%): 784.4257 (100%, $[M + Na]^+$, calcd for C₄₂H₅₉N₅NaO₈⁺: 784.4261).

Reference epimer mixture microsynthesis:

Methyl (2S)-2-[[[(2S)-1-[(2R,4S,5S)-2-benzyl-5-[(2S)-2-[[[(*tert*-butoxy)carbonyl]amino]-3-methylbutanamido]-4-hydroxy-6-methylheptanoyl]pyrrolidin-2-yl]formamido]-3-(1H-indol-3-yl)propanoate (9**) and**

Methyl (2S)-2-[[[(2S)-1-[(2R,4S,5S)-2-benzyl-5-[(2R)-2-[[[(*tert*-butoxy)carbonyl]amino]-3-methylbutanamido]-4-hydroxy-6-methylheptanoyl]pyrrolidin-2-yl]formamido]-3-(1H-indol-3-yl)propanoate (*epi-9*)



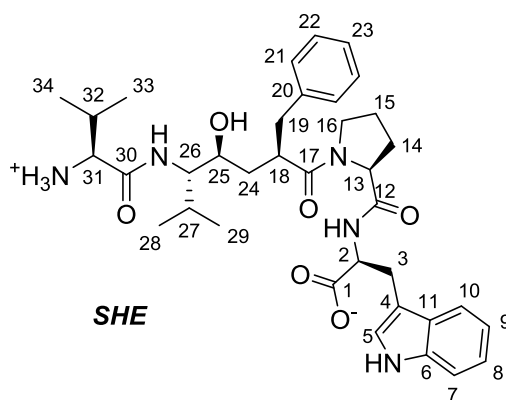
According to the procedure for preparation of **9**, in a 1.5 mL glass vial, equipped with a small Teflon[®]-coated magnetic stirring bar, an aliquot (88 μ L, 1.2 eq) of a stock solution of Boc-DL-Val-OH (5.0 mg, 0.023 mmol) in absolute DMF (1.00 mL) was treated with an aliquot (7 μ L, 1.2 eq) of a stock solution of HATU (78 mg, 0.21 mmol) in absolute DMF (0.70 mL) using microliter-syringes. The mixture was stirred for 1 min and then immediately treated with an aliquot (10 μ L) of the solution of the crude deprotected intermediate in absolute DMF (97 mg in 1.00 mL, from the preparation of). After 15 min, the reaction was quenched by the

addition of water (200 μL) and extracted with EtOAc (500 μL). The organic layer was separated, and evaporated under reduced pressure. The residue was dissolved in 1000 μL of MeCN and analyzed by TLC and HPLC-ESI-MS.

$R_f = 0.51$ ($\text{CH}_2\text{Cl}_2/\text{MeOH}$ 10:1 (v/v); staining: KMnO_4).

HPLC-ESI-MS (Agilent Poroshell120; method: SHE_Poroshell120_HCOOHMeCN_40_60_95): $t_R(\mathbf{9}) = 7.61$ min, 48.2%, $[\text{M} + \text{Na}]^+ = 785$, $[\text{M} + \text{K}]^+ = 801$; $t_R(\textit{epi-9}) = 7.79$ min, 47.1% $[\text{M} + \text{Na}]^+ = 785$, $[\text{M} + \text{K}]^+ = 801$.

(2S)-2-[[[(2S)-1-[(2R,4S,5S)-5-[(2S)-2-Azaniumyl-3-methylbutanamido]-2-benzyl-4-hydroxy-6-methylheptanoyl]pyrrolidin-2-yl]formamido]-3-(1H-indol-3-yl)propanoate
(10)



10

Saponification: In a 5 mL glass vial equipped with a Teflon[®]-coated magnetic stirring bar, **9** (46 mg, 0.060 mmol, 1.0 eq) was dissolved in THF (0.24 mL). A solution of $\text{LiOH} \times \text{H}_2\text{O}$ (21 mg, 0.48 mmol, 8.0 eq) in H_2O (0.40 mL) was added and the mixture was stirred vigorously until TLC indicated full conversion (15 min). The solution was adjusted to pH = 4 with AcOH. The stirring was stopped and the white colloidal mixture was extracted with Et_2O (3 \times 2 mL). The combined organic extracts were dried over Na_2SO_4 , concentrated under reduced pressure and dried in high vacuum to constant mass to yield a saponified intermediate as an off-white powder (40 mg, m.p. = 121–124 $^\circ\text{C}$).

Boc-deprotection: In a 5 mL glass vial equipped with a Teflon[®]-coated magnetic stirring bar, the saponified intermediate (40 mg) was dissolved in 2,2,2-trifluoroethanol (1.20 mL). Under vigorous stirring ethanethiol (18 μL , 0.24 mmol, 4.0 eq) and ZnBr_2 (108 mg, 0.480 mmol, 8.0

eq) were added. The reaction mixture was stirred vigorously for 10 h and a white precipitate formed. The mixture was concentrated under reduced pressure and the residue was dissolved in water (1.20 mL) and MeOH (200 μ L). Purification via preparative reverse phase HPLC (method: JKV_NucleodurC18_001HCOOH_10to85) afforded **10** (18 mg, 0.028 mmol, 46%, 2 steps) as a white solid.

Yield: 18 mg (0.028 mmol, 46%, 2 steps, from **9**), white solid.

m.p. = 151–155 °C

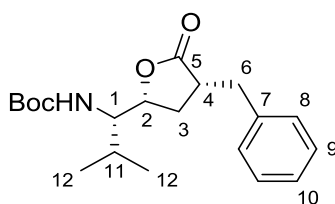
$[\alpha]_D^{23} = -24^\circ$ (c = 0.61, MeOH).

^1H NMR (300 MHz, methanol- d_4 /D $_2$ O 5:1, complex mixture of signals of cabamate rotamers and intramolecular interaction stabilized conformers in equilibrium, assigned based on COSY and HSQC) $\delta = 7.69$ – 7.55 (m, 1H, H–C10), 7.41 – 6.89 (m, 9H, H–Ar), 4.65 – 4.37 (m, 1H, H–C2), 3.83 – 2.58 (m, 11H, H–C13, H–C31, H–C25, H $_2$ –C3, H $_2$ –C16, H–C18, H $_2$ –C19, H–C26), 2.36 – 2.18 (m, 1H, H–C32), 2.11 – 1.14 (m, 7H, H $_2$ –C14, H $_2$ –C15, H $_2$ –C24 and H–C27), 1.14 – 0.76 (m, 12H, H $_3$ –C28, H $_3$ –C29, H $_3$ –C33 and H $_3$ –C34).

^{13}C NMR (75 MHz, methanol- d_4 /D $_2$ O 5:1, complex mixture of signals of cabamate rotamers and intramolecular interaction conformers in equilibrium, assigned based on COSY and HSQC) $\delta = 177.2$, 176.4 , 173.6 and 169.2 (s, 4C, 3 amide C=O and an ester C=O), 140.0 (s, 1C, C20), 137.9 (s, 1C, C6), 130.4 – 126.7 (m, 6C, C11, C21, C22 and C23), 124.4 (s, 1C, C5), 122.4 (s, 1C, C8), 119.8 (s, 1C, C9), 119.6 (s, 1C, C10), 112.3 (s, 1C, C7), 68.6 (s, 1C, C25), 62.3 – 61.9 (m, 2C, C31 and C13), 47.5 (s, 1C, C16), 44.2 (s, 1C, C18), 42.8 (s), 41.4 (s, 1C, C19), 40.4 , 39.2 (s, 1C, C24), 37.4 (s, 1C, C2), 32.2 (s, 1C, C14), 31.6 (s, 1C, C32), 30.6 (s, 1C, C27), 28.6 (s, 1C, C3), 22.4 (s, 1C, C15), 20.8 – 17.5 (m, 4C, C33, C34, C28, C29).

HPLC-ESI-MS (Agilent Poroshell120; method: fast_Poroshell_001HCOOH_8mingradient.lc): $t_R(\mathbf{10}) = 5.54$ min, 100%, $[\text{M} + 1]^+ = 648$, $[\text{M} + \text{Na}]^+ = 670$.

HRMS (ESI): m/z (%): 648.3756 (100%, $[\text{M} + 1]^+$, calcd for $\text{C}_{36}\text{H}_{50}\text{N}_5\text{O}_6^+$: 648.3756), 670.3577 (100%, $[\text{M} + \text{Na}]^+$, calcd for $\text{C}_{36}\text{H}_{49}\text{N}_5\text{NaO}_6^+$: 670.3575).

(ii) Synthesis of *HER**tert*-Butyl-*N*-[(1*S*)-1-[(2*R*,4*R*)-4-benzyl-5-oxooxolan-2-yl]-2-methylpropyl]carbamate (**11**)**11**

Aldol reaction: In an oven dried, nitrogen purged 100 mL two-neck round-bottom flask, equipped with a dropping funnel, a gas valve adapter and a Teflon[®]-coated magnetic stirring bar, **5** (1.03 g, 4.00 mmol, 1.00 eq) was dissolved in absolute THF (29.9.8 mL), stirred and cooled to -78 °C in an acetone/dry ice bath. 1.0 M LiHMDS solution in hexanes (8.00 mL, 8.00 mmol, 2.00 eq) was added dropwise within 20 min and the resulting solution was stirred for 20 min. A solution of benzaldehyde (813 μL, 8.00 mmol, 2.00 eq) in THF (10.3 mL) was charged into the dropping funnel and added dropwise to the reaction mixture within 15 min. The resulting reaction solution was stirred at -78 °C until TLC indicated full conversion of lactone **5** (60 min). The reaction solution was poured into a vigorously stirred 3 M NH₄Cl aqueous solution (20 mL). The mixture was extracted with EtOAc (2×40 mL). The combined organic extracts were washed with 1 M HCl (20 mL), saturated aqueous NaHCO₃ (20 mL), brine (10 mL), dried over Na₂SO₄, and concentrated and dried under reduced pressure. Purification via flash chromatography (SiO₂, cyclohexane/EtOAc 4:1 to 2:1) furnished a mixture of 4 aldol diastereomers (528 mg, 1.75 mmol, 44%) as a pale yellow viscous liquid.

Mesylation: In an oven dried, nitrogen purged 20 mL Schlenk tube, equipped with a Teflon[®]-coated magnetic stirring bar, the mixture of aldol diastereomers (472 mg, 1.30 mmol, 1.00 eq) was dissolved in absolute CH₂Cl₂ (6.5 mL), stirred and cooled to 0 °C in an ice bath. Methanesulfonyl chloride (201 μL, 2.60 mmol, 2.00 eq) was added dropwise *via* syringe within 10 min and, subsequently, triethylamine (544 μL, 3.90 mmol, 3.00 eq) was added dropwise *via* syringe within 2 min. The resulting solution was stirred overnight in the warming ice bath, reaching RT. Additional methanesulfonyl chloride (201 μL, 2.60 mmol, 2.00 eq) and triethylamine (544 μL, 3.90 mmol, 3.00 eq) were added and the reaction solution was stirred again overnight to complete the conversion. The reaction was quenched by the addition of ice-cold water (4.0 mL). The resulting biphasic mixture was extracted with EtOAc

(2×13 mL), the combined organic extracts were washed with brine (4.0 mL), dried over Na₂SO₄, and concentrated under reduced pressure to afford a brown oily residue (571 mg), which was composed of a diastereomeric mixture of β'-chlorolactones and the desired elimination intermediates (based on HPLC-MS and NMR analysis of the crude mixture).

Elimination: In a 10 mL round-bottom flask, equipped with a reflux condenser and a Teflon[®]-coated magnetic stirring bar, the crude intermediate mixture was dissolved in EtOH (5.2 mL). Triethylamine (172 μL, 1.24 mmol, 0.95 eq) was added and the reaction mixture was heated overnight at 50 °C in an oil bath. After concentration *in vacuo*, the residue was partitioned between EtOAc (10 mL) and water (4.0 mL) and the aqueous layer extracted with EtOAc (5.0 mL). The combined organic layers were washed with brine (5 mL) and concentrated under reduced pressure to furnish a viscous oily residue containing only the desired elimination intermediate diastereomers (based on HPLC-MS and NMR analysis of the crude mixture).

Hydrogenation: In a 50 mL two-neck round-bottom flask, equipped with a gas valve adaptor and a mechanical stirring apparatus, the crude intermediate mixture was dissolved in THF (15.2 mL). A portion of aqueous slurry of Raney-Ni (1.0 mL) was pipetted into a test tube, the water was decanted and the mass of the tube was recorded. Wet Raney-Ni was suspended in THF (1.0 mL), transferred into the reaction flask and the mass of the tube was recorded again to determine the difference which corresponds to the mass of Raney-Ni (17 mg). The apparatus was first purged with nitrogen and then with hydrogen, and the reaction mixture was stirred vigorously at RT overnight, under hydrogen atmosphere. The reaction flask was disconnected from the hydrogen balloon and purged with N₂. Under nitrogen atmosphere the content of the flask was transferred to the nitrogen-purged fritted Schlenk type funnel containing a 2 cm thick compressed bed of Celite[®]. The product was eluted from the filter cake with THF (3×5 mL). The Celite[®] bed with the solid catalyst was washed with water (5 mL), and stored under water in a container dedicated for catalyst waste. The product-containing filtrate was evaporated under reduced pressure, and the residue was purified via flash chromatography (SiO₂, cyclohexane/EtOAc 9:1 to 4:1) to furnish a white solid **11** (311 mg, 0.895 mmol, 30%, 4 steps).

Yield: 311 mg (0.895 mmol, 30%, in 4 steps from **5**), white solid.

m.p. = 83–86 °C.

$[\alpha]_D^{23} = -50.8^\circ$ ($c = 0.7$, CHCl_3).

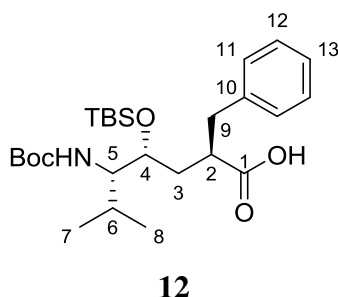
$R_f = 0.42$ (cyclohexane/EtOAc 2:1 (v/v); staining: KMnO_4).

$^1\text{H NMR}$ (300 MHz, CDCl_3 , based on COSY and HSQC) $\delta = 7.39\text{--}7.10$ (m, 5H, H-C8, H-C9 and H-C10), 4.31 (d, $^3J = 9.9$ Hz, 1H, NH), 4.25–4.03 (m, 1H, H-C2), 3.75–3.54 (m, 1H, H-C1), 3.31 (dd, $^2J = 13.5$ Hz, $^3J = 2.7$ Hz, 1H, $\text{H}_a\text{-C6}$), 2.95–2.77 (m, 1H, H-C4), 2.77–2.60 (m, 1H, $\text{H}_b\text{-C6}$), 2.33–2.18 (m, 1H, $\text{H}_a\text{-C3}$), 2.15–1.98 (m, 1H, H-C11), 1.95–1.76 (m, 1H, $\text{H}_b\text{-C3}$), 1.43 (s, 9H, $(\text{CH}_3)_3$), 0.94 (d, $^3J = 6.8$ Hz, 3H, H-C12), 0.85 (d, $^3J = 6.9$ Hz, 3H, H-C12).

$^{13}\text{C NMR}$ (75 MHz, CDCl_3 , based on COSY and HSQC) $\delta = 177.8$ (s, 1C, C5), 156.1 (s, 1C, HNCO), 138.9 (s, 1C, C7), 129.0 (s, 2C, H-C9), 128.8 (s, 2C, H-C8), 126.8 (s, 1C, H-C10), 79.9 (s, 1C, Me_3C), 78.2 (s, 1C, C2), 58.3 (s, 1C, C1), 42.7 (s, 1C, C4), 36.5 (s, 1C, C6), 32.2 (s, 1C, C3), 28.6–28.3 (m, 4C, C11 and $(\text{CH}_3)_3$), 20.0 (s, 1C, C12), 16.0 (s, 1C, C12).

HRMS (ESI): m/z (%): 370.1987 (100%, $[\text{M} + \text{Na}]^+$, calcd for $\text{C}_{20}\text{H}_{29}\text{NNaO}_4^+$: 370.1989).

(2R,4R,5S)-2-Benzyl-5-[[(*tert*-butoxy)carbonyl]amino]-4-[(*tert*-butyldimethylsilyl)oxy]-6-methylheptanoic acid (12**)**



Lactone opening: In a 10 mL round-bottom flask, equipped with a Teflon[®]-coated magnetic stirring bar, **11** (108 mg, 0.42 mmol, 1.00 eq) was dissolved in THF (1.4 mL) and stirred vigorously. A 1 M solution of $\text{LiOH}\cdot\text{H}_2\text{O}$ (70 mg, 1.7 mmol, 4.0 eq) in H_2O (2.1 mL) was added dropwise via syringe. After TLC indicated full conversion (90 min), Et_2O (4.0 mL) was added and the biphasic mixture was cooled down to 0°C in an ice bath. Under vigorous stirring, the acidity of the aqueous phase was carefully adjusted to $\text{pH}=4$ with 25% aqueous citric acid. The layers were separated and the aqueous layer was extracted with Et_2O (2×3.0 mL). The combined organic extracts were washed with H_2O (3.0 mL) and brine (3.0 mL),

dried over Na₂SO₄, and concentrated and dried under reduced pressure and temperatures <30 °C to furnish a white solid substance.

Silylation: In a nitrogen-purged 10 mL Schlenk tube, equipped with a Teflon[®]-coated magnetic stirring bar, the isolated white solid and *N*-methylimidazole (201 μL, 2.52 mmol, 6.00 eq) were dissolved in absolute CH₂Cl₂ (1.7 mL). The solution was cooled to 0 °C in an ice bath and iodine (640 mg, 2.52 mmol, 6.00 eq) was added. After stirring for 15 min, TBSCl (190 mg, 1.26 mmol, 3.00 eq) was added in portions within 1 min. The cooling bath was removed and the deep-red mixture stirred overnight. The dark red mixture was transferred into a separation funnel, diluted with Et₂O (4.0 mL) and washed with saturated aqueous Na₂S₂O₃ (3.0 mL). The organic phase was washed with 25% citric acid (3.0 mL) and brine (3.0 mL), concentrated under reduced pressure and dried *in vacuo* to yield a yellow oily residue.

Silyl ester methanolysis: In a 5 mL glass vial, equipped with a Teflon[®]-coated magnetic stirring bar, the yellow oil was dissolved in MeOH (1.1 mL) and 25% citric acid (32 μL) was added. The mixture was stirred until TLC indicated full conversion (6 h) of the least polar component observable. The mixture was concentrated under reduced pressure and purified via flash chromatography (SiO₂, CH₂Cl₂/MeOH/AcOH 100:1:0.5) to furnish **12** (102 mg, 0.213 mmol, 51% in 3 steps) as a colorless viscous oil.

Yield: 102 mg (0.213 mmol, 51%, in 3 steps from **11**), colorless viscous oil.

$[\alpha]_D^{23} = -5.5^\circ$ (c = 0.7, CHCl₃).

R_f = 0.14 (CH₂Cl₂/MeOH/AcOH 100:3:0.5 (v/v); staining: KMnO₄).

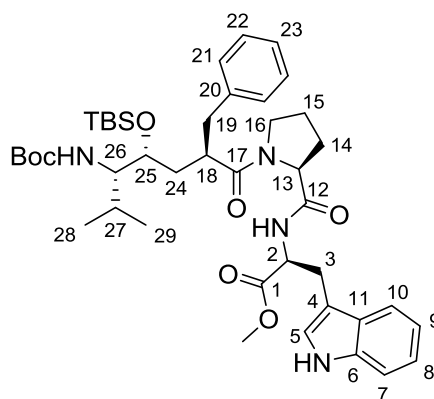
¹H NMR (300 MHz, CDCl₃, mixture of 2 rotamers, based on COSY, HSQC and EXSY) δ = 7.37–7.11 (m, 5H, H–C11, H–C12 and H–C13), 6.17 and 4.61 (d, ³J = 9.9 Hz, 1H, NH), 3.86–3.66 (m, 1H, H–C4), 3.52–3.23 (m, 1H, H–C5), 3.12–2.93 (m, 1H, H_a–C9), 2.87–2.66 (m, 2H, H–C2 and H_b–C9), 2.00–1.76 (m, 1H, H_a–C3), 1.74–1.50 (m, 2H, H_b–C3 and H–C6), 1.43 (s, 9H, (CH₃)₃CO), 0.88 (s, 9H, (CH₃)₃CSi), 0.84–0.70 (m, H–C7 and H–C8), 0.15–0.01 (s, 6H, (CH₃)₂Si).

¹³C NMR (75 MHz, CDCl₃, mixture of 2 rotamers, citing major rotamer based on COSY, HSQC and EXSY) δ = 179.0 (s, 1C, C1), 156.2 (s, 1C, HNCO), 138.8 (s, 1C, C10), 129.1 (s, 2C, H–C12), 128.6 (s, 2C, H–C11), 126.7 (s, 1C, H–C13), 79.4 (s, 1C, Me₃C), 71.9 (s, 1C,

C4), 58.0 (s, 1C, C5), 43.5 (s, 1C, C2), 38.6 (s, 1C, C9), 35.3 (s, 1C, C3), 28.6 (s, 3C, (CH₃)₃CO), 28.1 (s, 1C, C6), 26.0 (s, 3C, (CH₃)₃CSi), 20.9 (s, 1C, C7), 18.1 (s, 1C, C8), -4.3 (CH₃Si), -4.6 (CH₃Si).

HRMS (ESI): m/z (%): 502.2956 (100%, [M + Na]⁺, calcd for C₂₆H₄₅NNaO₅Si⁺: 502.2959).

Methyl (2R)-2-[[[(2S)-1-[(2R,4S,5S)-2-benzyl-5-[[[(tert-butoxy)carbonyl]amino]-4-[(tert-butyl)dimethylsilyl]oxy]-6-methylheptanoyl]pyrrolidin-2-yl]formamido]-3-(1H-indol-3-yl)propanoate (13)



13

In a 5 mL glass vial equipped with a Teflon[®]-coated magnetic stirring bar, **1** (110 mg, 0.260 mmol, 1.20 eq) was dissolved in TFA (508 μ L), ethanethiol (165 μ L, 2.20 mmol, 10 eq) was added, and the solution was stirred for 60 min at RT. The volatiles were evaporated, the residue was dried in high vacuum to constant mass to yield a deprotected H-Pro-Trp-OMe.

In a nitrogen-purged 10 mL Schlenk tube equipped with a Teflon[®]-coated magnetic stirring bar, **12** (106 mg, 0.220 mmol, 1.00 eq) and Hünig's base (38 μ L, 0.22 mmol, 1.0 eq) were dissolved in absolute DMF (1.00 mL). The solution was stirred, cooled to 0 °C in an ice bath and HBTU (100 mg, 0.260 mmol, 1.20 eq) was added. Immediately after 5 min of activation a solution of the freshly prepared H-Pro-Trp-OMe and Hünig's base (77 μ L, 0.44 mmol, 2.0 eq) in absolute DMF (0.47 mL) was added via syringe and septum. The ice bath was removed and the mixture was stirred for 60 min. Subsequently, brine (2.0 mL) and EtOAc (6.0 mL) were added, and the mixture was stirred vigorously for 5 min. The layers were separated and the organic phase was washed with brine (3 \times 2.0 mL), dried over Na₂SO₄, and concentrated under reduced pressure. Purification via flash chromatography (SiO₂, CH₂Cl₂/MeOH 100:3) furnished **13** (91 mg, 0.12 mmol, 53%) as a white solid.

Yield: 91 mg (0.12 mmol, 53% from **12**), white solid.

m.p. = 55–58 °C

$[\alpha]_D^{23} = -3.0^\circ$ (c = 1.12, CHCl₃).

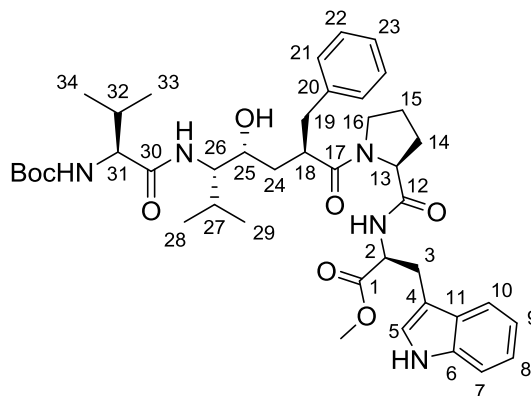
R_f = 0.36 (CH₂Cl₂/MeOH 10:1 (v/v); staining: KMnO₄).

¹H NMR (300 MHz, CDCl₃, only *trans*-Pro rotamer observable, based on HSQC) δ = 8.15 (br s, 1H, indole NH), 7.53 (d, ³J = 7.0 Hz, 1H, H-C10), 7.34 (d, ³J = 6.1 Hz, 1H, amide NH), 7.30–6.90 (m, 9H, H-Ar), 4.82–4.71 (m, 1H, H-C2), 4.62–4.47 (m, 2H, H-C13 and carbamate NH), 3.75–3.58 (m, 4H, CH₃O and H-C25), 3.57–3.42 (m, 1H, H_a-C16), 3.40–3.15 (m, 3H, H₂-C3 and H-C26), 3.00–2.87 (m, 1H, H_b-C16), 2.80–2.67 (m, 1H, H-C18), 2.67–2.45 (m, 1H, H-C19), 2.29–2.14 (m, 1H, H_a-C14), 1.97–1.50 (m, 6H, H_a-C14, H₂-C15, H₂-C24 and H-C27), 1.40 (s, 9H, (CH₃)₃C), 0.99–0.71 (m, 15H, (CH₃)₃CSi, H₃-C28 and H₃-29), 0.11 (s, 3H, CH₃Si), 0.07 (s, 3H, CH₃Si).

¹³C APT NMR (75 MHz, CDCl₃, only *trans*-Pro rotamer observable, based on HSQC) δ = 175.0 (s, 1C, C=O), 172.5 (s, 1C, C=O), 171.2 (s, 1C, C=O), 156.0 (s, 1C, carbamate C=O), 139.2 (s, 1C, C20), 136.2 (s, 1C, C6), 129.0 (s, 2C, C22), 128.5 (s, 2C, C21), 127.8 (s, 1C, C11), 126.6 (s, 1C, C23), 123.5 (s, 1C, C5), 122.2 (s, 1C, C8), 119.6 (s, 1C, C9), 118.7 (s, 1C, C10), 111.3 (s, 1C, C7), 110.3 (s, 1C, C4), 79.0 (s, 1C, Me₃C), 72.2 (s, 1C, C25), 60.1 (s, 1C, C13), 57.7 (s, 1C, C26), 53.5 (s, 1C, C2), 52.4 (s, 1C, CH₃O), 47.3 (s, 1C, C16), 42.0 (s, 1C, C18), 39.0 (s, 1C, C19), 35.5 (s, 1C, 24), 28.5 (s, 3C, (CH₃)₃CO), 27.8 (s, 1C, C27), 27.6 (s, 1C, C3), 27.4 (s, 1C, C14), 26.0 (s, 3C, (CH₃)₃CSi), 24.9 (s, 1C, C15), 21.4 (s, 1C, C28), 18.4 (s, 1C, C29), 18.1 (s, 1C, (CH₃)₃CSi), -4.1 (CH₃Si), -4.7 (CH₃Si).

HRMS (ESI): m/z (%): 799.4442 (100%, [M + Na]⁺, calcd for C₄₃H₆₄N₄NaO₇Si⁺: 799.4442).

Methyl (2R)-2-[[[(2S)-1-[(2R,4S,5S)-2-benzyl-5-[(2S)-2-[[[(tert-butoxy)carbonyl]amino]-3-methylbutanamido]-4-hydroxy-6-methylheptanoyl]pyrrolidin-2-yl]formamido]-3-(1H-indol-3-yl)propanoate (14)



14

Deprotection: In a 5 mL glass vial equipped with a Teflon[®]-coated magnetic stirring bar, **13** (97 mg, 0.125 mmol, 1.00 eq) was dissolved in 2,2,2-trifluoroethanol (1.3 mL). Ethanethiol (37 μ L, 0.50 mmol, 4.0 eq) and ZnBr₂ (197 mg, 0.875 mmol, 7.00 eq) were added, and the solution was stirred for 7 h at RT, accompanied with formation of a white precipitate. Subsequently, the reaction mixture was treated with 25% aqueous ammonia (2.0 mL) to adjust to pH=11. After stirring for 10 min the mixture was extracted with EtOAc (2 \times 4.0 mL). The combined organic layers were washed with water (2.0 mL) and brine (2.0 mL), dried over Na₂SO₄, concentrated under reduced pressure and the residue was dried in high vacuum to constant mass to yield the crude deprotected intermediate as a white amorphous solid.

Coupling: In an oven-dried, nitrogen-purged 10 mL Schlenk tube, equipped with a Teflon[®]-coated magnetic stirring bar, Boc-Val-OH (33 mg, 0.15 mmol, 1.2 eq) and Hünig's base (22 μ L, 0.13 mmol, 1.0 eq) were dissolved in absolute DMF (0.35 mL), stirred and cooled to 0 °C in an ice bath. A solution of HATU (57 mg, 0.15 mmol, 1.2 eq) in abs. DMF (0.35 mL) was added and the reaction solution was stirred for 1 min before a solution of the deprotected intermediate and Hünig's base (22 μ L, 0.13 mmol, 1.0 eq) in abs. DMF (0.60 mL) was added. After TLC indicated full conversion of the intermediate (30 min), the reaction was quenched by addition of brine (1.3 mL) and extracted with EtOAc (3 \times 3.0 mL). The combined organic extracts were washed with brine (3 \times 1.5 mL), dried over Na₂SO₄, and concentrated under reduced pressure. Purification via flash chromatography (SiO₂, CH₂Cl₂/MeOH 50:1 to 20:1) furnished **14** (20 mg, 0.026 mmol) as a white solid.

Yield: 20 mg (0.026 mmol, 21%, 2 steps, from **13**), white solid.

m.p. = 87–89 °C.

$[\alpha]_D^{23} = -26.6^\circ$ (c = 0.52, CHCl₃).

R_f = 0.20 (CH₂Cl₂/MeOH 20:1 (v/v); staining: KMnO₄).

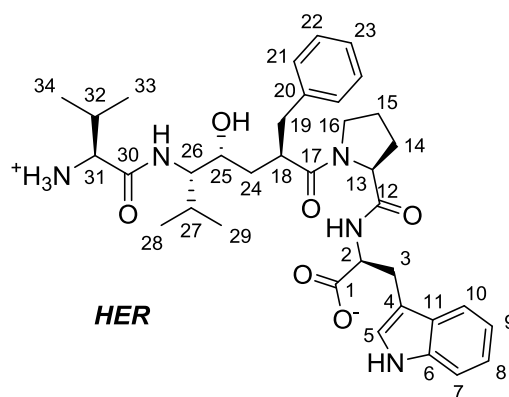
¹H NMR (300 MHz, CDCl₃, complex mixture of signals of 2 rotamers in 7:1 ratio; major rotamer assigned based on COSY, HSQC, and EXSY) δ = 9.02 (br s, 1H, indole NH), 7.50 (d, ³J = 7.6 Hz, 1H, H–C10), 7.42–6.89 (m, 10H, H–Ar and amide NH from Trp), 6.13 (d, ³J = 9.2 Hz, 1H, amide NH), 5.04 (d, ³J = 8.9 Hz, 1H, carbamate NH), 4.81–4.58 (m, 1H, H–C2), 3.93–3.87 (m, 1H, H–C31), 3.83–3.52 (m, 4H, CH₃O and H–C26), 3.50–3.15 (m, 3H, H₂–C3 and H–C13), 3.14–2.96 (m, 1H, H_a–C16), 2.91–2.73 (m, 1H, H_b–C16), 2.71–2.55 (m, 2H, H₂–C19), 2.55–2.40 (m, 1H, H–C18), 2.36–1.50 (m, 5H, H–C32, H–C27, H₂–C24, H_a–C14), 1.50–1.38 (m, 9H, (CH₃)₃C), 1.37–1.18 (m, 1H, H_a–C15), 1.12–0.75 (m, 14H, H₃–C33, H₃–C34, H_b–C14, H_b–C15, H₃–C28 and H₃–C29).

¹³C NMR (75 MHz, CDCl₃, complex mixture of signals of 2 rotamers in 7:1 ratio; major rotamer assigned based on COSY, HSQC, and EXSY) δ = 175.4 (s, 1C, C17), 172.8 (s, 1C, C=O), 172.7 (s, 1C, C=O), 172.3 (s, 1C, C=O), 156.2 (s, 1C, carbamate C=O), 138.8 (s, 1C, C20), 136.3 (s, 1C, C6), 129.2 (s, 2C, C22), 128.5 (s, 2C, C21), 127.6 (s, 1C, C11), 126.8 (s, 1C, C23), 123.4 (s, 1C, C5), 122.3 (s, 1C, C8), 119.9 (s, 1C, C9), 118.0 (s, 1C, C10), 111.8 (s, 1C, C7), 109.9 (s, 1C, C4), 80.4 (s, 1C, Me₃C), 71.0 (s, 1C, C25), 60.8 (s, 1C, C31), 60.1 (s, 1C, C13), 59.3 (s, 1C, C26), 53.6 (s, 1C, C2), 52.6 (s, 1C, CH₃O), 46.2 (s, 1C, C16), 44.0 (s, 1C, C18), 39.9 (s, 1C, C19), 37.1 (s, 1C, C24), 31.0 (s, 1C, C14), 30.0 (s, 1C, C32), 28.5 (s, 3C, (CH₃)₃CO), 27.5 (s, 1C, C27), 26.2 (s, 1C, C3), 21.8 (s, 1C, C15), 20.6 (s, 1C, C28), 19.9 (s, 1C, C33), 18.2 (s, 1C, C34) and 16.8 (s, 1C, C29).

HPLC-ESI-MS (Agilent Poroshell120; method: fast_Poroshell120_001HCOOHMeCN): *t*_R(**14**) = 9.14 min, 100%, [M + Na]⁺ = 785, [M + K]⁺ = 801.

HRMS (ESI): m/z (%): 784.4245 (100%, [M + Na]⁺, calcd for C₄₂H₅₉N₅NaO₈⁺: 784.4256).

(2S)-2-[[[(2S)-1-[(2R,4R,5S)-5-[(2S)-2-Azaniumyl-3-methylbutanamido]-2-benzyl-4-hydroxy-6-methylheptanoyl]pyrrolidin-2-yl]formamido]-3-(1H-indol-3-yl)propanoate
(15)



15

Saponification: In a 5 mL glass vial equipped with a Teflon[®]-coated magnetic stirring bar, **14** (11 mg, 0.015 mmol, 1.0 eq) was dissolved in THF (0.20 mL). A solution of LiOH×H₂O (5 mg, 0.12 mmol, 8.0 eq) in H₂O (0.10 mL) was added and the mixture was stirred vigorously until TLC indicated full conversion (60 min). The acidity of the solution was adjusted to pH=3 with 1M HCl. The resulting white colloidal mixture was extracted with EtOAc (3×1 mL). The combined organic extracts were merged, dried over Na₂SO₄, concentrated under reduced pressure and dried in high vacuum to constant mass to yield a saponified intermediate as an off-white powder (5 mg).

Boc-deprotection: In a 5 mL glass vial equipped with a Teflon[®]-coated magnetic stirring bar, the saponified intermediate (40 mg) was dissolved in trifluoroacetic acid (150 μL) and stirred for 5 min. The mixture was concentrated under reduced pressure and dried under high vacuum to constant mass. The residue was dissolved in water (600 μL), MeCN (200 μL) and DMSO (300 μL) and purified via preparative reverse phase HPLC (method: JKV_NucleodurC18_001HCOOH_10to85) to yield **15** (4.0 mg, 0.0062 mmol, 41%, 2 steps) as a white solid.

Yield: 4.0 mg (0.0062 mmol, 41%, 2 steps, from **14**), white solid.

m.p. = 123–126 °C.

$[\alpha]_D^{23} = -25^\circ$ ($c = 0.13$, MeOH).

^1H NMR (500 MHz, methanol- d_4 , complex mixture of signals of 2 Pro-peptide rotamers in equilibrium, major rotamer assigned based on COSY and HSQC) $\delta = 8.53$ (br s, 1H, indole NH), 7.73–6.88 (m, 10H, H–Ar), 4.66–4.56 (m, 1H, H–C2), 3.85–3.78 (m, 2H, H–C25 and H–C26), 3.70 (d, 1H, $^3J = 4.9$ Hz, H–C31), 3.52–3.36 (m, 2H, H–C13 and H_a–C3), 3.25–3.12 (m, 1H, H_b–C3), 3.11–3.01 (m, 1H, H_a–C16), 2.94–2.82 (m, 1H, H_b–C16), 2.81–2.70 (m, 2H, H–C18 and H_a–C19), 2.69–2.59 (m, 1H, H_b–C19), 2.35–2.10 (m, 2H, H–C32 and H–C27), 2.08–1.94 (m, 1H, H_a–C24), 1.68–1.58 (m, 1H, H_b–C24), 1.53–1.42 (m, 1H, H_a–C14), 1.24–0.68 (m, 15H, H_b–C14, H₂–C15, H₃–C33, H₃–C34, H₃–C28 and H₃–C29).

^{13}C NMR (125 MHz, methanol- d_4 , complex mixture of signals of 2 Pro-peptide rotamers in equilibrium, major rotamer assigned based on COSY and HSQC) $\delta = 177.8$ (C=O), 173.1 (s, 1C, C=O), 170.7 (s, 1C, C=O), 169.6 (s, 1C, C=O), 140.3 (s, 1C, C20), 138.0 (s, 1C, C6), 130.1 (s, 2C, C22), 129.6 (s, 2C, C21), 127.9–127.2 (m, 2C, C23 and C11), 124.2 (s, 1C, C5), 122.3 (s, 1C, C8), 119.7 (s, 1C, C9), 119.5 (s, 1C, C10), 112.2 (s, 1C, C4), 112.1 (s, 1C, C7), 71.1 (s, 1C, C25), 62.3 (s, 1C, C13), 61.4 (s, 1C, C26), 60.5 (s, 1C, C31), 57.0 (s, 1C, C2), 47.3 (s, 1C, C16), 45.4 (s, 1C, C18), 40.5 (s, 1C, C19), 37.5 (s, 1C, C24), 31.9 (s, 1C, C32), 31.7 (s, 1C, C14), 29.3 (s, 1C, C27), 28.5 (s, 1C, C3), 22.4 (s, 1C, C15), 21.1 (s, 1C, C28), 19.6 (s, 1C, C33), 18.4 (s, 1C, C29) and 17.5 (s, 1C, C34).

HPLC-ESI-MS (Agilent Poroshell120; method: fast_Poroshell_001HCOOH_8mingradient.lc): $t_R(\mathbf{15}) = 6.56$ min, 100%, $[\text{M} + 1]^+ = 648$, $[\text{M} + \text{Na}]^+ = 670$.

HRMS (ESI): m/z (%): 648.3752 (100%, $[\text{M} + 1]^+$, calcd for $\text{C}_{36}\text{H}_{50}\text{N}_5\text{O}_6^+$: 648.3756), 1295.7433 (91%, $[\text{2M} + 1]^+$, calcd for $\text{C}_{72}\text{H}_{99}\text{N}_{10}\text{O}_{12}^+$: 1295.7438).

Protein expression and purification.

The active wildtype (WT) and inactive E451A variant of hDPP3(1–726) used in this study were cloned and inserted into pET21a and pET28a respectively. Thereafter, the plasmids containing the desired constructs were transformed into a BL21-CodonPlus (DE3) RIL strain. The cell culture was grown in Luria-Bertani (LB) medium containing $100 \mu\text{g ml}^{-1}$ Ampicillin for WT-DPP3 and $50 \mu\text{g ml}^{-1}$ kanamycin for inactive DPP3-E451A. Gene expression was

induced with 0.4 mM isopropyl-1-thio-D-galactopyranoside (IPTG) after the culture medium reached an OD of 0.6–0.8. After being allowed to grow overnight at 18 °C, the cells were harvested by centrifugation at 4000 g for 10 min. The harvested cell pellet was resuspended in 50 mM Tris-HCl pH 8.0 containing 150 mM NaCl, 10 mM imidazole (lysis buffer) and lysed by sonication. Centrifugation at 18000 g for 1 hour at 4 °C was performed to remove cell debris and the supernatant was subjected to affinity chromatography on Ni-NTA resin (5 mL prepacked His-trap FF, GE Healthcare) previously equilibrated with lysis buffer. Then the column was washed with lysis buffer supplemented with 20 mM imidazole. After washing, bound protein was eluted using lysis buffer containing 500 mM imidazole. Fractions containing target protein were pooled and concentrated with centrifugal filter units (Amicon Ultra-15, 50 kDa; Millipore, Massachusetts, USA). Concentrated protein was re-buffered to 50 mM Tris, 100 mM NaCl, pH 8.2 with a PD-10 desalting column. The protein solutions were shock frozen and stored at –80 °C if not used immediately.

The pure fractions were collected and pooled. This sample was then applied to a Superdex 200 16/60 gel filtration column (GE Healthcare) and pure fractions corresponding to a molecular mass of ~82 kDa were collected and concentrated. The buffer used for gel filtration was 100 mM multi component buffer (L-malic acid, MES and Tris, pH 8.0) containing 100 mM NaCl and 1 mM tris (2-carboxyethyl) phosphine (TCEP). The purity of the fractions was analyzed by 12.5% SDS-PAGE.

Enzyme inhibition assay

The enzyme activity of hDPP3 was determined by following the release of 2-naphthylamine in a plate reader (excitation at 332 and emission at 420 nm) at 37 °C in a mixture containing 25 µl of 200 µM Arg-Arg-2-naphthylamide as substrate in 50 mM Tris-HCl buffer, pH 8.0 and 0.05-0.1 µM of enzyme in a total reaction mixture of 235 µl (White, Tissue Culture treated Krystal 2000 96-well plate from Porvair sciences, Norfolk, UK). The activity assay was performed by continuous measurement of fluorescence of 2-naphthylamide for 30 min (Molecular Devices, Sunnyvale CA, USA). For the inhibition assay, the inhibitors were added to the mixture without the substrate and incubated for 10 min at room temperature. The reaction was started by the addition of the substrate. The concentration of an inhibitor that gave 50% inhibition (IC₅₀) was determined through a series of assays with a fixed substrate concentration but with various inhibitor concentrations. 5% DMSO was used in the control

assay. The activity (in %) in the presence of increasing concentrations of the inhibitor was calculated using the equation:

$$\% \text{ activity} = 100 \times (\Delta\text{fluorescence} / \Delta\text{fluorescence of control})$$

The activity (in %) against concentration of inhibitor (log scale for inhibitor concentration [x-axis] and linear scale for percent activity [y-axis]) was plotted. The activity in % vs. log of concentration was fitted to a sigmoidal dose-response curve using the four parameter logistic equation entitled “log (inhibitor) vs. response -- variable slope” in GraphPad Prism (San Diego, CA, USA).

To measure *ex vivo* inhibition, *dpp3*-knockout mice (DPP3^{-/-}) bred and maintained in the animal facility of the University of Graz were used. The brains from ~ 16-week old male DPP3^{-/-} mice were surgically removed and washed with PBS. Homogenization was performed on ice in solution A (0.25M sucrose, 1 mM EDTA, 20 μM dithiothreitol, 0.1% Triton X-100, 20 μg/ml leupeptin, 2 μg/ml antipain, 1 μg/ml pepstatin, pH 7.0) using an Ultra Turrax (IKA, Staufen, Germany). 20000 g infranatants were used for further experiments. Protein concentrations in the tissue lysates were estimated using the Protein Assay Dye Reagent (Bio-Rad, Munich, Germany) using bovine serum albumin as the standard. 0.01-0.05 mg/ml of tissue homogenate was used in the same assay as described above.

Isothermal titration calorimetry

The inactive variant E451A of hDPP3 was used for thermodynamic analysis. The titrations were performed in 50 mM Tris-HCl pH 8 containing 100 mM NaCl and 5% DMSO. Both the purified enzyme and ligands were dissolved in exactly the same buffer, and all solutions were degassed immediately before the measurements. The measurements were performed with a VP-ITC microcalorimeter (MicroCal, Northampton, MA, USA). In each experiment the temperature was equilibrated at 298 K. The ligand solution in the syringe (500 μM) was titrated into a 20 μM solution of hDPP3 in the sample cell. In a typical experiment, under constant stirring at 270 rpm, a total of one aliquot of 2 μl and 29 aliquots of 10 μl of the ligand solution were injected at a rate of 0.5 μl/s into 1.421 ml of the enzyme solution. Every injection was carried out over a period of 20 s with a spacing of 300 s between the injections. The heat of binding was determined by integration of the observed peaks. The observed enthalpies were plotted against the ratio of peptide vs. protein concentration in the cell to generate the binding isotherm. Nonlinear least-squares fitting using Origin® version 7.0

(MicroCal®) was used to obtain association constants (K_a), the enthalpy (ΔH) and stoichiometries. The dissociation constants (K_d) were calculated using $K_d = 1/K_a$.

Time-dependent inhibition of hDPP3 by tynorphin and HER

Tynorphin (VVYPW), which is an endogenous pentapeptide inhibitor of hDPP3, was shown to be unstable in human serum and was cleaved rapidly to smaller fragments (3). Being a peptidase, it is likely that hDPP3 degrades tynorphin over time. A comparative study of tynorphin and *R*-hydroxyethylene was performed to study their behavior in a time-based manner and to assess their efficiency to inhibit hDPP3 as a function of time. For the assay, 0.1 μM of the enzyme was incubated at room temperature with inhibitor concentrations equivalent to 5 times their IC_{50} values. Enzyme in the absence of any inhibitor incubated at room temperature was used as control. At various time points (0, 0.25, 0.50, 0.15, 1, 2, 3, 4, 5, 20 and 24 hours), 10 μl aliquots were added to 200 μl of 50 mM Tris-HCl buffer, pH 8.0. The reaction was initiated by adding 25 μl of 200 μM Arg-Arg-2-naphthylamide and enzyme activity was measured fluorometrically (excitation, 332 nm; emission, 420 nm). The efficacy of inhibition was calculated as percent of control at each time point for tynorphin and HER.

Thermal shift assay with HER

Thermal shift assay was performed as described previously by (15). For this, a mixture of 10 μM hDPP3 and 50 μM HER was used. A separate mixture with the same concentrations of protein and inhibitor was incubated for 24 hours. A 20 μl aliquot from the pre-incubation solutions were mixed with 2 μl of 1:500 dilution of SYPRO® orange dye (Molecular Probes, Oregon, USA) and added to a white 96-well RT-PCR plate (Bio-Rad, California, USA). Protein incubated in the absence of inhibitor was used as a control sample. The plate was sealed with an Optical-Quality Sealing Tape (Bio-Rad, California, USA). The experiment was started by heating the plate from 20 °C to 95 °C in increments of 0.5 °C/s in a CFX Connect™ Real Time PCR detection system (Bio-Rad, California, USA). Fluorescence changes in the wells of the plate were monitored simultaneously at excitation and emission wavelengths of 470 and 500 nm, respectively. Melting temperatures (T_m) were determined using CFX manager 3.0 software (Bio-Rad, California, USA).

Acknowledgements

This work was supported by a grant from the Austrian Science Foundation (FWF) through grants W901 (Doctoral Program “Molecular Enzymology”) to PM and RB. The authors are also grateful for the support by the interuniversity program in natural sciences (NAWI Graz).

References

1. Prajapati SC, Chauhan SS. Dipeptidyl peptidase III: a multifaceted oligopeptide N-end cutter. *FEBS J.* 2011 Sep;278(18):3256-76.
2. Bezerra GA, Dobrovetsky E, Viertlmayr R, Dong A, Binter A, Abramić M, et al. Entropy-driven binding of opioid peptides induces a large domain motion in human dipeptidyl peptidase III. *PNAS.* 2012 -04-24 00:00:00;109(17):6525-30.
3. Yamamoto Y, Hashimoto J, Shimamura M, Yamaguchi T, Hazato T. Characterization of tynorphin, a potent endogenous inhibitor of dipeptidyl peptidase III. *Peptides.* 2000 Apr;21(4):503-8.
4. Chiba T, Li Y, Yamane T, Ogikubo O, Fukuoka M, Arai R, et al. Inhibition of recombinant dipeptidyl peptidase III by synthetic hemorphin-like peptides. *Peptides.* 2003 May;24(5):773-8.
5. Thanawala V, Kadam VJ, Ghosh R. Enkephalinase inhibitors: potential agents for the management of pain. *Curr Drug Targets.* 2008 Oct;9(10):887-94.
6. Akiyama T, Nakamura KT, Takahashi Y, Naganawa H, Muraoka Y, Aoyagi T, et al. Fluostatins A and B, new inhibitors of dipeptidyl peptidase III, produced by *Streptomyces* sp. TA-3391. II. Structure determination. *J Antibiot.* 1998 Jun;51(6):586-8.
7. Agić D, Hranjec M, Jajcanin N, Starcević K, Karminski-Zamola G, Abramić M. Novel amidino-substituted benzimidazoles: synthesis of compounds and inhibition of dipeptidyl peptidase III. *Bioorg Chem.* 2007 Apr;35(2):153-69.
8. Hom RK, Gailunas AF, Mamo S, Fang LY, Tung JS, Walker DE, et al. Design and synthesis of hydroxyethylene-based peptidomimetic inhibitors of human beta-secretase. *J Med Chem.* 2004 Jan 01;47(1):158-64.
9. Petroková H, Dusková J, Dohnálek J, Skálová T, Vondrácková-Buchtelová E, Soucek M, et al. Role of hydroxyl group and R/S configuration of isostere in binding properties of HIV-1 protease inhibitors. *Eur J Biochem.* 2004 Nov;271(22):4451-61.
10. Tossi A, Benedetti F, Norbedo S, Skrbec D, Berti F, Romeo D. Small hydroxyethylene-based peptidomimetics inhibiting both HIV-1 and *C. albicans* aspartic proteases. *Bioorg Med Chem.* 2003 Nov 03;11(22):4719-27.
11. Vandenbroucke RE, Libert C. Is there new hope for therapeutic matrix metalloproteinase inhibition? *Nat Rev Drug Discov.* 2014 Dec;13(12):904-27.
12. Fehrentz JA, Heitz A, Castro B, Cazaubon C, Nisato D. Aldehydic peptides inhibiting renin. *FEBS Lett.* 1984 Feb 27;167(2):273-6.
13. Ghosh AK, Xi K, Ratia K, Santarsiero BD, Fu W, Harcourt BH, et al. Design and synthesis of peptidomimetic severe acute respiratory syndrome chymotrypsin-like protease inhibitors. *J Med Chem.* 2005 Nov 03;48(22):6767-71.

14. Wollinsky B, Ludwig L, Hamacher A, Yu X, Kassack MU, Li S. Prenylation at the indole ring leads to a significant increase of cytotoxicity of tryptophan-containing cyclic dipeptides. *Bioorg Med Chem Lett.* 2012 Jun 15;22(12):3866-9.

15. Ericsson UB, Hallberg BM, Detitta GT, Dekker N, Nordlund P. Thermofluor-based high-throughput stability optimization of proteins for structural studies. *Anal Biochem.* 2006 Oct 15;357(2):289-98.

Chapter 4

Novel methods for the quantification of Dipeptidyl Peptidase 3 (DPP3) concentration and activity in human blood samples

**Novel methods for the quantification of Dipeptidyl Peptidase 3 (DPP3) concentration
and activity in human blood samples**

**Linda Rehfeld¹, Eugenia Funk¹, Shaline Jha², Peter Macheroux², Olle Melander³,
Andreas Bergmann¹**

¹Sphingotec Therapeutics GmbH, Hennigsdorf, Germany

²Graz University of Technology, Institute of Biochemistry, 8010 Graz, Austria

³Lund University, Department of Clinical Sciences, Clinical Research Center, Malmö,
Sweden

Author contributions

L.R. initiated the project; L.R., E.F., S.J., P.M., O.M., and A.B. designed research; L.R., E.F., S.J., O.M., and A.B. performed research; L.R., E.F., O.M., and A.B. analyzed data and interpreted experimental results; L.R., S.J., and P.M. wrote the manuscript.

Keywords: Dipeptidyl peptidase 3, angiotensin II, luminescence immunoassay, enzyme capture activity assay

Abbreviations:

aa: amino acid, Arg2- β NA: Arg-Arg- β -naphthylamide, β NA: β -naphthylamine, BSA: bovine serum albumin, CV: coefficient of variation, DPP3: dipeptidyl peptidase 3, ECA: enzyme capture activity assay, GST: glutathione-S-transferase, hDPP3: human DPP3, His: 6xhistidine-tag, HPLC: high pressure liquid chromatography, kDa: kilodalton, LIA: luminometric immunoassay, LOD: limit of detection, LOQ: limit of quantification, mAb: monoclonal antibody, MACN: MA70-Acrinium-NHS-Ester, RFU: relative fluorescence units, RLU: relative light units, SD: standard deviation

Abstract

Background: The ubiquitously expressed dipeptidyl peptidase 3 (DPP3) is involved in protein metabolism, blood pressure regulation and pain modulation. These diverse functions of DPP3 are attributed to the degradation of bioactive peptides like angiotensin II. However, due to limitations in currently available assays for determination of active DPP3 in plasma, the exact physiological function of DPP3 and its role in the catabolism of bioactive peptides is understudied. Here, we developed two assays to specifically detect and quantify DPP3 protein and activity in plasma, and validated DPP3 quantification in samples from critically ill patients.

Methods: Assay performance was evaluated in a sandwich-type luminometric immunoassay (LIA) and an enzyme capture activity assay (ECA). DPP3 plasma levels were detected in a healthy, population-based, cohort and in critically ill patients suffering from severe sepsis and septic shock.

Results: The DPP3-LIA and -ECA show an almost ideal correlation and very similar and robust performance characteristics. DPP3 activity is detectable in plasma of predominantly healthy subjects with a mean (\pm SD) of 58.6 (\pm 20.5) U/L. Septic patients show significantly increased DPP3 plasma activity at hospital admission. DPP3 levels further increase in patients with more severe conditions and high mortality risk.

Conclusion: We developed two highly specific assays for the detection of DPP3 in plasma. These assays allow the use of DPP3 as a biomarker for the severity of acute clinical conditions and will be of great value for future investigations of DPP3's role in bioactive peptide degradation in general and the angiotensin II pathway in specific.

Impact Statement

The assay technologies described here, enable for the first time a highly specific measurement of DPP3 concentration and activity in plasma. As DPP3 cleaves bioactive peptides, i.e. angiotensin II, in the circulation, it can influence the renin-angiotensin pathway and thus be a key player in acute diseases. The two novel assays are powerful tools for research studies involving the bioactive peptide degradation and can potentially evolve as important tools for determining severity of patients' acute conditions and for monitoring of the treatment and decision making in a clinical setting.

Introduction

Human dipeptidyl peptidase 3 (DPP 3; EC 3.4.14.4), also known as red cell angiotensinase, is a member of the M49 family of zinc dependent metallopeptidases and cleaves dipeptides sequentially from the N-terminus of various bioactive peptide substrates(1). DPP3 was first identified and its activity measured by Ellis and Nuenke in 1967(2). The enzyme has a molecular mass of about 83 kDa, is ubiquitously expressed and highly conserved in prokaryotes and eukaryotes(1).

Although the protein is known for a long time and despite its widespread expression, the exact biological function of DPP3 is not understood. Recent findings indicate a role, not only in protein metabolism, but also in blood pressure regulation, pain modulation and inflammatory processes, based on the substrate specificity of DPP3(1).

DPP3 was detected in organ homogenates and several bodily fluids, such as retroplacental serum(3), seminal plasma(4) and cerebrospinal fluid(5). The release of intracellular DPP3 was proposed as a marker for dying cells in a cell culture system(6) and as influencing factor for the immune response in a mouse model by degrading potential antigens(7). *In vitro*, DPP3 has been shown to cleave peptides such as angiotensins, enkephalins and endomorphins(8,9). The most prominent substrate of DPP3 is angiotensin II (Ang II) – the main effector of the renin-angiotensin system (RAS). The RAS is activated in cardiovascular diseases (10–12), sepsis and septic shock(13). Ang II, in particular, has been shown to modulate many cardiovascular functions including the control of blood pressure and cardiac remodelling. Furthermore, infusion of Ang II improved 28d survival of septic patients in a phase 3 clinical trial(14). Pang et al. (2016) showed a direct interaction of DPP3 and Ang II *in vivo*, including an effect of DPP3 injection on blood pressure due to Ang II cleavage(15). Thus, quantification of plasma levels of active DPP3 could be a useful tool to further understand the RAS regulation in plasma.

The release of DPP3 from dying cells, and DPP3's implications in diseases and regulation of the RAS system, raised the question whether DPP3 can be detected and quantified in blood or plasma. The standard detection method for purified DPP3 is a soluble enzyme activity assay with fluorogenic substrates, e.g. Arg-Arg- β -naphthylamide (Arg₂- β NA)(2). However, this assay is not specifically detecting DPP3 activity, but also the activity of other aminopeptidases that cleave single amino acids off the fluorogenic substrate(16,17). Furthermore, other substances in the plasma samples can interfere with the assay itself or

show self-fluorescence. Especially the use of EDTA plasma in this soluble assay is not possible due to the chelating effect on the metalloprotease DPP3. All possible interferences make the so far used soluble activity assay unsuitable for the reproducible detection of DPP3 activity in plasma samples. Thus, the clinical significance of DPP3 in human plasma could not be analysed yet. Here, we generated, characterized and validated two assays to specifically detect DPP3 in human bodily fluids (e.g. blood, plasma, serum): A luminescence immunoassay (LIA) to detect DPP3 protein concentration and an enzyme capture activity assay (ECA) to detect specific DPP3 activity. A washing step in both methods removes all interfering substances before the actual detection of DPP3 protein or activity is performed. Both methods are highly specific and allow the reproducible detection of DPP3 in blood samples.

Results

We developed and validated two assays to specifically detect DPP3 protein and activity in human plasma: a luminescence immunoassay (LIA) and an enzyme capture activity assay (ECA). Both assay principles are shown in Figure 1a and 1b respectively.

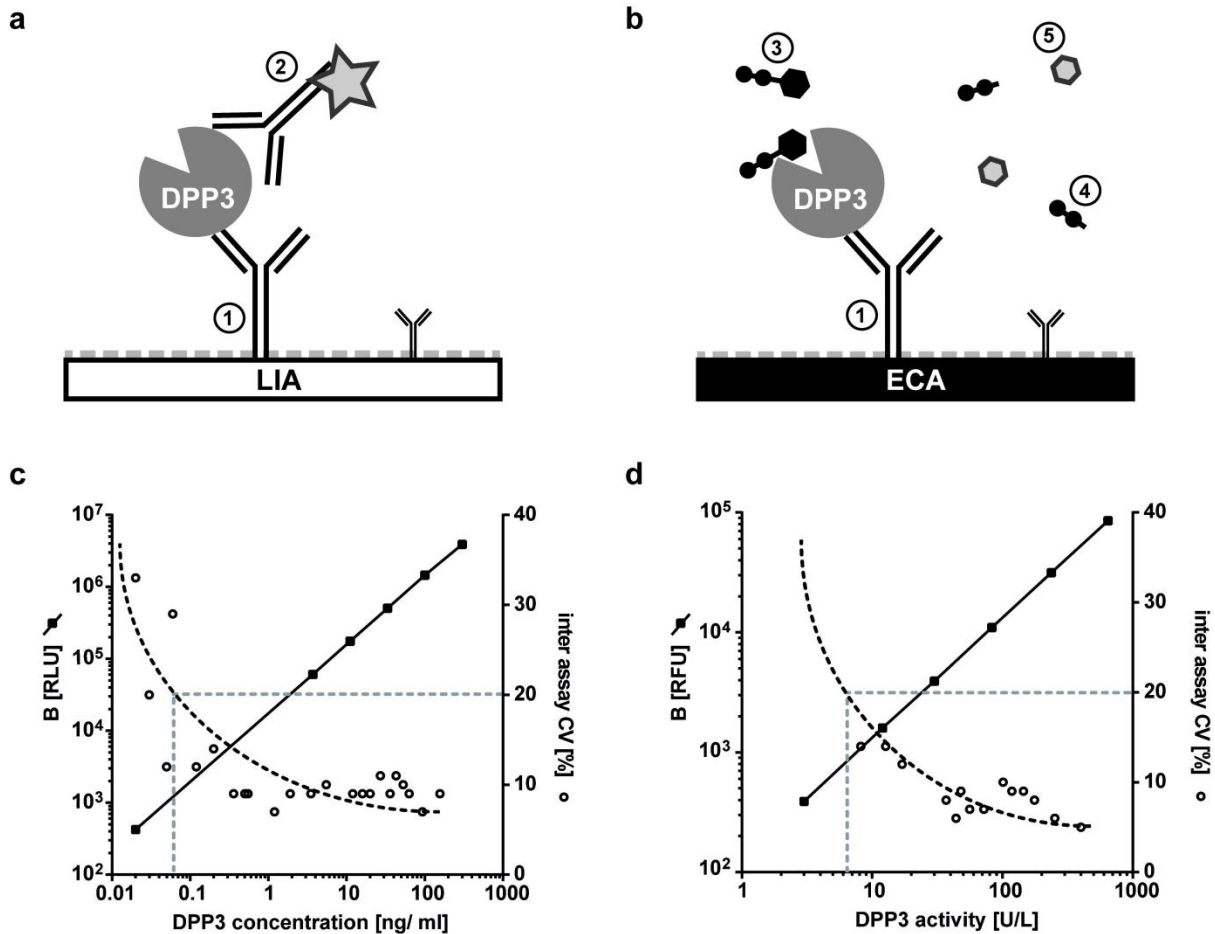


Figure 1: Schematic representation, range and precision of the two DPP3 assays. Plasma DPP3 concentration and activity is measured with the DPP3-LIA and ECA respectively. (a) Representation of the DPP3-LIA: a monoclonal antiDPP3 antibody (AK2555; ①) is used as the solid phase capture antibody coupled to white high-binding polystyrene plates; immobilized DPP3 is detected by the acridinium ester labelled, monoclonal antiDPP3 antibody AK2553 (②). (b) Representation of the DPP3-ECA: a monoclonal antiDPP3 antibody (AK2555; ①) is used as the solid phase capture antibody coupled to black high-binding polystyrene plates; specific activity of immobilized DPP3 is detected by addition of

the fluorogenic substrate Arg₂-βNA (③); DPP3 cleaves the substrate into the dipeptide Arg₂ (④) and fluorescent βNA (⑤; 410 nm); (c-d) Representative dose response curves and interassay precision profiles for the detection of DPP3 concentration (LIA, c) and DPP3 activity (ECA, d). Each point represents the mean of 10 measurements.

A typical dose-response-curve along with the obtained interassay precision profile of the DPP3-LIA is shown in Figure 1c. From the interassay precision profile the limit of quantification (LOQ) was 0.06 ng/mL and the limit of detection (LOD) of the assay was determined at 0.033 ng/mL. The quantitative measuring range of the assay was deduced to be 0.06-300 ng/mL.

Figure 1d shows a typical dose-response-curve along with the obtained interassay precision profile of the DPP3-ECA. From this the LOQ of the assay was 6.5 U/L and the LOD was determined at 3.5 U/L. The quantitative measuring range of the assay was deduced to be 6.5-645 U/L.

The characterization, performance and stability analyses of both assays are summarized in Table 1. The accuracy of both assays was determined by addition of known amounts of DPP3 from blood cells to plasma samples and analysis of the recovery from the expected value. The recovery fulfilled all quality criteria (average recovery from expected concentration of ±20%) in both assays. The linearity of the assays was assessed by two methods: a) by stepwise dilution of native plasma samples with zero matrix (heat-inactivated horse serum; X2, X4, X8, X16, X32) and b) by mixing various native plasma samples containing different concentrations of endogenous DPP3. Both, linear dilution and mixing of native samples fulfilled all quality criteria of linearity in both assays.

Upper limits of both assays were determined by using samples with increasing DPP3 concentrations. The DPP3-LIA reaches its saturation plateau above 400 ng/mL and a high dose hook effect starts at concentrations above 5 μg/mL. Due to the assay design there is no high dose hook effect possible in the DPP3-ECA, but the assay reaches a plateau of saturation and substrate limitation at 2,500 U/L.

The activity of DPP3 is strongly dependent on the pH of the surrounding buffer. Hence, a study was conducted specifically for the second step of the DPP3-ECA and the influence of pH changes on the specific DPP3 activity as determined by calibrators. The assay performance is unaffected by pH changes between 7.5 and 8.5.

Parameter	DPP3-LIA	DPP3-ECA
Calibrator Range	0.02 (def.) - 300 ng/mL	3 (def.) - 645 U/L
Limit of Detection	0.033 ng/mL	3.5 U/L
Limit of Quantitation	0.06 ng/mL	6.5 U/L
Upper limit	saturation plateau: >400 ng/mL high dose hook: >5.000 ng/mL	Substrate limitation plateau: >2.500 U/L; no high dose hook
Accuracy (Recovery of added DPP3 to EDTA plasma)	Average (range) % recovery from expected = 97% (87-108%)	Average (range) % recovery from expected = 99% (93 - 104%)
Linearity (10 mixing studies)	Range: 8.7-91.6 ng/mL Average (range) % recovery from expected = 101% (99-105%)	Range: 24.6-239.2 U/L Average (range) % recovery from expected = 101% (95-106%)
Dilutional Linearity (Dilutions: X2, X4, X8, X16, X32 using zero calibrator)	Range: 57.5-98.4 ng/mL Average (range) % recovery from expected = 100% (95-107%) for all dilutions	Range: 163.6-268.7 U/L Average (range) % recovery from expected = 100% (93-114%) until X16 dilution; unacceptable recovery of $\geq 120\%$ at X32
Analytical Specificity [Interfering substance (concentration maximum), % recovery MW \pm SD]	Triglycerides (3 g/L) = 90% \pm 4.7% Bilirubin (40 mg/dL) = 99% \pm 6.4% Albumin (6 g/dL) = 102% \pm 2.1% Hemoglobin (500 mg/dL) = 101% \pm 6.8% Heparin (3000 U/L) = 103% \pm 2.4%	Triglycerides (3 g/L) = 96% \pm 2.1% Bilirubin (40 mg/dL) = 99% \pm 2.7% Albumin (6 g/dL) = 102% \pm 3.3% Hemoglobin (500 mg/dL) = 101% \pm 4.4% Heparin (3000 U/L) = 102% \pm 3.2%
pH stability of activity (Average (\pm SD) % recovery of specific	not relevant	pH 7.5: 99% ($\pm 2.2\%$) pH 8.5: 96% ($\pm 1.7\%$)

DPP3 activity compared to reference (pH 8.0))		
<i>Ex vivo</i> stability at 22°C (Average (±SD) % recovery from fresh sample (t=0h))	2h: 98% (±2,0%)	2h: 101% (±3,7%)
	4h: 97% (±4,2%)	4h: 101% (±7,1%)
	8h: 96% (±4,9%)	8h: 100% (±2,8%)
	24h: 98% (±1,3%)	24h: 99% (±5,1%)
	48h: 97% (±4,6%)	48h: 100% (±5,1%)
	15d: 86% (±3,1%)	15d: 92% (±3,0%)
	15d (4°C): 101% (±2,5%)	15d (4°C): 102% (±3,2%)
Freeze thaw stability	Average (±SD) % recovery from fresh sample after up to 6 freeze thaw cycles: 104% (±6,8%)	Average (±SD) % recovery from fresh sample after up to 6 freeze thaw cycles: 104% (±6,8%)

Table 1: Analytical Performance Characteristics of the DPP3-LIA and the DPP3-ECA.

The *ex vivo* stability of DPP3 concentration and activity in five native EDTA plasma samples was determined. Upon storage at 22°C, recoveries were acceptable until at least 15 days in both DPP3 concentration and activity. Up to six freeze-thaw cycles did not alter recovery of DPP3 and DPP3 activity in native EDTA plasma samples.

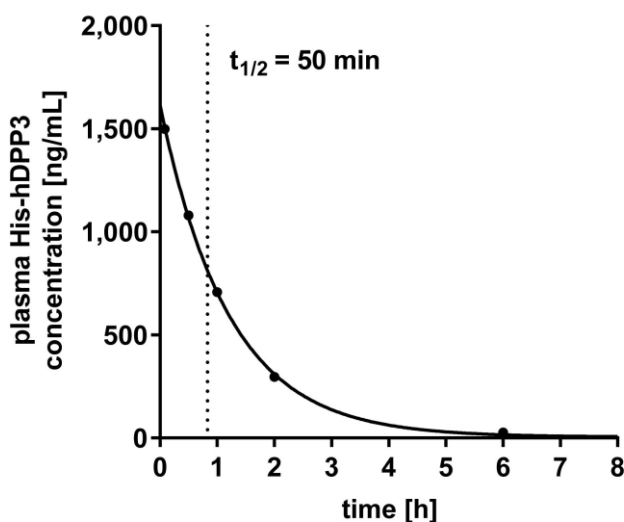


Figure 2: Plasma half-life of DPP3: Recombinant His-hDPP3 was injected into healthy rats (n=3) and plasma hDPP3 levels monitored using the DPP3-LIA.

In vivo stability analysis of DPP3 were performed to estimate the dynamics of DPP3 as a biomarker. Recombinant human His-hDPP3₍₁₋₇₂₆₎ and the vehicle PBS were injected into rats and hDPP3 levels measured using the DPP3-LIA. Since the LIA does not recognize rat DPP3, due to antibody specificity, there was no DPP3 signal in PBS treated rats. His-hDPP3 shows a calculated plasma half-life of 70 minutes (Fig. 2).

Since both assays showed similar performance and characteristics we first analysed their correlation. To assess the complete range of DPP3 levels in humans, samples from healthy subjects and from severely ill patients were measured. The scatter blot in Figure 3 shows an almost ideal correlation ($r=0.9873$, $p<0.0001$) of both assays. Since the results from both assays are completely interchangeable, we focused on the DPP3-ECA for the following clinical analyses.

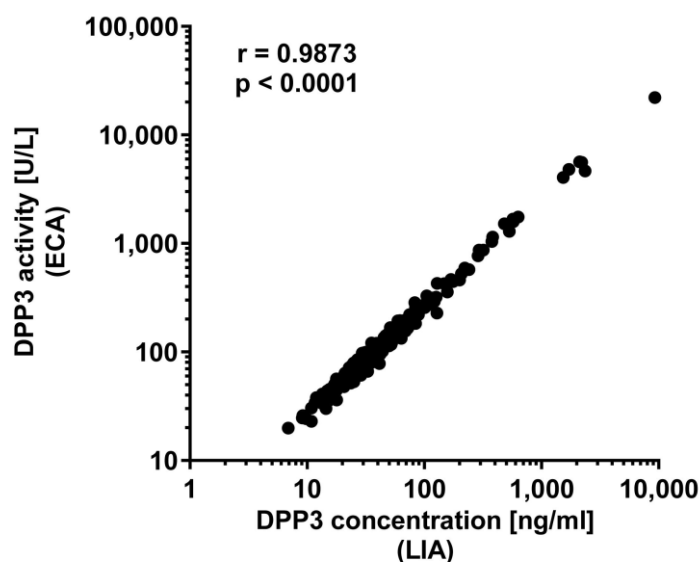


Figure 3: Correlation of DPP3-LIA and -ECA in human plasma samples: Scatter plot of the correlation of DPP3-LIA and DPP3-ECA in samples from critically ill patients and healthy controls.

We measured DPP3 activity in a random subcohort of the Malmö Preventive Project (MPP). For all samples, DPP3 activities were higher than the limit of detection of the assay. The distribution of the DPP3 activities in this healthy population-based cohort was used to calculate the normal range for DPP3 in plasma (Fig. 4a). The mean (\pm SD) was 58.6 (\pm 20.5) U/L. The 99th percentile of this cohort was 106.2 U/L.

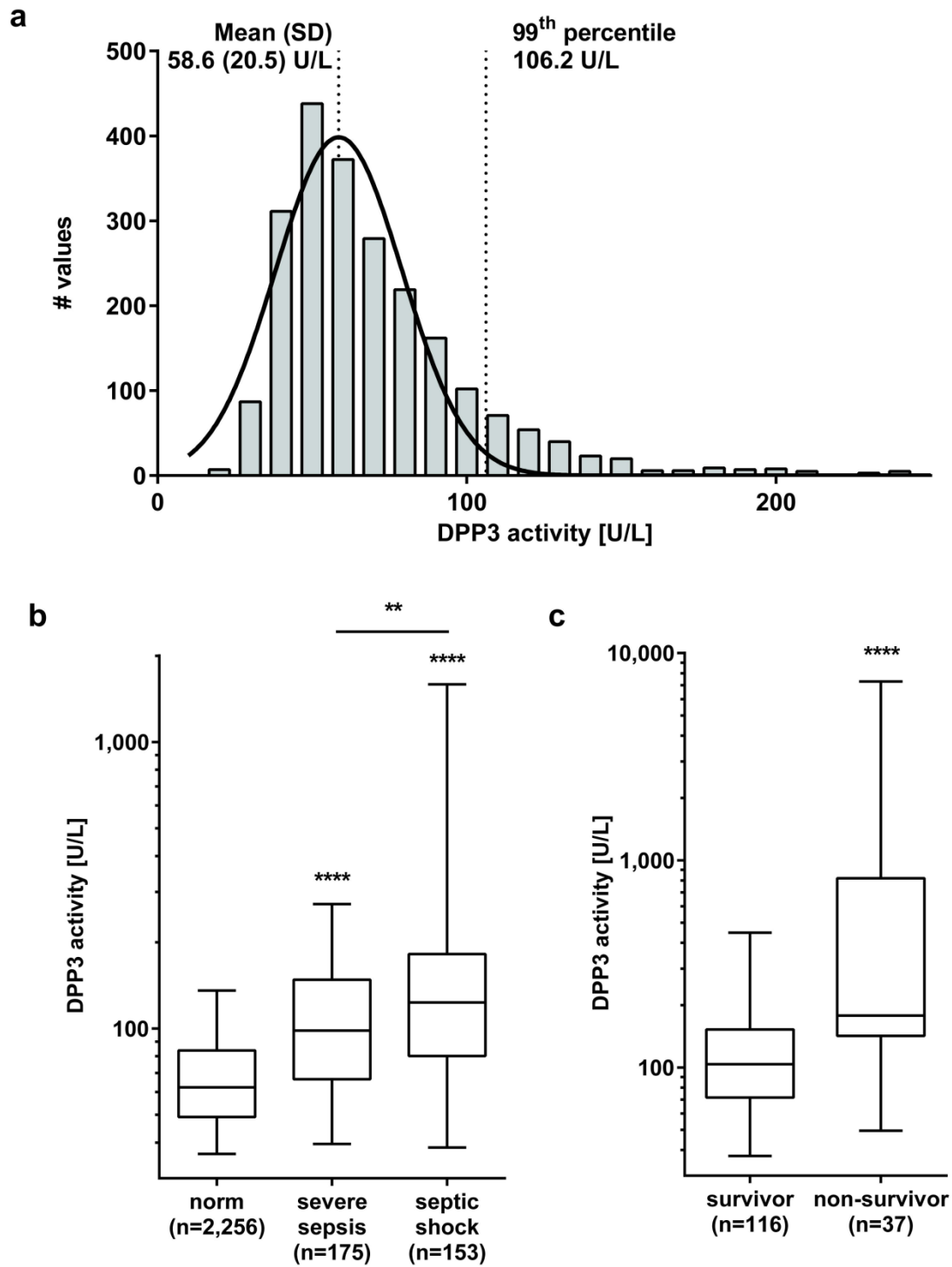


Figure 4: Plasma DPP3 levels in healthy and critically ill humans: (a) DPP3 activity (ECA) in a cohort of healthy subjects ($n=2,256$). The data did not pass the D'Angostino-Pearson omnibus test for normal distribution; a normal distribution curve was fitted into the frequency distribution of this cohort. (b-d) DPP3 plasma activity levels in a cohort of septic patients: (b) comparison of healthy subjects with patients suffering from severe sepsis and

*septic shock. (c) ROC curves DPP3 activities in severe sepsis and septic shock. (d) DPP3 plasma activity levels of septic shock patients that survived for at least 28 days vs. non-survivors. Box: median, 25 and 75 percentile; whiskers: 5 and 95 percentile. Statistical significance between groups was assessed with the Mann-Witney U-test. * $p < 0.05$, ** $p < 0.01$, *** $p < 0.001$, **** $p < 0.0001$.*

Finally, we measured DPP3 plasma activities in critically ill patients from hospital admission. Patients were grouped by diagnosis in severe sepsis (n=175) and septic shock (n=153). Both groups show significantly increased DPP3 levels compared to the healthy subjects of the MPP subcohort, with the septic shock group furthermore being significantly higher than the severe sepsis group (Fig. 4b). ROC curves were generated for both diagnoses (Fig. 4c), showing an area under the curve of 0.7235 for severe sepsis and 0.7927 for septic shock. A further subgroup analysis dividing the septic shock group into 28-day-survivors (n=116) and non-survivors (n=37) is shown in Figure 4d. DPP3 plasma activity is significantly increased in non-survivors. In summary, DPP3 plasma activities are significantly increased in septic patients and further increase with the severity and mortality risk of the condition.

Discussion

Our data document the accurate and reproducible performance of two different assay formats to specifically measure DPP3 plasma concentration and activity. We have demonstrated that DPP3 can be detected in the circulation and we defined a reference range for plasma DPP3 in healthy subjects.

DPP3 is a peptidase that cleaves dipeptides from the N-terminus of its substrates. Since most of its known substrates are found in circulation, it was our interest to determine specific DPP3 levels in plasma. Initially, we developed a classical one-step sandwich type immunoassay to detect DPP3 protein concentration in plasma (LIA), which can be easily transferred to other clinical platforms or point of care tests. Additionally, we aimed to measure the, physiologically more relevant, activity of the enzyme in circulation. To gain a high level of specificity we created an enzyme capture activity assay (ECA). The first step of this assay is the immobilization of DPP3 from plasma onto a solid phase, followed by a subsequent washing step. Finally, the activity of immobilized DPP3 is measured by the addition of a fluorogenic substrate. The assay design of the DPP3-ECA circumvents all limitations of the so far used soluble activity assay to detect DPP3 activity. The isolation of DPP3 before detection removes potential interfering substances, e.g. unspecific aminopeptidases, EDTA or fluorescent drugs. The DPP3-LIA and -ECA are both analytically robust and the performance is similar between the two formats. Surprisingly, the correlation of both assays is almost ideal. This indicates that every DPP3 protein detected by the LIA in plasma is active. The presence of active DPP3 in the circulation can lead to an uncontrolled degradation of bioactive peptide substrates, such as Ang II.

The DPP3-LIA or -ECA represent tools for specific DPP3 quantification and allow the further investigation of biological functions attributed to the DPP3 *in vivo*, e.g. a possible involvement in RAS pathway regulation due to Ang II cleavage. The developed assays can also address the specific mechanism of release and clearance of DPP3 from the circulation. Our pilot experiment in rats revealed a very short half-life of DPP3. This feature of DPP3 could make it a very useful dynamic biomarker in the monitoring of disease or treatment progression. Further clinical studies are required to monitor the changes in DPP3 plasma levels and assess its clinical relevance.

In this report, we show that DPP3 is a novel and valuable biomarker to indicate and possibly monitor the severity of patients' conditions, and that, with the DPP3-LIA and DPP3-ECA, we created two specific and powerful tools to quantify DPP3 in plasma.

Material and Methods

Antibodies

Monoclonal antibodies (mAb) directed against recombinant Glutathione-S-transferase tagged human DPP3 (GST-hPDP3; United States Biological, USA) were generated by standard procedures(18,19). In brief, Balb/c mice were immunized and boosted with recombinant GST-hDPP3; spleen cells were fused with SP2/0 myeloma cells to generate hybridoma cell lines. From this immunization we screened cell lines for their ability to secrete antibodies that bind DPP3. For the ECA, antibodies needed to be further screened for binding of DPP3 without inhibiting its activity. Inhibitory potential of screened antibodies was measured in a standard soluble activity assay with native DPP3 and fluorogenic substrate(20). With these approaches, we selected the hybridoma cell lines secreting monoclonal antibodies AK2553 and AK2555. Antibodies were produced by standard procedures and purified via protein A chromatography to obtain >95% purity as judged by capillary gel electrophoresis.

Recombinant human DPP3 production and purification

Recombinant DPP3 was produced as previously described(21). In Brief, the gene encoding human DPP3₍₁₋₇₂₆₎ was cloned into the pET21a expression vector, which includes a C-terminal hexahistidine tag (His-hDPP3). The plasmid was transformed into a BL21-CodonPlus (DE3) RIL strain and cells grown in Luria-Bertani medium containing 100 µg/mL ampicillin. Gene expression was induced with 0.4 mM isopropyl-1-thio-D-galactopyranoside (IPTG) at an OD of 0.6–0.8. The cells were then incubated overnight at 18 °C and harvested by centrifugation at 4,000 g for 10 min. The cell pellet was resuspended in lysis buffer (50 mM Tris-HCl, pH 8.0, 150 mM NaCl, 10 mM imidazole) and lysed by sonication. Centrifugation at 18,000 g for 1 hour at 4 °C was performed to remove cell debris and the supernatant was subjected to affinity chromatography on Ni-NTA resin (5 mL prepacked His-trap FF, GE Healthcare). Bound protein was eluted using lysis buffer containing 300 mM imidazole. The purity of the fractions was analyzed by 12.5% SDS-PAGE. Concentrated protein was re-buffered to 50 mM Tris, 100 mM NaCl, pH 8.2 with a PD-10 desalting column and endotoxins removed using Pierce™ High Capacity Endotoxin Removal Spin Columns.

Calibrators

Both assays were calibrated using dilutions of native DPP3 from human blood cell lysates. To prepare native DPP3, EDTA blood was centrifuged at 2,000 rpm and EDTA-plasma removed.

The blood cells were lysed by repeated freeze-thaw-cycles and cell debris was removed by centrifugation at 20,000 rpm. Supernatant with a DPP3 concentration of 10 µg/mL was used as stock solution for calibrator production. DPP3 concentration in the blood cell lysate was determined by DPP3-LIA using calibrators with purified recombinant His-hDPP3; DPP3 activity (U/L) of the blood cell lysate and the calibrators was determined by quantifying relative fluorescence units (RFU) of calibrator activity after 1h at 37°C with a dilution series of the fluorescent cleavage product β-naphthylamine (βNA, Sigma-Aldrich Chemie GmbH, Germany) in the range of 0.05-100 µM. All calibrators were diluted in heat-inactivated horse serum (Gibco® Thermofisher Scientific, Boston, USA) with 0,09% sodium azide.

Luminescence Immunoassay for the quantification of DPP3 protein levels (DPP3-LIA)

The DPP3-LIA is a one-step chemiluminescence sandwich immunoassay which uses polystyrene microtiter plates as solid phase.

Labeled Compound (Tracer)

Purified anti-DPP3 mAb AK2553 was labeled by incubation with a 1:5 molar ratio of MA70-Acrinium-NHS-Ester (MACN 1 g/L; Invent diagnostic GmbH, Hennigsdorf, Germany) for 30 minutes at room temperature. The reaction was stopped by addition of a 1:10 volume of 1M TRIS solution and the labeled antibody was separated from free label by gel filtration (Nap25 column, emp BIOTECH GmbH, Berlin, Germany) and further purified via size-exclusion chromatography on an HPLC column (Knauer, Berlin, Germany, 0.5 mL/min. flow rate). The tracer was produced by diluting labeled antibody in assay buffer (17 mM monopotassium phosphate, 83 mM dipotassium phosphate, 100 mM sodium chloride, 0.5% bovine serum albumin, 0.1% unspecific bovine IgG, 0.02% unspecific mouse IgG, 0.09% sodium azide, pH 7.4) to achieve an antibody concentration of 20 ng per well.

Solid phase

White high-binding polystyrene microtiter plates (Greiner Bio-One International AG, Austria) were coated (18 h at 2-4°C) with monoclonal anti-DPP3 antibody AK2555 (per well: 1.5 µg in 0.2 mL 50 mM Tris/HCl, 100 mM sodium chloride, pH 7.8). After blocking with 3% Karion FP, 0.5% BSA, 6.5 mM monopotassium phosphate, 3.5 mM disodium phosphate (pH 6.7), the plates were vacuum dried.

Assay protocol

20 μ L of samples or calibrators were pipetted into coated white microtiter plates. After adding labelled anti-DPP3 mAb AK2553, the microtiter plates were incubated for 3 hours at room temperature and 600 rpm (Titramax 101, Heidolph Instruments GmbH & CO. KG). Unbound tracer was removed by washing 4 times (350 μ L per well). Remaining chemiluminescence was measured for 1s per well by using the Centro LB 960 microtiter plate luminometer (Berthold Technologies GmbH & Co. KG, Germany). The concentration of DPP3 was determined using a 6-point calibration curve (0 (def. 0.02) - 300 ng/mL). Calibrators as well as samples were run in duplicate.

Enzyme capture activity assay for the quantification of DPP3 activity (DPP3-ECA)

The DPP3-ECA is a DPP3 specific activity assay which uses polystyrene microtiter plates as solid phase. DPP3 is immobilized by binding to a monoclonal antiDPP3 capture antibody, washed, and specific activity of immobilized DPP3 measured by the addition of a fluorogenic substrate.

Solid phase

Black high-binding polystyrene microtiter plates (Greiner Bio-One) were coated (18 h at 2-4°C) with monoclonal anti-DPP3 antibody AK2555 (per well: 1.5 μ g in 0.2 mL 50 mM Tris/HCl, 100 mM sodium chloride, pH 7.8). After blocking with 3% Karion FP, 0.5% BSA, 6.5 mM monopotassium phosphate, 3.5 mM disodium phosphate (pH 6.7), the plates were vacuum dried.

Assay protocol

Samples/calibrators (20 μ L) were pipetted into coated black microtiter plates. After adding assay buffer (200 μ L), the microtiter plates were incubated for 2 hours at 22°C and 600 rpm (Titramax 101, Heidolph Instruments). Unbound plasma components were removed by washing 4 times (350 μ L per well). The activity of immobilized DPP3 was then measured by using fluorogenic substrate(20). Microtiter plates were washed, reaction buffer (containing fluorogenic substrate Arg-Arg- β -naphthylamide (Arg₂- β NA, Bachem AG, Switzerland)) added and incubated at 37°C for 1 h. DPP3 specifically cleaves Arg₂- β NA into the Arg-Arg dipeptide and fluorescent β -naphthylamine (β NA; excitation at 340 nm, emission detected at 410 nm). Fluorescence was measured using the fluorometer Twinkle LB 970 (Berthold Technologies GmbH). The activity of DPP3 was determined using a 6-point calibration curve (0 (def. 3 U/L) - 645 U/L). Calibrators as well as samples were run in duplicates.

Assay performance studies

A full analytical evaluation of the DPP3 assays was performed on both variants using similar and complementary protocols. Assay precision profiles were determined by performing an inter-laboratory testing of a large number of plasma sample replicates(22,23). The interassay coefficient of variation (CV) was determined by measuring 26 human EDTA-plasma samples (range 0.02-156.0 ng/mL or 3,2-399 U/L) in duplicate. For each run one microtiter plate was used for calibrators and samples. These data were generated over seven days by six different operators for ten assay runs. Out of this analysis the limit of quantification (LoQ, or functional assay sensitivity (FAS)), defined as the DPP3 concentration quantifiable with a CV of 20%, was determined. The limit of detection (LoD) was determined as the upper two standard deviations (SD) of the lowest (i.e. zero) calibrator.

Accuracy was assessed by adding known concentrations of native DPP3 from blood cell lysates (20, 40, 60, 80, and 100 ng/mL or 60, 120, 180, 240 and 300 U/L, respectively) to EDTA plasma samples and comparing the measured DPP3 levels to expected concentrations/activities. For linearity studies, 10 random plasma samples were diluted serially in a range from 1:2 to 1:32 in heat-inactivated horse serum (Gibco® Thermofisher Scientific, Boston, USA) and the deviation from expected concentrations determined. Pools were generated from 20 EDTA-plasma samples pooling equal volumes (e.g. 60µL + 60µL) in different combinations.

For *ex vivo* stability studies fresh EDTA-plasma samples were collected, separated from cells within two hours of collection and stored up to 15 days at 4°C or room temperature. Aliquots were collected after 0, 2, 4, 8, 24, 48 hours and 15 days and stored at -80°C until measurement. To assess freeze/thaw stability, the fresh EDTA-plasma samples were frozen and thawed six times. The samples were stored frozen at -80°C for at least 24 hours for each freeze/thaw cycle.

The acceptance criterion for all stability, accuracy and linearity studies was $\pm 20\%$ difference from the original or expected concentration.

For *in vivo* stability analysis of the analyte purified recombinant His-hDPP3 (c=0.06 mg/kg) and vehicle were injected *i.v.* into healthy rats and blood drawn 5 min, 30 min, 1h, 3h, 6h and 24h after injection (n=3 per group). Levels of human DPP3 in rat serum were quantified using the DPP3-LIA. The in-life experimental procedures undertaken during the course of this study

were subject to the provisions of the directive 2010/63/EU of the European Parliament and the Council and the German Animal Welfare Act. The project was reviewed and approved by the ethical committee of the Landesamt für Arbeitsschutz, Verbraucherschutz und Gesundheit of the State of Brandenburg. The registration number is 2347-48-2017.

Analytical specificity was assessed by adding potential interfering substances within clinically relevant range to eight different EDTA-plasma samples: albumin 6 g/dL (BSA, Proliant biologicals, Ankeny, USA), bilirubin 40 mg/dL (Sigma-Aldrich, Taufkirchen, Germany), triglycerides 3 g/dL (SMOFlipid from Fresenius Kabi, Bad Homburg vor der Höhe, Germany), hemoglobin 500 mg/dL (Sigma-Aldrich) or heparin 3000 U/L (Heparin sodium salt, Sigma-Aldrich). The acceptance criterion for all interference studies was $\pm 20\%$ difference from original concentration.

Patients and controls

Residual, anonymized EDTA plasma samples initially collected for routine laboratory and clinical studies were provided by the Gemeinschaftslabor Cottbus, Germany. These samples were from patients with normal and increased DPP3 levels and were used for assay development. A cohort of 88 healthy subjects (57 females, 31 males, mean age (SD): 42.2 (+/- 12.7) years, without clinical evidence of acute disease or history of chronic illness) was used for correlation analysis

Samples from acute critically ill patients were randomly selected from the AdrenOSS study (ClinicalTrials.gov Identifier: NCT02393781). Hospital admission plasma samples from 175 patients diagnosed with severe sepsis and 153 patients diagnosed with septic shock were measured in both DPP3 assays. Differences in DPP3 levels between the two diagnoses as well as between groups of survivors and non-survivors of septic shock were analysed.

To assess the DPP3 normal distribution in healthy subjects, plasma samples from the Malmö Preventive Project (MPP) were measured. The Swedish single-center, prospective, population-based study was described recently(24). Of this 18,240-participants-study a subcohort was randomly selected (n=5,060) to determine the normal range of plasma DPP3. Excluding all participants that died or developed any cardiovascular disease during the time course of the study led to a final sample size of 2,256.

Written consent was obtained from all participants.

Statistical analysis

All statistical analyses were conducted with GraphPad Prism 6.0. Distribution was tested with the D'Agostino-Pearson omnibus test. We performed comparison of non-parametric data with the Mann-Witney U-test. Correlations were calculated as Spearman rank correlation. P values <0.05 were considered significant.

Acknowledgements

The underlying project of this report was aided by grants of the “Investitionsbank des Landes Brandenburg (ILB)” given to Sphingotec Therapeutics GmbH. We also thank the “Fonds zur Förderung der wissenschaftlichen Forschung (FWF)” for financial support through the PhD program “Molecular Enzymology” (W901). Furthermore, we thank Mandy Kaestorf (Sphingotec Therapeutics GmbH) for excellent technical assistance and Joachim Struck and Andrea Sparwaßer (Sphingotec GmbH) for consultancy.

References

1. Prajapati SC, Chauhan SS. Dipeptidyl peptidase III: a multifaceted oligopeptide N-end cutter. *FEBS J.* 2011;278:3256–76.
2. Ellis S, Nuenke JM. Dipeptidyl Arylamidase III of the Pituitary: Purification and Characterization. *J Biol Chem.* 1967;242:4623–9.
3. Shimamori Y, Watanabe Y, Fujimoto Y. Purification and Characterization of Dipeptidyl Aminopeptidase III from Human Placenta. *Chem Pharm Bull.* 1986;34:3333–40.
4. Vanha-Perttula T. Dipeptidyl peptidase III and alanyl aminopeptidase in the human seminal plasma: origin and biochemical properties. *Clin Chim Acta.* 1988;177:179–95.
5. Aoyagi T, Wada T, Kojima F, Nagai M, Harada S, Takeuchi T, et al. Enzymatic Changes in Cerebrospinal Fluid of Patients with Alzheimer-Type Dementia. *J Clin Biochem Nutr.* 1993;14:133–9.
6. Wattiaux R, Wattiaux-de Coninck S, Thirion J, Gasingirwa M-C, Jadot M. Lysosomes and Fas-mediated liver cell death. *Biochem J.* 2007;403:89–95.
7. Gamrekelashvili J, Kapanadze T, Han M, Wissing J, Ma C, Jaensch L, et al. Peptidases released by necrotic cells control CD8 + T cell cross-priming. *J Clin Invest.* 2013;123:4755–68.
8. Lee CM, Snyder SH. Dipeptidyl-aminopeptidase III of rat brain. Selective affinity for enkephalin and angiotensin. *J Biol Chem.* 1982;257:12043–50.
9. Baršun M, Jajčanin N, Vukelić B, Špoljarić J, Abramić M. Human dipeptidyl peptidase III acts as a post-proline-cleaving enzyme on endomorphins. *Biol Chem.* 2007;388:343–8.
10. Dostal DE, Hunt RA, Kule CE, Bhat GJ, Karoor V, McWhinney CD, et al. Molecular mechanisms of angiotensin II in modulating cardiac function: intracardiac effects and signal transduction pathways. *J Mol Cell Cardiol.* 1997;29:2893–902.
11. Roks A, Buikema H, Pinto YM, van Gilst WH. The renin-angiotensin system and vascular function. The role of angiotensin II, angiotensin-converting enzyme, and alternative conversion of angiotensin I. *Heart Vessels.* 1997;Suppl 12:119–24

12. Ferrario CM. Role of Angiotensin II in Cardiovascular Disease — Therapeutic Implications of More Than a Century of Research. *J Renin-Angiotensin-Aldosterone Syst.* 2006;7:3–14.
13. Corrêa TD, Takala J, Jakob SM. Angiotensin II in septic shock. *Crit Care.* 2015;19:98.
14. Tumlin JA, Murugan R, Deane AM, Ostermann M, Busse LW, Ham KR, et al. Outcomes in Patients with Vasodilatory Shock and Renal Replacement Therapy Treated with Intravenous Angiotensin II. *Crit Care Med.* 2018;46:949–57.
15. Pang X, Shimizu A, Kurita S, Zankov DP, Takeuchi K, Yasuda-Yamahara M, et al. Novel Therapeutic Role for Dipeptidyl Peptidase III in the Treatment of Hypertension. *Hypertension.* 2016;68:630–41.
16. Singh H, Kalnitsky G. alpha-N-benzoylarginine-beta-naphthylamide hydrolase, an aminoendopeptidase from rabbit lung. *J Biol Chem.* 1980;255:369–74.
17. Suhar A, Marks N. Purification and Properties of Brain Cathepsin B: Evidence for Cleavage of Pituitary Lipotropins. *Eur J Biochem.* 1979;101:23–30.
18. Lane RD. A short-duration polyethylene glycol fusion technique for increasing production of monoclonal antibody-secreting hybridomas. *J Immunol Methods.* 1985;81:223–8.
19. Hikawa N, Takenaka T. Method for production of neuronal hybridoma using emetine and actinomycin D. *Brain Res Brain Res Protoc.* 1997;1:224–6.
20. Jones TH, Kapralou a. A rapid assay for dipeptidyl aminopeptidase III in human erythrocytes. *Anal Biochem.* 1982;119:418–23.
21. Kumar P, Reithofer V, Reisinger M, Wallner S, Pavkov-Keller T, Macheroux P, et al. Substrate complexes of human dipeptidyl peptidase III reveal the mechanism of enzyme inhibition. *Sci Rep. Nature Publishing Group;* 2016;6:23787.
22. Armbruster DA, Pry T. Limit of blank, limit of detection and limit of quantitation. *Clin Biochem Rev. The Australian Association of Clinical Biochemists;* 2008;29 Suppl 1:S49-52.
23. Spencer CA, Takeuchi M, Kazarosyan M, MacKenzie F, Beckett GJ, Wilkinson E. Interlaboratory/intermethod differences in functional sensitivity of immunometric assays of

thyrotropin (TSH) and impact on reliability of measurement of subnormal concentrations of TSH. *Clin Chem.* 1995;41:367–74.

24. Melander O, Belting M, Manjer J, Maisel AS, Hedblad B, Engstrom G, et al. Validation of Plasma Proneurotensin as a Novel Biomarker for the Prediction of Incident Breast Cancer. *Cancer Epidemiol Biomarkers Prev.* 2014;23:1672–6.

Chapter 5

Peptidomics based approach to identify endogenous substrates of DPP3

Peptidomics based approach to identify endogenous substrates of DPP3

Shalinee Jha,¹ Rolland Hellinger,² Ulrike Taschler,³ Robert Zimmermann,³ Christian Gruber,² and Peter Macheroux¹

¹Institute of Biochemistry, Graz University of Technology, Austria

²Center for Physiology and Pharmacology, Medical University of Vienna, Austria

³Institute of Molecular Biosciences, University of Graz, Austria

Author contributions

P.M. initiated the project; P.M., R.Z., C.G., R.H., S.J., and U.T. designed research; S.J., R.H., U.T. performed research; S.J., R.H., U.T., C.G., and P.M. analyzed data and interpreted experimental results; S.J. and P.M. wrote the manuscript.

Keywords: Dipeptidyl peptidase 3, knockout mice, Peptidomics, LC-MS, substrate identification

Abbreviations:

DPP3, Dipeptidyl Peptidase-3; WT, Wild-type; RAS, Renin-Angiotensin Pathway; LC-MS/MS, Liquid Chromatography-tandem Mass Spectrometry; SDS-PAGE, sodium dodecyl sulfate–polyacrylamide gel electrophoresis

Abstract

DPP3 plays many important roles in controlling physiological functions through regulation of bioactive peptides. While DPP3 has been implicated in various pathophysiological processes, the underlying peptides and pathways regulated by this enzyme are less clear. The identification of endogenous substrates of DPP3 is an important step in elucidating the molecular mechanisms of this peptidase. Most recently, peptidomics approaches have been applied to investigate the substrate scope of many enzymes. These approaches can be utilized for the discovery of bioactive substrates and biochemical characterization of the enzyme. Here, we employed liquid chromatography–mass spectrometry-based peptidomics on DPP3-knockout mice to enable the discovery of endogenous substrates directly from tissues. The information collected from this method may serve to better understand the biochemical and physiological functions of DPP3. A comparison of the sequences of the peptides that change with those that do not change in the absence of DPP3 can also be employed to better understand the features that govern specificity of DPP3 towards peptide substrates.

Introduction

DPP3 is a zinc-dependent exopeptidase expressed in several mammalian tissues. It is also a component of the human central proteome, which comprises of a set of proteins ubiquitously expressed in all human cells. DPP3 contributes to the processing of peptide hormones, opioid peptides and other bioactive peptides (1). Bioactive peptides regulate physiology by controlling a wide variety of important biological processes. Some of the functions mediated by bioactive peptides are pain modulation, sleep regulation and gastrointestinal activity (2-5). Other bioactive peptides control complex social behaviors like emotions and sexual activity (6, 7). Given this wide range of biology regulated by bioactive peptides, it is a possibility that DPP3 could itself potentially be involved in affecting a large number of physiological processes. Although DPP3 has suspected biological roles like pain modulation, blood pressure regulation and defense against oxidative stress, the molecular pathways through which they achieve these functions remain unknown. Additionally, it may be involved in some other *in vivo* functions which are still largely unknown.

While substrates of DPP3 were traditionally discovered using activity-based screening (8-10), this approach is tedious and limited by the commercial availability of prospective peptide substrates. Peptidomics based approaches have been developed in the recent years which allow global assessments of peptide levels and easy identification of even slightly differing peptide species, such as those that may result from post-translational modifications (11-14). These advantages make peptidomics a powerful method for characterizing the full set of endogenous substrates regulated by DPP3. In this study, we conducted a global comparative peptidome analysis in order to define the range of accepted substrates for DPP3. This technique involved extraction and purification of peptides from DPP3 knockout (DPP3^{-/-}) and control wildtype (WT) mice brain followed by incubation with inactive recombinant purified human DPP3 protein and subsequent analysis using liquid chromatography and electrospray ionization mass spectrometry. By examining the relative amount of a peptide that varied between WT mice and mice lacking the peptide-processing DPP3, it was possible to define the substrate range of the enzyme in the brain tissue. Peptides which increased in DPP3^{-/-} mice relative to WT are putative substrates of the DPP3, whereas peptides that decreased in DPP3^{-/-} mice relative to WT mice are putative products of the enzyme. Peptides that do not change between the two genotypes are presumably processed redundantly by multiple peptidases, such that deletion of DPP3 does not have an effect on peptide levels.

Results and Discussion

A mass list of all MS1 runs of the samples was generated and compared to the mass list of peptide samples from two different databases (Mascot and Proteinscape) with a cut-off within +/-12 ppm window. Individual MS2 spectra were additionally confirmed manually. This generated a list of 140 peptides. Relative quantification was done by taking into account the peak intensities of peptides. However, there were many redundant peaks belonging to the same peptide. This was corrected by summing up peak intensities. Additionally, prior knowledge about the substrate preference of DPP3, for example the length of the peptide that can be processed, was considered. This narrowed down the list to 12 peptides that were upregulated in the DPP3^{-/-} mice and can be potential substrates of DPP3. Many of these peptides belong to the endogenous opioid system and the renin-angiotensin circuit as expected. But some novel peptides like apelin-13, cholecystokinin, and urotensin II are also detected.

Peptides identified by LC-MS based peptidomics			
DPP3 ^{-/-} Elevated Peptides	Fold Change	DPP3 ^{+/+} Elevated Peptides	Fold Change
Angiotensin 1-4 (4 aa)	2.0	Angiotensin 1-5 (5 aa)	2.0
Angiotensin II (8 aa)	2.0	Angiotensin 1-7 (7 aa)	2.2
Apelin-13 (13 aa)	10.7	Arg-vasopressin (9 aa)	2.2
Bradykinin (9 aa)	2.1	Cortistatin-14 (14 aa)	2.3
Cholecystokinin-12 (12 aa)	2.7	Met-enkephalin (5 aa)	5.3
Dynorphin A(1-17) (17 aa)	2.2	Neuropeptide AF (18 aa)	22.7
Leu-enkephalin (5 aa)	2.5	Substance P (11 aa)	3.6
Melanin-Concentrating Hormone (19 aa)	2.6		
Neurokinin B (10 aa)	3.7		
Nociceptin (17 aa)	2.5		
Somatostatin-14 (14 aa)	2.0		
Urotensin II (6 aa)	2.6		

Table 1 List of peptides identified by peptidomics along with the fold-change according to the quantification of their peak intensities.

Interestingly, apelin-13 shares functions similar to angiotensin II which is a known substrate of DPP3 (15, 16). Both these peptides are involved in regulating blood pressure and water intake in the body. Urotensin II is a potent vasoconstrictor and is associated with cardiovascular diseases, atherosclerosis, diabetes, renal dysfunction, hypertension, and

obesity (17). This reinforces the notion that DPP3 plays a major role in the physiology of heart, kidney and accessory blood vessels.

Neuropeptide AF, which is an anti-opioid neuropeptide involved in pain modulation and endocrine functions, was found to be elevated in the WT mice. However, considering the length of this peptide, it is highly probable that this is due to a feedback signaling cascade and does not involve a direct interaction with DPP3.

The results are generally consistent with a major role for DPP3 in the generation of peptides from the opioid and renin-angiotensin system. Though this method is useful for a rapid screening of potential substrates, there can be many sources of error such as sample variations and redundant peaks for a single peptide. Extensive studies are required in the future to further validate this method for DPP3 substrate identification. Peptidomics should be complemented with biochemical interaction studies to improve the quality and reliability of the results.

Material and Methods

Ethics Statement

All animal experiments were formally approved by the *Ethics Committee of the University of Graz* and the *Austrian Federal Ministry of Science and Research*.

Animals and generation of DPP3 knockout mice

All studies were conducted in age-matched DPP3^{-/-} and WT control male mice on C56BL/6J background. Mice were bred and maintained at regular housing temperatures (23 °C) and 14-h light/10-h dark cycle. Animals had ad libitum access to water and chow diet (4.5% fat, 34% starch, 5.0% sugar, and 22.0% protein; Ssniff Spezialdiäten). Breeding and genotyping were done according to standard procedures. For generation of DPP3 KO mice, targeted mutant ES cells were obtained from EUCOMM and injected into blastocytes of C57Bi/6 mice. Chimeric animals with a high degree of coat color chimerism were bred with C57BI/6 mice. The construct containing a β -galactosidase cassette (lacZ) and a promoter-driven selection cassette (neo) was inserted into the *dpp3* gene. Additionally, the construct contained two flippase recognition target (FRT) sites for flippase recombination enzyme (FLP)-mediated recombination flanking lacZ and neo. The selection cassette and exon 6 (essential for DPP3 function), flanked by loxP sites, were removed by breeding with transgenic C57BI/6 mice expressing cre-recombinase (CMV-Cre). Cre-lox recombination resulted in deletion of neo and exon 6 leaving the lacZ reporter gene intact. Mice totally lacking *dpp3* were bred by crossing mice heterozygous for the mutant *dpp3* allele lacking neo and exon 6.

Tissue collection

Animals were anesthetized with isoflurane using the bell jar method and subsequently killed by cervical dislocation and tissues were surgically removed. The tissues were weighed and 5 μ l of ice-cold double distilled water was added per mg of tissue weight. Homogenization was performed on ice in using an Ultra Turrax (IKA, Staufen, Germany).

Extraction of peptides

Peptide extraction was done as described in (12). In brief, the sonicated tissues were incubated at 70°C for 20 mins followed by cooling on ice for 15 mins. The homogenates were then acidified by adding ice-cold 0.1 M HCl to a final concentration of 10 mM. The acidified homogenates were mixed by vortexing and left on ice for an additional 15 mins. The

homogenates were then centrifuged at 13000 g for 40 min at 4°C. The supernatants were then transferred to low-retention tubes (Eppendorf, Hamburg, Germany). The pH of the peptide extracts was adjusted to 8.0 by adding 0.1 M NaOH.

Recombinant human DPP3 (hDPP3) production and purification

The genes encoding for the catalytically inactive E451A variant of hDPP3 (1–726) used in this study was cloned and inserted into a pET28a vector. Cloning into the vectors and deletion of the stop codon allowed production of the protein with a hexahistidine affinity tag at the N-terminus for the inactive E451A variant. Thereafter, the plasmids containing the desired constructs were transformed into a BL21-CodonPlus (DE3) RIL strain. The cell culture was grown in Luria-Bertani (LB) medium containing 50 µg ml⁻¹ kanamycin for inactive DPP3-E451A. Gene expression was induced with 0.4 mM isopropyl-1-thio-D-galactopyranoside (IPTG) after the culture medium reached an OD of 0.6–0.8. After being allowed to grow overnight at 18 °C, the cells were harvested by centrifugation at 4000 g for 10 min. The harvested cell pellet was resuspended in 50 mM Tris-HCl pH 8.0 containing 150 mM NaCl, 10 mM imidazole (lysis buffer) and was lysed by sonication. Centrifugation at 18,000 g for 1 hour at 4 °C was performed to remove cell debris and the supernatant was subjected to affinity chromatography on Ni-NTA resin (5 mL prepacked His-trap FF, GE Healthcare) previously equilibrated with lysis buffer. Then the column was washed with lysis buffer supplemented with 20 mM imidazole. After washing, bound protein was eluted using lysis buffer containing 300 mM imidazole. The fractions containing target protein were pooled and concentrated with centrifugal filter units (Amicon Ultra-15, 50 kDa; Millipore, MA, USA). The purity of the fractions was analyzed by 12.5% SDS-PAGE. Concentrated protein was re-buffered to 50 mM Tris, 100 mM NaCl, pH 8.2 with a PD-10 desalting column.

Pull-down of peptide extracts with inactive hDPP3

The peptide extracts from DPP3^{-/-} and control WT mice were incubated with 100 nM hDPP3E451A for 1 hour at RT. The peptide extract was then loaded onto a Ni-NTA column (1 mL prepacked His-trap, GE Healthcare) previously equilibrated with lysis buffer. Then the column was washed with lysis buffer supplemented with 20 mM imidazole. After washing, bound protein was eluted using lysis buffer containing 300 mM imidazole. The eluted mixture containing the inactive hDPP3 and bound peptides was heated at 80°C for 15 mins to inactivate the protein followed by centrifugation at 14000 g to remove the protein precipitate. The peptides were further purified using centrifugal filter units (Amicon Ultra Ultracel, 10

kDa; Millipore, MA, USA). The peptides were desalted on PepClean C-18 spin columns (Pierce, Thermo Fisher Scientific, MA, USA) according to the manufacturer's instructions using acetonitrile and trifluoroacetic acid solutions. Finally, the peptides were eluted with 40 μ l of 70% acetonitrile in water. The eluates were concentrated to 10-20 μ l in a vacuum centrifuge and stored at -80°C for further measurements.

Separate peptides and detect by LC/MS

The peptide samples were thawed and briefly microcentrifuged at maximum speed to remove particulates. Peptide extract was analyzed via LC-MS on a QqTOF compact (Bruker Daltonics, Billerica, MA) and peptides were separated with a PepMap Acclaim capillary column (Thermo Fisher Scientific; 150 \times 0.3 mm, 2 μ m 100 Å) using a Dionex Ultimate 3000 UPLC system. Proteinscape software package (v. 3.1.5 474; Bruker Daltonics) together with the Mascot algorithm (Matrixscience, MA) was used for data analysis and database search. A list of MS1 annotation peaks was generated for the peptides. The annotated peaks were verified by manual *de novo* analysis using Biotools 3.0 (Bruker Daltonics). Peaks from oxytocin, vasopressin, angiotensin 1-10 were used as reference.

Acknowledgements

This work was supported by a grant from the Austrian Science Foundation (FWF) through grants W901 (Doctoral Program “Molecular Enzymology”) to PM and RZ. The authors are also grateful for the support by the interuniversity program in natural sciences (NAWI Graz).

References

1. Kumar P, Reithofer V, Reisinger M, Wallner S, Pavkov-Keller T, Macheroux P, et al. Substrate complexes of human dipeptidyl peptidase III reveal the mechanism of enzyme inhibition. *Scientific reports*. 2016 Mar 30;6(1):10.
2. Szentirmai E, Hajdu I, Obal F, Krueger JM. Ghrelin-induced sleep responses in ad libitum fed and food-restricted rats. *Brain Res*. 2006 May 09;1088(1):131-40.
3. Ohno K, Sakurai T. Orexin neuronal circuitry: role in the regulation of sleep and wakefulness. *Front Neuroendocrinol*. 2008 Jan;29(1):70-87.
4. De Felipe C, Herrero JF, O'Brien JA, Palmer JA, Doyle CA, Smith AJ, et al. Altered nociception, analgesia and aggression in mice lacking the receptor for substance P. *Nature*. 1998 Mar 26;392(6674):394-7.
5. Cummings DE, Overduin J. Gastrointestinal regulation of food intake. *The Journal of clinical investigation*. 2007 Jan;117(1):13-23.
6. Fichna J, Janecka A, Costentin J, Do Rego J. The endomorphin system and its evolving neurophysiological role. *Pharmacol Rev*. 2007 Mar;59(1):88-123.
7. Bodnar RJ. Endogenous opiates and behavior: 2013. *Peptides*. 2014 Dec;62:67-136.
8. Ellis S, Nuenke JM. Dipeptidyl arylamidase III of the pituitary. Purification and characterization. *J Biol Chem*. 1967 Oct 25;242(20):4623-9.
9. Lee CM, Snyder SH. Dipeptidyl-aminopeptidase III of rat brain. Selective affinity for enkephalin and angiotensin. *J Biol Chem*. 1982 Oct 25;257(20):12043-50.
10. Smyth M, O'Cuinn G. Dipeptidyl Aminopeptidase III of Guinea-Pig Brain: Specificity for Short Oligopeptide Sequences. *Journal of Neurochemistry*. 1994 -10-01;63(4):1439-45.
11. Lim J, Berezniuk I, Che F, Parikh R, Biswas R, Pan H, et al. Altered neuropeptide processing in prefrontal cortex of Cpe.sup.fat/fat mice: implications for neuropeptide discovery. *Journal of Neurochemistry*. 2006 Feb 1;96(4):1169.
12. Lyons PJ, Fricker LD. Peptidomic approaches to study proteolytic activity. *Curr Protoc Protein Sci*. 2011 Aug;Chapter 18:Unit18.13.
13. Wardman J, Fricker LD. Quantitative peptidomics of mice lacking peptide-processing enzymes. *Methods in molecular biology (Clifton, N.J.)*. 2011;768:307.
14. Che F, Biswas R, Fricker LD. Relative quantitation of peptides in wild-type and Cpe(fat/fat) mouse pituitary using stable isotopic tags and mass spectrometry. *Journal of mass spectrometry : JMS*. 2005 Feb;40(2):227.
15. Yamaleyeva LM, Shaltout HA, Varagic J. Apelin-13 in blood pressure regulation and cardiovascular disease. *Curr Opin Nephrol Hypertens*. 2016 09;25(5):396-403.

16. Taheri S, Murphy K, Cohen M, Sujkovic E, Kennedy A, Dhillon W, et al. The effects of centrally administered apelin-13 on food intake, water intake and pituitary hormone release in rats. *Biochem Biophys Res Commun.* 2002 Mar 15;291(5):1208-12.

17. Ames RS, Sarau HM, Chambers JK, Willette RN, Aiyar NV, Romanic AM, et al. Human urotensin-II is a potent vasoconstrictor and agonist for the orphan receptor GPR14. *Nature.* 1999 -09;401(6750):282-6.

Appendix

**Oxidative stress induced structural changes in the microtubule-associated flavoenzyme
Irc15p from *Saccharomyces cerevisiae***

**Karin Koch¹, Emilia Strandback¹, Shalinee Jha¹, Gesa Richter², Benjamin Bourgeois²,
Tobias Madl² and Peter Macheroux¹,**

¹Institute of Biochemistry, Graz University of Technology, Austria

²Institute of Molecular Biology and Biochemistry, Medical University of Graz, Austria

Author contributions

P.M. initiated the project; K.K., E.S., G.R., S.J., B.B., T.M. and P.M. designed the experiments and interpreted the data. K.K. and E.S. produced and purified Irc15p. K.K., E.S. and S.J. performed analytical, biochemical and enzymatic experiments. G.R. and B.B. performed SAXS measurements. K.K., E.S., S.J., G.R., B.B. and P.M. wrote the manuscript.

Keywords: oxidative stress; thiol modification; flavin adenine dinucleotide; lipoamide dehydrogenase; microtubule-binding protein;

Abbreviations:

A. vinelandii, *Azotobacter vinelandii*; DCPIP, 2,6-dichlorophenol-indophenol; DTT, dithiothreitol; E. coli, *Escherichia coli*; Irc15, increased recombination centers 15; LPD, lipoamide dehydrogenase; MQ, menadione; MTT, 3-(4,5-Dimethyl-2-thiazolyl)-2,5-diphenyl-2H-tetrazolium bromide; ROS, reactive oxygen species; S. cerevisiae, *Saccharomyces cerevisiae*; S. seoulensis, *Streptomyces seoulensis*; STH, soluble pyridine nucleotide-transhydrogenases

Abstract

The genome of the yeast *Saccharomyces cerevisiae* encodes a canonical lipoamide dehydrogenase (Lpd1p) as part of the pyruvate dehydrogenase complex and a highly similar protein termed Irc15p (increased recombination centers 15). In contrast to Lpd1p, Irc15p lacks a pair of redox active cysteine residues required for the reduction of lipoamide and thus it is very unlikely that Irc15p performs a similar dithiol-disulfide exchange reaction as reported for lipoamide dehydrogenases. We expressed *IRC15* in *Escherichia coli* and purified the produced protein to conduct a detailed biochemical characterization. Here, we show that Irc15p is a dimeric protein with one FAD per protomer. Photoreduction of the protein generates the fully reduced hydroquinone without the occurrence of a flavin semiquinone radical. Similarly, reduction with NADH or NADPH yields the flavin hydroquinone without the occurrence of intermediates as observed for lipoamide dehydrogenase. The redox potential of Irc15p was -313 ± 1 mV and is thus similar to lipoamide dehydrogenase. Reduced Irc15p is oxidized by several artificial electron acceptors, such as potassium ferricyanide, 2,6-dichlorophenol-indophenol, 3-(4,5-dimethyl-2-thiazolyl)-2,5-diphenyl-2*H*-tetrazolium bromide and menadione. However, disulfides, such as cystine, glutathione and lipoamide were unable to react with reduced Irc15p. Limited proteolysis and SAXS-measurements revealed that the NADH-dependent formation of hydrogen peroxide caused a substantial structural change in the dimeric protein. Therefore, we hypothesize that Irc15p undergoes a conformational change in the presence of elevated levels of hydrogen peroxide, which is a putative biomarker of oxidative stress. This conformational change may in turn modulate the interaction of Irc15p with other key players involved in regulating microtubule dynamics.

Introduction

Reactive oxygen species (ROS), such as hydrogen peroxide (H₂O₂), superoxide anions ($\cdot\text{O}_2^-$), and hydroxyl radicals ($\cdot\text{OH}$) are constantly generated during aerobic respiration. Organisms employ various strategies to preserve an intrinsic balance in the overall redox environment within the cell by simultaneously producing low levels of ROS essential for physiological signaling processes. An imbalance between the production of ROS and the antioxidant defenses to eliminate these toxic intermediates can lead to oxidative damage to DNA, lipids, and proteins, generating cellular stress. (1) In the recent past, an increasing number of proteins have been identified that use reversible ROS-mediated thiol modifications to regulate their function. Similar to other post-translational modifications, oxidative thiol modifications are fully reversible, the extent of which depend on the reactivity and accessibility of cysteine thiols and the concentration of ROS present. Under oxidative stress conditions in the cell, these thiol modifications can become irreversible, leading to deleterious effects on protein structure and function.(2-4)

In this study we report an uncharacterized flavoprotein from the yeast *Saccharomyces cerevisiae*, which was found to be structurally sensitive to oxidative damage. The genome of *S. cerevisiae* features 68 genes that were identified to encode a flavoprotein. Despite being a widely utilized model organism biochemical information on the flavoproteome is rather limited. For example, Irc15p (increased recombination centers 15) has a sequence similarity of 59% to the FAD-containing yeast lipoamide dehydrogenase 1 (Lpd1p) (5). Although it was demonstrated that Irc15p is associated with microtubules and regulates their dynamics (6), it is currently unclear whether the protein carries a flavin cofactor not to mention the potential properties and function of the putative enzymatic activity. This lack of information prompted us to recombinantly produce Irc15p and study its properties.

Lipoamide dehydrogenases (LPDs) orchestrate the reversible transfer of electrons between dihydrolipoamide to the enzyme-bound FAD cofactor and NAD⁺. Generally, LPDs possess a second redox active group that is composed of two cysteine residues capable of forming an internal disulfide. This internal dithiol-disulfide exchange communicates the electrons between the lipoamide and the FAD cofactor and is thus an essential asset of LPDs (7, 8). LPDs also constitute a component of oxoacid dehydrogenases that are large multienzyme complexes. In these complexes, LPDs reoxidize the covalently bound lipoamide cofactor of

the transacylase component. (9) Interestingly, Irc15p lacks the two essential cysteines required for the formation of a disulfide and therefore it is most unlikely that Irc15 is a redundant LPD or even exhibits similar enzymatic properties. Apparently, *IRC15* evolved after the whole genome duplication of *S. cerevisiae* and the duplicated *LPD1* sequence subsequently evolved to attain a new function (“neofunctionalization”) (10, 11). This new function appears to be connected to the regulation of microtubule dynamics and chromosome segregation (6). However, it is not known what exactly this function is let alone whether this function is compatible with the properties of a putative LPD homolog.

LPDs are members of the family of flavoprotein disulfide reductases that catalyze the NAD(P)H-dependent reduction of disulfide containing substrates. To perform this reaction the enzymes are equipped with a flavin cofactor and another non-flavin redox center. Initially only three members, namely LPD, glutathione reductase and thioredoxin reductase composed the enzyme family, which has expanded significantly in recent years (7). In 2012, the family was classified according to the nature and position of the non-flavin redox center into five sub groups (8). Group one comprises the flavoprotein disulfide reductases with the classical sequence motif CXXXXC, such as LPD. Members of group two are structurally related but contain a second cysteine based redox center. Enzymes from group three contain only one cysteine, which either forms a cysteine sulfenic acid or a cysteine-coenzyme A mixed disulfide during the reaction. Members of group four contain the classical sequence motif but catalyze a non-disulfide reductase reaction. Finally, members of group five feature two cysteines that are widely separated in the primary sequence.

In addition to these five sub-groups, several proteins described in the literature exhibit high sequence similarity with flavoprotein disulfide reductases, but lack some significant features. For example, pyridine nucleotide transhydrogenases (STH) catalyzes the reversible transfer of electrons between NADH and NADP⁺ and lack at least one of the redox active cysteines and a histidine residue essential for catalytic activity (7, 12). These enzymes are also closely related to LPD, for example, STH from *Escherichia coli* exhibits 27% identity and 45% similarity to several LPDs (13). However, also LPDs themselves are able to catalyze transhydrogenase reactions (14). Another example is LpdA from *Mycobacterium tuberculosis*, which lacks one cysteine as well as the catalytic histidine and glutamate. Like STH the protein is not able to catalyze the reduction of disulfides but instead features quinone reductase activity. The physiological relevance of this protein is unknown (15). In the present work, we

recombinantly produced Irc15p in *E. coli*. The purified Irc15p shows the typical characteristics of a flavoenzyme. We have demonstrated that Irc15p is efficiently reduced by NADH but lacks disulfide reductase activity. However, reduced Irc15p reduces a range of artificial electron acceptors, such as potassium ferricyanide, 2,6-dichlorophenol-indophenol (DCPIP) and quinones. The potential role of Irc15p as a microtubule-associated protein is discussed in light of our findings concerning the enzymatic properties and structural changes that occur upon exposure to hydrogen peroxide.

Results

Biochemical characterization of Irc15p

Initially, Irc15p was produced with a C-terminal hexa-histidine tag as described by Keyes and Burke. (6) However, the protein could not be purified successfully due to weak binding to the Ni-NTA sepharose resin. Therefore, we employed a C-terminal nona-histidine tag enabling the successful purification of ~13 mg of protein from 1 L culture with a purity of >95% as judged by visual inspection of SDS-PAGE and by using the program ImageJ (<http://imagej.nih.gov/ij/>) (16) (Figure 1, panel A). The presence of DTT in the buffer was critical to prevent the precipitation of Irc15p.

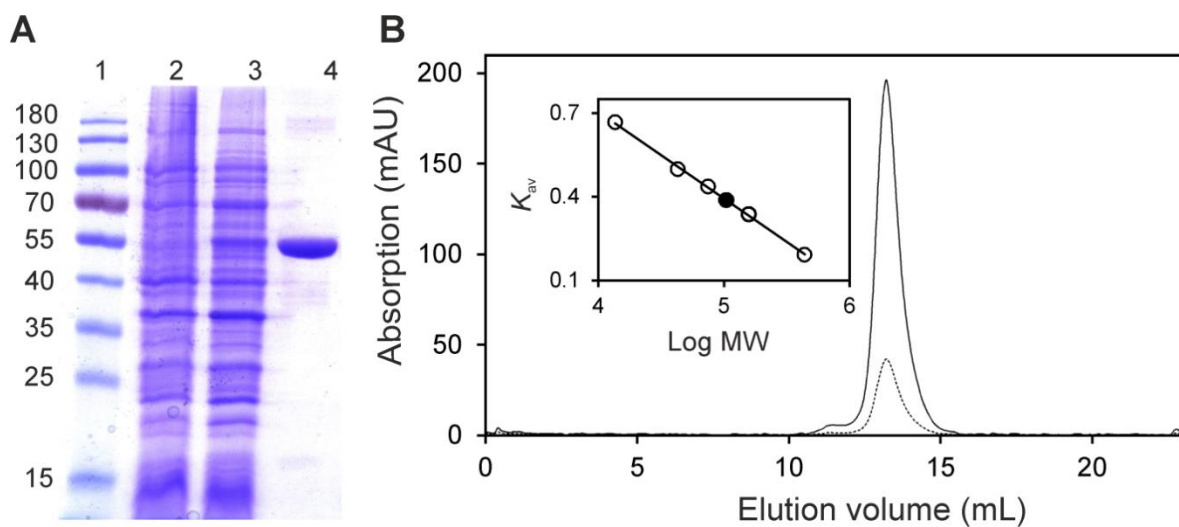


Figure 1 Determination of the purity and molecular mass of Irc15p using SDS-PAGE and analytical size exclusion chromatography. (A) Determination of purity and subunit molecular mass of Irc15p by SDS-PAGE after purification by affinity chromatography. Lane 1, PageRuler™ prestained protein ladder (10-180 kDa); lane 2, protein extract before induction; lane 3, protein extract after induction of IRC15; lane 4, protein fraction after purification by Ni-NTA-sepharose. The subunit molecular mass of Irc15p was estimated to ~55 kDa. (B) Determination of native molecular mass of Irc15p (solid and dotted line display the absorption at 280 nm and 450 nm, respectively) using analytical size exclusion chromatography. The insert shows a plot of the partition coefficient (K_{av}) against the logarithm of molecular mass of standard proteins (ferritin, 440 kDa; aldolase, 158 kDa; conalbumin, 75 kDa; ovalbumin, 43 kDa; ribonuclease A, 13.7 kDa). The calculated

molecular mass of *Irc15p* (~ 113 kDa, black circle) indicates that *Irc15p* is present as a dimer.

Analytical size exclusion chromatography yielded a molecular mass of ~115 kDa confirming that *Irc15p* forms a homodimer as previously reported by Keyes and Burke (6). The protein peak was associated with a yellow color indicating the presence of a flavin cofactor in agreement with the high sequence similarity to the FAD-dependent LPD (Figure 1, panel B). To assess the chemical identity of the flavin cofactor, *Irc15p* was denatured and the released flavin was analyzed by HPLC. A peak was obtained at a retention time of 9.1 min closely corresponding to the retention time of authentic FAD (9.05 min). Furthermore, the purified protein exhibited the absorption characteristics of a flavoprotein and also looks very similar to lipoamide dehydrogenases, with two distinct peaks at 377 and 453 nm with a shoulder at ~470 nm (17). Denaturation of the protein resulted in a slight bathochromic shift of the absorption maxima at 453 nm (Figure 2, panel A). Using an extinction coefficient of $11.300 \text{ M}^{-1} \text{ cm}^{-1}$ at 450 nm for free FAD (18) an extinction coefficient of $11.900 \text{ M}^{-1} \text{ cm}^{-1}$ at 453 nm was calculated for *Irc15p*. This extinction coefficient was used to determine the concentration of *Irc15p* in further experiments. The A_{280}/A_{450} ratios of purified *Irc15p* were usually between 4.3 and 4.5.

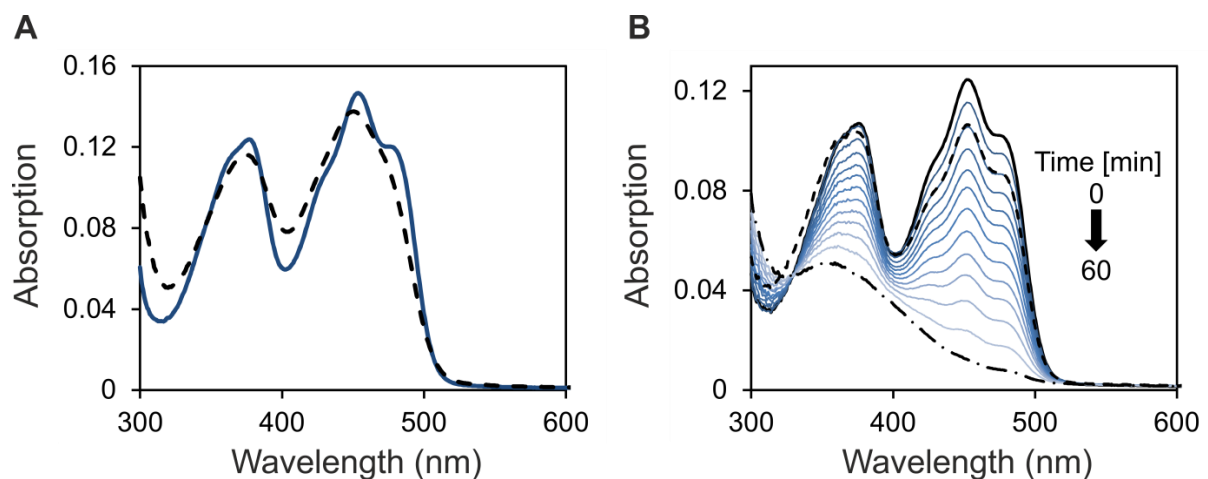


Figure 2 UV/Vis absorption spectroscopy. (A) UV-visible absorption spectrum of *Irc15p* before (solid line) and after denaturation (dashed line). Denaturation of purified *Irc15p* was carried out in buffer B (50 mM HEPES, 50 mM NaCl, 1 mM DTT, pH 7.0) containing 0.2% SDS. (B) Absorption spectra observed during the anaerobic photoreduction of *Irc15p* in 50 mM HEPES, 50 mM NaCl, 1 mM DTT, 1 mM EDTA, pH 7.0. The solid black line

represents the spectrum before irradiation. The reduction proceeds as indicated by the arrow with the dashed dotted line representing the final spectrum. After reoxidation by dioxygen the protein was partially denatured. The solution was cleared by centrifugation and the spectrum recorded (dashed line).

Photoreduction of Irc15p in the presence of EDTA led to the formation of the fully reduced flavin (hydroquinone) without the formation of a semiquinone radical (Figure 2, panel B). After reoxidation and removal of precipitated protein the obtained UV-vis absorption spectrum was similar to the initial spectrum indicating that reduction is fully reversible and does not give rise to chemical alterations of the flavin (Figure 2, panel B). The redox potential of the FAD cofactor was determined with the xanthine/xanthine oxidase system in the presence of safranin T ($E_M = -289$ mV). According to the method of Minnaert (19) a plot of $\log(\text{Irc15p}_{\text{ox}}/\text{Irc15p}_{\text{red}})$ versus $\log(\text{dye}_{\text{ox}}/\text{dye}_{\text{red}})$ was used to estimate the redox potential to -313 ± 1 mV (six independent measurements). In agreement with the photoreduction, reduction of Irc15p occurred without formation of a semiquinone and accordingly the slope of the logarithmic plot was close to unity indicating that the reference dye as well as the isoalloxazine moiety of the flavin took up two electrons (Figure 3).

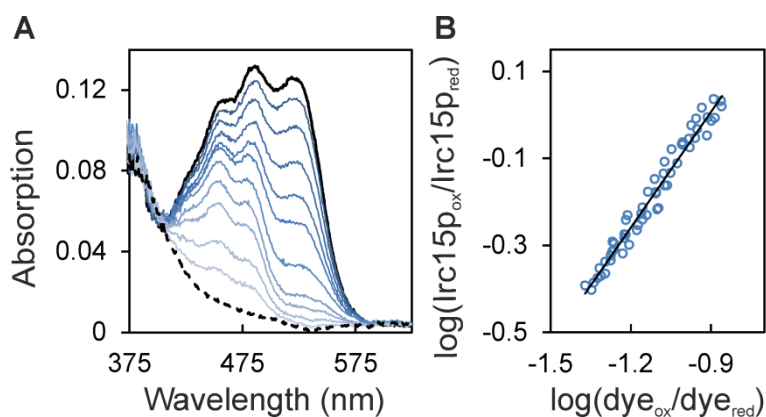


Figure 3 Redox potential determination of Irc15p in the presence of safranin T. (A) The absorption spectrum of the fully oxidized and fully reduced species are represented by a solid and dashed black line, respectively. Selected spectra of the course of reduction are represented in different shades of blue. Ten μM Irc15p was reduced by the xanthine/xanthine oxidase electron delivering system in the presence of safranin T over a time period of ~ 100 min. Data points for evaluation were extracted at 430 nm and 530 nm for Irc15p and for the dye safranin T, respectively. (B) Double logarithmic plot of the concentration of oxidized/reduced Irc15p vs. the concentration of oxidized/reduced safranin T (Nernst plot).

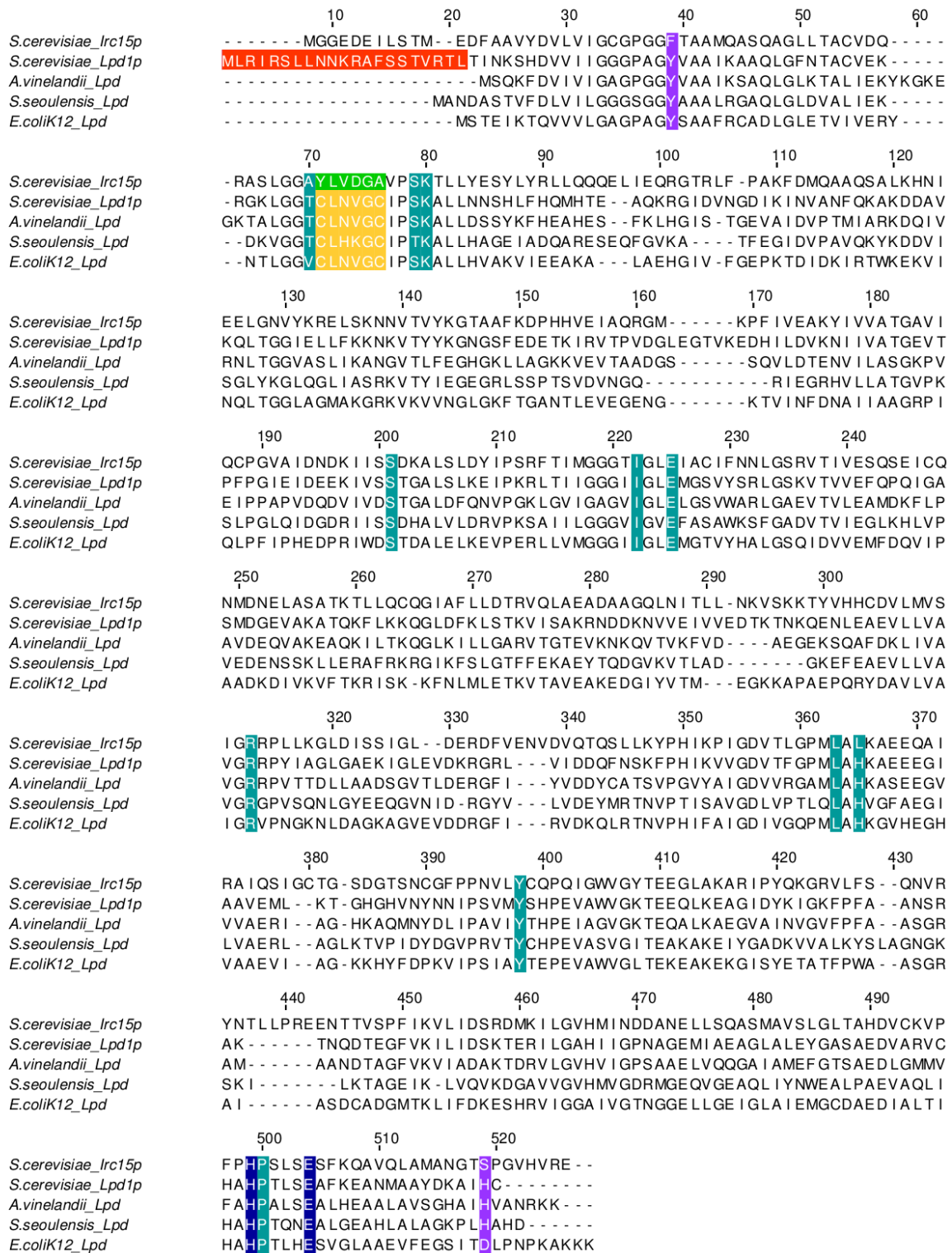


Figure 4 Alignment of the *Irc15p* protein sequence with sequences of *LPD* from *S. cerevisiae*, *E. coli*, *S. seoulensis* and *A. vinelandii*. The mitochondrial targeting sequence of *Lpd1p* is

highlighted in red. The amino acid signature near the redox-active disulfide is highlighted in yellow. The respective sequence in *Irc15p* is highlighted in green. The catalytic His-Glu diad is highlighted in blue. Other residues in the active site are highlighted in petrol. Residues involved in structural stabilization are highlighted in purple.

Sequence alignment and homology modeling

A multiple sequence alignment using the amino acid sequence of *Irc15p* and the sequences of LPD from *S. cerevisiae*, *E. coli*, *Streptomyces seoulensis* and *Azotobacter vinelandii* was generated (Figure 4). The sequence identities of *Irc15p* and various LPDs are presented in Table 1 (20, 21).

Table 1 Sequence identity of *Irc15p* in comparison to other LPDs from *S. cerevisiae*, *E. coli*, *Streptomyces seoulensis* and *Azotobacter vinelandii*.

Percent identity to <i>Irc15p</i>	
<i>S. cerevisiae</i> _Lpd1p	40
<i>A. vinelandii</i> _Lpd	30
<i>S. seoulensis</i> _Lpd	28
<i>E. coli</i> K12_Lpd	27

A structural model of *Irc15p* was computationally generated using Lpd1p from *S. cerevisiae* (PDB entry: 1V59) as template (Figure 5, panel A and B) (22, 23). A comparison of the close environment of the FAD cofactor from *Irc15p* (Figure 5, panel C) and Lpd1p (Figure 5, panel D) reflects a high sequence conservation: out of 16 residues that are within 4 Å of the flavin isoalloxazine ring only four are different. Notably, among these are the two cysteines, C44 and C49, which make up the dithiol/disulphide redox centre of Lpd1p. These are replaced by tyrosine and alanine, respectively. The two amino acid residues that compose the catalytic diad, *i.e.* H457 and E462 are conserved in both proteins (17).

Enzymatic properties and thermal stability of *Irc15p*

To gain information on the specificity of the electron donor, the reductive half-reaction was studied using stopped-flow spectrophotometry. Reduction of *Irc15p* with NADH was fast and monophasic. The rate of reduction was analysed as a function of substrate concentration and

fitted to a hyperbolic equation yielding a limiting reductive rate of $250 \pm 3 \text{ s}^{-1}$ and a dissociation constant of $100 \pm 5 \text{ }\mu\text{M}$ (Figure 6, panel A). As noted above, no semiquinone radical was observed (Figure 6, panel A, inset). In contrast to reduction by NADH, the reduction with NADPH exhibited two phases (Figure 6, compare panel B and C) and the bimolecular rate constant determined at $100 \text{ }\mu\text{M}$ NAD(P)H is an order of magnitude lower (NADH = $1.2 \cdot 10^6 \text{ M}^{-1} \cdot \text{s}^{-1}$, NADPH = $3.4 \cdot 10^5 \text{ M}^{-1} \cdot \text{s}^{-1}$).

To evaluate the enzymatic activity of Irc15p, assays with NAD(P)H and several potential electron acceptors were performed (Table 2). No activity was observed with disulfides such as lipoic acid, glutathione or cystine. On the other hand, the enzyme showed

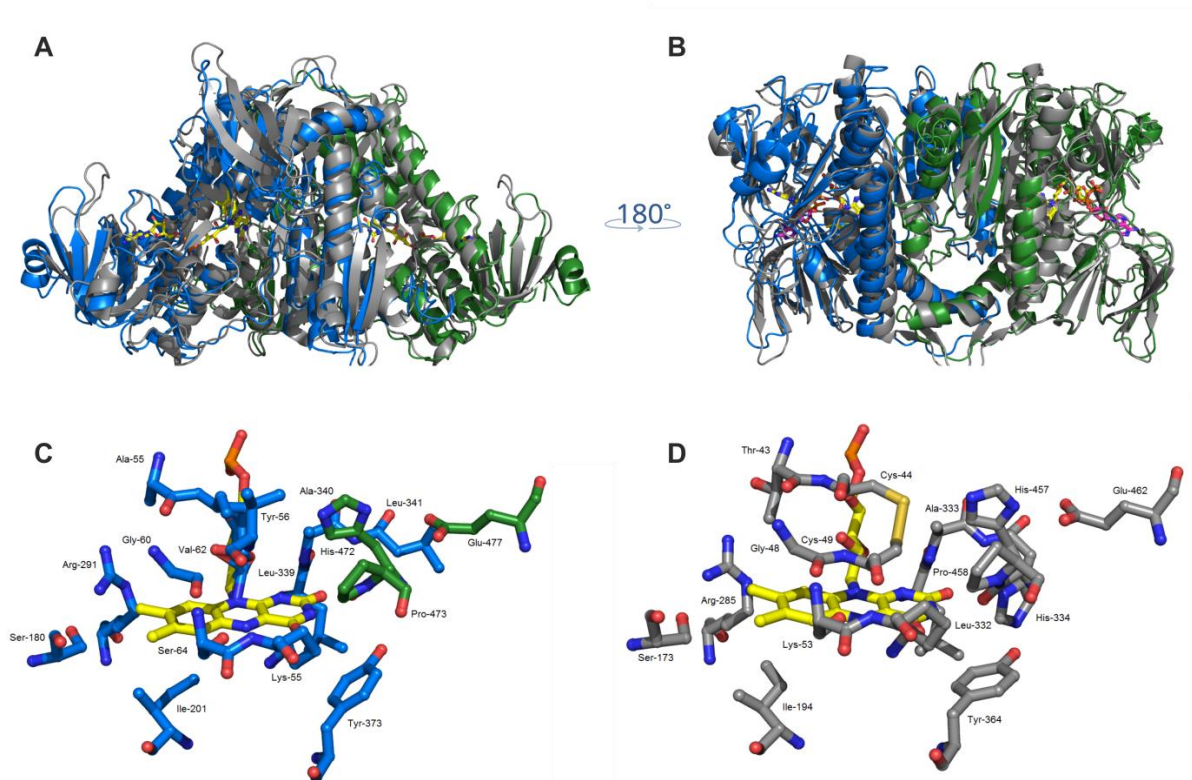


Figure 5 Overall structural similarity of Irc15p and LPD1p. (A) and (B): Structural superposition of LPD1p (grey, PDB code: 1V59) and Irc15p (blue/green). The FAD cofactor is displayed in yellow and NADH is shown in magenta. Close-up view of the active sites of Irc15p (C) and LPD1p (D). Residues close to the FAD isoalloxazine ring are illustrated as grey sticks for both protomers (Lpd1p) or in colors corresponding to the respective protomer (Irc15p). Figures were prepared with the software PyMOL (24).

diaphorase activity with the non-specific electron acceptors potassium ferricyanide, 3-(4,5-dimethyl-2-thiazolyl)-2,5-diphenyl-2H-tetrazolium bromide (MTT), and 2,6-dichlorophenol-

indophenol (DCPIP) and quinone reductase activity with menadione (MQ). Furthermore the reduced cofactor was reoxidized by molecular oxygen, however at a comparatively sluggish rate. A clear preference for NADH as electron donor is only observed in steady-state assays employing potassium ferricyanide as electron acceptor.

*Table 2 Specific activities with standard deviations of Irc15p with NAD(P)H [$\mu\text{mol}/\text{min}^{-1}/\text{mg}^{-1}$] as electron donor in comparison with the specific activity of LPD from *S. seoulensis* (25) and LPD from *S. cerevisiae* (in brackets) (26) with NADH. Reduction of ferricyanide, DCPIP and MTT was determined at 420, 600 and 578 nm, respectively. All other reactions were monitored at 380 nm.*

Substrate	Specific Activity with NADH [$\mu\text{mol}/\text{min}^{-1}/\text{mg}^{-1}$] ^a	Specific Activity with NADPH [$\mu\text{mol}/\text{min}^{-1}/\text{mg}^{-1}$] ^a	Specific Activity of LPD with NADH [$\mu\text{mol}/\text{min}^{-1}/\text{mg}^{-1}$] ^c
Ferricyanide	179.5 \pm 3.41	17.9 \pm 1.14	7.87 (1670.0 ^d)
DCPIP ^b	3.88 \pm 0.14	4.72 \pm 0.22	61.4 (2.0 ^d)
MQ ^{*,b}	19.7 \pm 0.82	19.3 \pm 2.12	7.18
MTT [*]	1.62 \pm 0.08	1.28 \pm 0.02	-
Lipoic acid [*]	0	0	15.6
Cystine [*]	0	0	0.80
Glutathione [*]	0	0	0.18
Oxygen [*]	1.0 \pm 0.02	1.0 \pm 0.02	0

^aThe reaction mixture for the measurements of Irc15p contained 50 mM HEPES, pH 7.0, 50 mM NaCl, 10 nM DTT, 500 μM NAD(P)H, 500 μM electron acceptors (except MQ and DCPIP). ^bThe concentration of DCPIP and MQ were 50 and 200 μM , respectively. ^cThe reaction mixture for the measurements of LPD from *S. seoulensis* contained 50 mM sodium phosphate buffer, pH 7.4, 0.3 mM substrates and 0.2 mM NADH. ^dThe reaction mixture for the potassium ferricyanide assay of LPD1 from *S. cerevisiae* contained 165 mM sodium acetate, pH 4.8, 0.7 mg/mL bovine serum albumin, 1 mM EDTA, 600 μM NADH, 670 μM potassium ferricyanide. The DCPIP assay contained phosphate buffer, pH 7.2, 0.7 mg/mL bovine serum albumin, 1 mM EDTA; 600 μM NADH and 40 μM DCPIP.

The potassium ferricyanide assay was further used to determine the influence of various pH values and salt concentrations on the enzymatic activity of Irc15p. The highest activity was observed at pH 7.0 without salt in the assay buffer. Below and above pH 7.0 the activity is reduced by about 14-49%, and the presence of 150 mM NaCl decreased the activity at pH 7.0 by 40%.

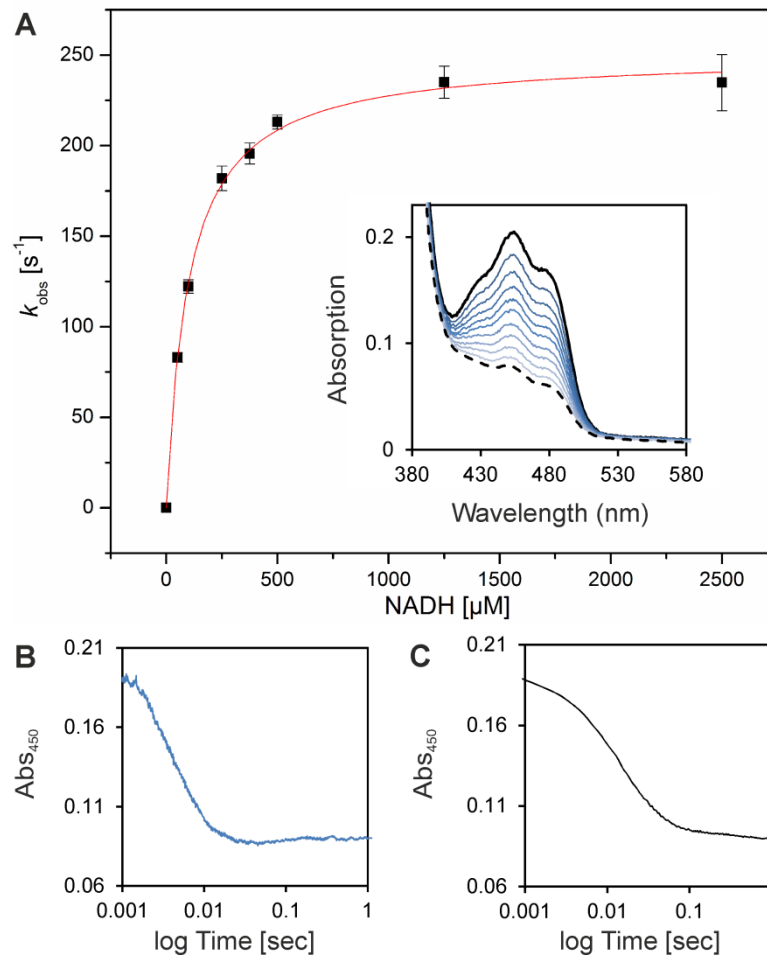


Figure 6 Pre-steady-state kinetics of Irc15p to determine reductive rates for NADH. (A) The rate of reduction was determined under anoxic conditions with the stopped flow device equipped with a diode array detector. At least three independent measurements were performed (error bars are shown as standard deviations). The inset displays selected absorption spectra of the reduction of $\sim 20 \mu\text{M}$ Irc15p with $375 \mu\text{M}$ NADH. (B) Absorption change at 450 nm of the reduction of $\sim 20 \mu\text{M}$ Irc15p with $1250 \mu\text{M}$ NADH. (C) Absorption change at 450 nm of the reduction of $\sim 20 \mu\text{M}$ Irc15p with $1000 \mu\text{M}$ NADPH.

The thermal stability of Irc15p was monitored using a thermal shift assay, performed with the fluorescent dye SYPRO[®] Orange. (27) Under optimal conditions, Irc15p displays a rather high thermal stability of about 70 °C (Table 3).

Table 3 Activity and thermal stability of Irc15p at various pH and in the absence and presence of NaCl. Melting points are given as the average of two independent measurements.

Buffer composition	Activity [%]	T _m [°C]
50 mM HEPES, pH 6.0	51	70
50 mM HEPES, pH 7.0	100	69
50 mM HEPES, pH 8.0	86	62
50 mM Tris/HCl, pH 9.0	46	56
50 mM HEPES, pH 7.0, 150 mM NaCl	61	69

The reaction mixture for the activity assay contained also 10 nM DTT, 500 μM NADH and 500 μM ferricyanide.

Additionally, measurements were performed in the presence and absence of NADH, NAD⁺, NADPH and NADP⁺, as summarized in Table 4. Interestingly a significant decrease in melting temperature could be observed after addition of an excess of NADH or NADPH.

Limited proteolysis

To further study the effect of NAD(P)H on the protein stability, limited proteolysis using tryptic digestion was performed under oxic and anoxic conditions in the presence and absence of NADH. As displayed in Figure 7A, Irc15p is more sensitive to proteolysis in the presence of NADH and molecular oxygen showing degradation already after 1 hour whereas the control sample is stable overnight. Interestingly, when the same experiment was performed under anoxic conditions, no degradation was detectable after six hours and became apparent only after 16 hours.

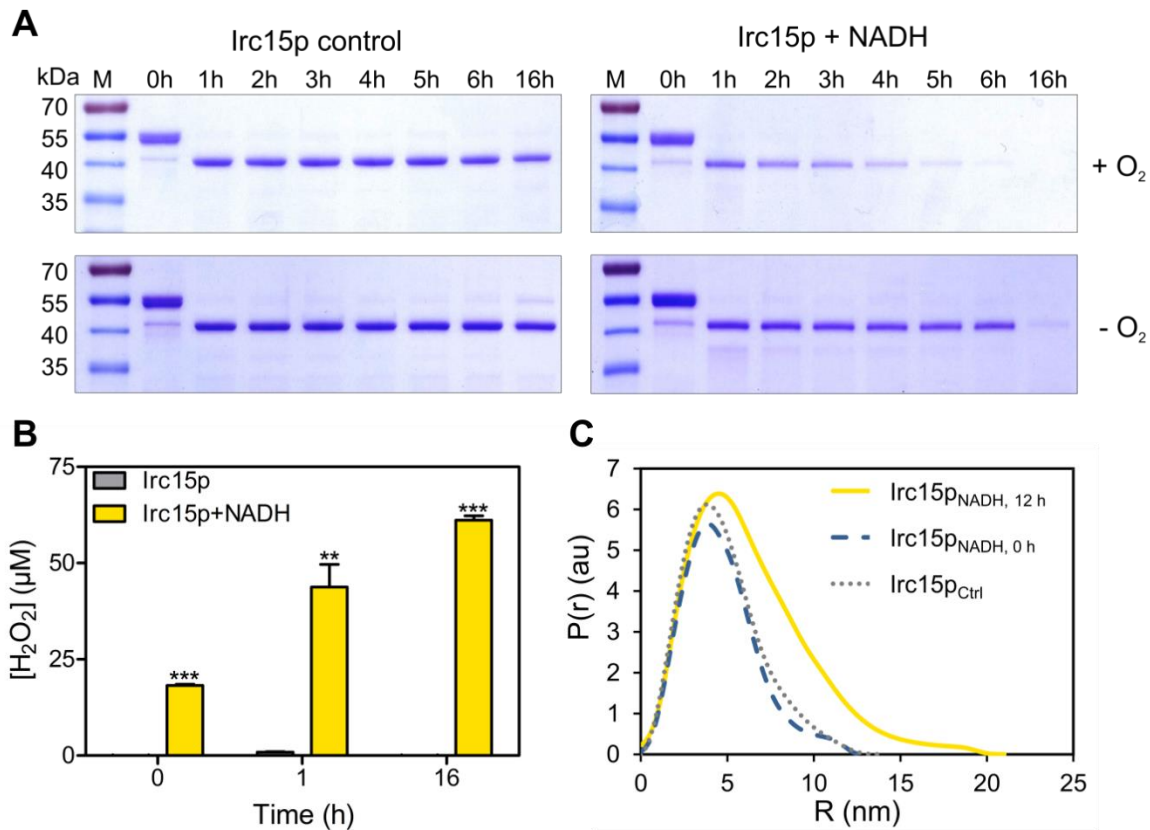


Figure 7 Limited proteolysis, hydrogen peroxide formation and SAXS data for Irc15p in the presence and absence of NADH. (A) SDS-PAGE from the limited proteolysis experiment illustrating the effect of NADH and oxygen on the stability of the protein. Each gel has the marker PageRuler™ prestained protein ladder in lane 1, the remaining lanes display the samples incubated for 0-16 hours. (B) Hydrogen peroxide formation in Irc15p over time (0, 1 and 16 hours) and in the presence and absence of NADH. (C) SAXS data comparing the experimental radial density distribution ($P(r)$) of Irc15p incubated with NADH measured after 0 and 12 hours compared to a control sample without NADH.

Hydrogen peroxide production

Since our limited proteolysis experiments demonstrated that NADH and molecular oxygen play a synergistic role, we hypothesized that the reduction of Irc15p by NADH and subsequent reoxidation by dioxygen led to the generation of hydrogen peroxide, which in turn may oxidize cysteine residues accessible on the surface of the protein. To assess this, we determined the production of hydrogen peroxide over a period of time by Irc15p in the presence of NADH under aerobic conditions. As expected, there was a marked increase in the level of hydrogen peroxide in the presence of NADH. In contrast, Irc15p without NADH showed no significant peroxide production (see Figure 7B).

Table 4 Thermal stability of Irc15p in 50 mM HEPES, 50 mM NaCl, 1 mM DTT, pH 7.0 in the presence and absence of 50 mM NADH, 50 mM NAD⁺, 50 mM NADPH, 50 mM NADP⁺ and 50 mM sodium dithionite. Melting points are determined as the average of two independent measurements.

Condition	T _m [°C]
Control	68
NADH	47
NAD ⁺	64
NADPH	45
NADP ⁺	68
Sodium dithionite	65

SAXS measurements of Irc15p

In order to further investigate the potential impact of thiol oxidation on the overall structure of the protein, SAXS measurements were employed. Irc15p formed a dimer in solution with a radius of gyration (R_g) of 3.64 ± 0.02 and with a maximum distance (D_{max}) of 14 nm. However, incubation of Irc15p with NADH in the presence of molecular oxygen resulted in a substantial change of the radius of gyration (R_g) and of the maximal diameter (D_{max}) indicating that the dimer adopts a more extended conformation (Irc15p with NADH measured directly: $R_g = 3.56 \pm 0.01$, $D_{max} = 13$ nm, Irc15p with NADH measured after 12 hours: $R_g = 5.44 \pm 0.03$, $D_{max} = 21$ nm, Figure 7, panel B). The SAXS data implicate that the presence of NADH is extending the conformation of Irc15p by 60%.

Discussion

In this study, we have demonstrated that Irc15p is a flavoprotein with FAD as the cofactor. Recombinant Irc15p features characteristic spectral properties that are similar to those reported for LPDs (Figure 2, panel A). In contrast to LPDs, reduction of Irc15p does not give rise to the typical red charge transfer absorption at longer wavelength (~530 nm) owing to the lack of a pair of redox active cysteines near the FAD cofactor. (25, 28) Instead, reduction by light as well as with NAD(P)H yielded the fully reduced FAD hydroquinone without the occurrence of a semiquinone radical (Figures 2, panel B and Figure 6).

The redox potential determined for Irc15p is shifted by 93 mV to -313 ± 1 mV compared to free flavin (= -220 mV). The redox potentials determined for LPD from *E. coli* were $E_{\text{ox}}/\text{EH}_2 = -264$ mV and $\text{EH}_2/\text{EH}_4 = -314$ mV and were assigned to the redox potentials of the disulfide/dithiol and the FAD/FADH₂ couple, respectively (28). In order to confirm this assignment, Hopkins *et al.* (29) created two variants lacking either one of the two participating thiol groups, *i.e.* the variants C44S and C49S. The redox potentials of these variants were -379 and -345 mV, respectively, suggesting that the more negative redox potential determined for wild-type LPD belongs to the FAD/FADH₂ couple. Thus the redox potential of the FAD/FADH₂ couple of Irc15p is very similar to that of LPD suggesting that the environment of the FAD cofactors in these proteins is comparable.

Furthermore, we have demonstrated that the thermal stability of the protein is rather high ($T_m = 70$ °C). This is not unusual as the reported melting temperature for LPD from *A. vinelandii* is even higher ($T_m = 80$ °C). (30) Interestingly, it was shown that an exchange of Y16 to phenylalanine leads to a decrease of the melting temperature to 72 °C, since Y16 stabilizes the interaction of the subunits via hydrogen bond formation to H470. (31) In Irc15p phenylalanine is found in position 16 and H470 is replaced by serine. Therefore, the lower melting temperature of Irc15p may be accounted for, at least in part, by the amino acid changes in these positions.

To determine the substrate specificity of Irc15p the reductive half reaction was investigated using either NADH or NADPH. These measurements established a clear preference for NADH as electron donor proceeding with a limiting rate of $k_{\text{red}} = 250$ s⁻¹ (Figure 6). Thus, the limiting rate of Irc15p is an order of magnitude lower than that of lipoamide dehydrogenase (250 s⁻¹ vs. >3000 s⁻¹). (32, 33) Since Irc15p is associated with microtubules and was shown

to regulate their dynamics, the rapid reduction by NADH and the obvious conformational change occurring in the presence of NADH sheds new light on its potential role in processes such as mitosis. In recent years, several studies concluded that the NAD^+/NADH ratio and the overall redox status are regulatory elements of the cell cycle and the dynamics of the cytoskeleton. (34-36) It was shown that the NAD^+/NADH ratio is high during the G0 phase, decreases during the S phase before it increases again in the G2 phase. However, no information is available of the NAD^+/NADH ratio during mitosis. (35) Furthermore, it has been demonstrated that NAD^+ has an influence on the stability and curvature of microtubules. Since it is not interacting directly with the polymer it has been proposed, that NAD^+ affects microtubule binding proteins on the plus-end of the polymer.³⁴ How exactly the redox state influences the cell cycle and the cytoskeletal dynamics is not known, but several proteins regulating the cell cycle as well as tubulin contain redox sensitive elements like cysteines or cofactors where modifications may occur. (37, 38) Therefore, it is conceivable that reduced Irc15p interacts with these proteins and reduces oxidized groups, *e.g.* disulfides, to enable for example the polymerization of tubulins. This reactivity would clearly fit to the mode of action found in LPDs, where an internal disulfide in proximity to the isoalloxazine moiety of FAD is reduced to the dithiol via reduction of the flavin by NAD(P)H. In search for such an activity we tested a variety of disulfides, such as cystine, glutathione and lipoamide but we were unable to detect any reduction of these compounds (Table 2). However, we discovered that artificial electron acceptors such as potassium ferricyanide, DCPIP, MTT and MQ were good to excellent electron acceptors (Table 2).

A similar observation was reported for LpdA from *Mycobacterium tuberculosis*, which contains five homologs of flavoprotein disulfide reductases (7). Apparently, LpdA does not reduce disulfide containing compounds but similar to Irc15p reduces quinones. (7) Interestingly, LpdA lacks one of the two cysteines near the FAD and the catalytic His-Glu diad, in other words it shares the absence of the dithiol-disulfide redox center with Irc15p but on the other hand also lacks the catalytic diad, which is present in Irc15p. Since the catalytic diad is important in the oxidative half reaction of disulfide reductases, *i.e.* the formation of the internal disulfide by oxidation through the external disulfide (the “dithiol-disulfide exchange reaction”), its presence in Irc15p suggests that it has retained the ability to catalyze a similar reaction.

Limited proteolysis experiments performed in the presence and absence of NADH under oxic and anoxic conditions showed that Irc15p became more susceptible to degradation in the presence of NADH and oxygen. Furthermore, we showed that the formation of hydrogen peroxide was responsible for the increased sensitivity toward tryptic digestion. In keeping with this, SAXS measurements for Irc15p indicated time-dependent conformational change in Irc15p that resulted in a more extended and possibly more flexible structure. This structural change can be attributed to the presence of 11 cysteine residues per subunit of Irc15p, many of which are present on the surface. Cysteine is the most reactive and oxygen-sensitive amino acid due to the presence of the side chain thiol group. ROS-mediated oxidation of these thiols involves formation of sulfenic, sulfinic and sulfonic acids. While the sulfenic intermediates can be re-converted to their reduced form, thereby modulating protein activity, the sulfinic and sulfonic acid states are irreversible in nature and can cause decreased protein stability. This phenomenon is called hyperoxidation and can be induced during oxidative stress. (39) NADH-mediated generation of H₂O₂ shown here mimics oxidative stress conditions in the yeast cell, where the excessive ROS accumulation may result from a plethora of sources such as electron leakage originating in the mitochondrial transport chain, hyperoxia, upregulation of certain enzymes such as D-amino acid oxidases and peroxisomal acyl-coenzyme A oxidases, xenobiotics and environmental factors such as heat stress. (1) The study presented here showed that the yeast flavoprotein Irc15p is susceptible to redox-regulated conformational change, which can potentially impair its interaction with tubulin leading to a negative regulation of the microtubule dynamics. (6)

Materials & Methods

Materials

All chemicals, reagents and enzymes were of highest quality and from Sigma-Aldrich (St. Louis, USA), Roth (Karlsruhe, Germany) or Thermo Fisher Scientific (Waltham, USA), unless otherwise noted. Columns for affinity chromatography (Ni-NTA-sepharose), size exclusion chromatography (Superdex 200 10/300 GL) and buffer exchange (PD-10 desalting column) were from GE Healthcare (Little Chalfont, UK). The *E. coli* strains Top10 and RosettaTM(DE3) were from Invitrogen (Carlsbad, USA) and Merck (Darmstadt, Germany), respectively. The plasmid pET21d was from Merck (Darmstadt, Germany).

Cloning of IRC15 for large scale expression in *E. coli*

All strains were generated using standard genetic techniques (40, 41). Briefly, genomic DNA from *S. cerevisiae* was extracted with the yeast DNA extraction kit from VWR (Radnor, USA). According to the sequence for *IRC15* from the *Saccharomyces* genome database (42) the following primers were designed and synthesized from VBC (Vienna, Austria): fw_5'-GAACCATGGCAATGGGAGGTGAAGACGAAATATTAAGCAC-3'; rev_5'-GAGCCTCGAGTTAATGGTGATGATGGTGATGATGATGATGATGTTCCCGGACATGTACGCCAG -3'. To construct the heterologous expression vector pET21d(+)*IRC15* introducing an additional C-terminal 9x-histidine tag the restriction enzymes NcoI/XhoI were used. Individual clones were sequenced before transforming the plasmid into *E. coli* RosettaTM(DE3) cells.

Heterologous production and purification of Irc15p

A single colony of *E. coli* Rosetta(DE3) comprising pET21d(+)*IRC15* was used to inoculate a pre-culture that was aerobically incubated (37 °C, 16 h, 150 rpm) in terrific broth media (bacto-tryptone 12 g/L, bacto-yeast extract 24 g/L, glycerol 4g/L, KH₂PO₄ 2.31 g/L and K₂HPO₄ 12.54 g/L) supplemented with 100 µg·mL⁻¹ ampicillin and 20 µg·mL⁻¹ chloramphenicol. 1% pre-culture was used to inoculate the main-culture supplemented with 100 µg·mL⁻¹ ampicillin and 10 µg·mL⁻¹ chloramphenicol, which was incubated aerobically at 37 °C with agitation at 150 rpm until an OD₆₀₀ of ~0.6 was reached. Production of the recombinant protein was induced by addition of 0.5 mM isopropyl-β-D-thiogalactoside and the culture was further incubated for 16 h at 20 °C. Cells were harvested by centrifugation at 4.500 g at 4 °C and washed once with 1% saline solution. Cell pellets were resuspended in 4 mL/g pellet buffer A (50 mM HEPES, 150 mM NaCl, 1 mM dithiothreitol, pH 7.0)

supplemented with 30 mM imidazole, 1 mM phenylmethylsulfonyl fluoride dissolved in dimethylsulfoxide, 10 μ M flavin adenine dinucleotide disodium salt hydrate. Furthermore, 1 μ L of protease inhibitor cocktail for the purification of histidine-tagged proteins from Sigma-Aldrich (St. Louis, USA) was added per 1 g of cell pellet. Cell disruption was achieved by sonication with a Labsonic L instrument from Braun Biotech International (Berlin, Germany) with 120 Watt for 3 x 3 min in an ice-water bath with 3 min pauses between each cycle. The cell lysate was centrifuged at 38.850 g for 45 min at 4 °C, and the supernatant was loaded onto a 5-mL HisTrap HP column previously equilibrated with buffer A supplemented with 30 mM imidazole. The column was washed with five column volumes with buffer containing 50 mM HEPES, pH 7.0, 150 mM NaCl, 1 mM DTT and 100 mM imidazole. Then the column was washed with buffer A supplemented with 100 mM imidazole and subsequently proteins were eluted with buffer A supplemented with 350 mM imidazole. Fractions containing target protein were pooled and concentrated with centrifugal filter units (Amicon Ultra-15, 50 kDa; Millipore, Massachusetts, USA). Concentrated protein was re-buffered to buffer B (50 mM HEPES, 50 mM NaCl, 1 mM DTT, pH 7.0) with a PD-10 desalting column. The protein solutions were shock frozen and stored at -80 °C if not used immediately.

Determination of molecular mass of Irc15p

The subunit molecular mass of purified Irc15p was determined by SDS-PAGE with a 12.5% separating gel and 5% stacking gel under reducing conditions described by Laemmli (43). The molecular mass marker PageRuler™ (prestained protein ladder 10-180 kDa) from Thermo Fisher Scientific (Waltham, USA) was used. To determine the native molecular mass of Irc15p size exclusion chromatography with Buffer A using a Superdex 200 10/300 GL column attached to an Äktapurifier™ system from GE Healthcare (Little Chalfont, UK) was performed. Protein elution was monitored at 280 nm and 450 nm. The column was calibrated with molecular mass standards according to the instructions from GE healthcare.

Determination of the flavin cofactor bound to Irc15p

To determine the nature of the flavin cofactor concentrated protein samples were treated with 8 M guanidine hydrochloride (pH 2 adjusted with concentrated HCl). Denatured protein was removed by centrifugation (13.000 g, 5 min) and the solution was neutralized with concentrated NaOH. To remove residual protein centrifugal filter units (Amicon Ultra-0.5 mL 10 kDa; Millipore, Massachusetts, USA) were used. The flow-through was concentrated at 50 °C under reduced pressure and subsequently analysed by HPLC (UltiMate® 3000 HPLC

system from Dionex, California, USA) using an Atlantis[®] dC18 5 μ M (4.6 x 250 mm) column. As liquid phase a 0.1% TFA solution and acetonitrile containing 0.1% TFA were used. The concentration of the organic solvent was increased within 20 min from 0% to 95% in a linear gradient (T = 25 °C; flow rate = 1 mL/min). The samples were analysed using a diode array detector at 280, 370 and 450 nm. The retention times of authentic FAD, FMN and riboflavin were 9.05, 9.75 and 10.4 min, respectively.

Determination of the redox potential

The redox potential was determined by the dye-equilibration method using the xanthine/xanthine oxidase electron delivering system as described by Massey (44). Reactions were carried out in buffer C (50 mM HEPES, 50 mM NaCl, pH 7) supplemented with methyl viologen (2.5 μ M) as mediator, 500 μ M xanthine, and xanthine oxidase in catalytic amounts (~40 nM) and lasted 0.5-2 h at 25 °C. The protein concentration for a typical experiment was ~10 μ M. The concentrations given are final values after mixing in the flow cell. Experiments were performed with a SF-61SX2 stopped flow device from TgK Scientific Limited (Bradford-on-Avon, UK) equipped with an auto-shutter to reduce photochemical effects during the experiment. To maintain anoxic conditions the device was positioned in a glove box from Belle Technology (Weymouth, UK). Absorption spectra during the course of reduction were recorded with a KinetaScanT diode array detector from TgK Scientific Limited (Bradford-on-Avon, UK). Safranin T was used as a reference dye for the analysis (-289 mV). The amounts of oxidized and reduced Irc15p and safranin T were quantitated at 430 nm and 530 nm, respectively. The reduction-oxidation potentials were calculated from plots of $\log(\text{Irc15p}_{\text{ox}}/\text{Irc15p}_{\text{red}})$ versus $\log(\text{dye}_{\text{ox}}/\text{dye}_{\text{red}})$ according to Minnaert (19) using Excel 2010 (Microsoft, Redmond, WA, USA).

Sequence alignment and homology modeling

A multiple sequence alignment was generated with the program Clustal Omega (21) with sequences taken from the *Saccharomyces* genome database⁴⁰ and from the UniProt database²⁰. A computational prediction approach was employed to construct the model structure of Irc15p. Tertiary structure of the protein was generated using protein homology-based molecular modeling software Swiss-Model (22) and *ab initio* threading based software I-TASSER (23). Both the programs used Lpd1p from *S. cerevisiae* (PDB entry: 1V59) as the top threading template for automated model building.

Methods using UV-visible absorption spectroscopy

Absorption spectra were recorded with a Specord 200 plus spectrophotometer from Analytik Jena (Jena, Germany) at 25 °C using 1-cm quartz cuvettes.

Extinction coefficient

The extinction coefficient of Irc15p was determined according to Macheroux (18). Briefly, Irc15p bound FAD was released by addition of 0.2% SDS. Absorption spectra were recorded before and after denaturation of the enzyme. The calculation yielded an extinction coefficient of 11.900 M⁻¹ cm⁻¹ at 453 nm for Irc15p.

Anoxic photoreduction

Photoreduction was carried out as described by Macheroux (18). Briefly, ~10 μM Irc15p in 1 mL buffer B (50 mM HEPES, 50 mM NaCl, 1 mM DTT, pH 7.0) supplemented with 1 mM EDTA was deoxygenated by incubation for 2 h in a glove box from Belle Technology (Weymouth, UK). A 10 W LED floodlight (Luminea) was used to reduce the cofactor by light irradiation. Absorption spectra were recorded after each reduction step until no further spectral changes were observed. Thereafter the sample was exposed to air and a spectrum was recorded after complete reoxidation.

Steady state kinetics

Initial-velocity kinetic measurements were performed in triplicates with NAD(P)H as electron donor and the disulfide containing electron acceptors lipoic acid, glutathione and cystine and the artificial electron acceptors potassium ferricyanide, MQ, MTT and DCPIP. Reaction mixtures were setup in buffer C (50 mM HEPES, 50 mM NaCl, pH 7). All reactions were initiated by addition of 5 μL enzyme stock solution supplemented with 200 nM DTT to the reaction mixture – final enzyme concentrations were 10 nM. Controls were performed in the absence of enzyme. Rates of reduction with MQ, oxygen and disulfide containing substrates were determined by fitting the observed absorption change at 380 nm in the first minute using adapted extinction coefficients (NADH $\epsilon_{380 \text{ nm}} = 1.210 \text{ M}^{-1} \cdot \text{cm}^{-1}$ or NADPH $\epsilon_{380 \text{ nm}} = 1.280 \text{ M}^{-1} \cdot \text{cm}^{-1}$). For the other electron acceptors pertinent wavelengths and extinction coefficients were used (ferricyanide $\epsilon_{420 \text{ nm}} = 1.040 \text{ M}^{-1} \cdot \text{cm}^{-1}$; MTT $\epsilon_{578 \text{ nm}} = 13.000 \text{ M}^{-1} \cdot \text{cm}^{-1}$; DCPIP $\epsilon_{600 \text{ nm}} = 21.000 \text{ M}^{-1} \cdot \text{cm}^{-1}$) (39).

Thermal shift assay

Thermal shift assays were performed as described by Ericsson *et al.* (27). 20 μL of $\sim 13 \mu\text{M}$ Irc15p protein solution was pipetted into a white 96-well RT-PCR plate from Bio-Rad (California, USA) both at different pH, in the absence and presence of 150 mM NaCl and in buffer B in the presence and absence of a final concentration of 50 mM NADH, 50 mM NAD^+ , 50 mM NADPH, 50 mM NADP^+ or 50 mM sodium dithionite. Two μL of a 1:500 dilution of SYPRO[®] orange from Molecular Probes (Oregon, USA) was added. The plates were sealed with an Optical-Quality Sealing Tape from Bio-Rad (California, USA) and heated in a CFX Connect[™] Real-Time PCR detection system from Bio-Rad (California, USA) from 20 to 95 °C in increments of 0.5 °C/5 sec. Fluorescence changes of the dye were detected at a wavelength between 470 and 500 nm. Melting temperatures (T_m) were determined using CFX Manager 3.0 software from Bio-Rad (California, USA).

Determination of kinetic rates

The protein was deoxygenated by incubation for 2 h in a glove box from Belle Technology (Weymouth, UK) kept in nitrogen atmosphere. The reductive half-reaction was investigated by mixing protein ($\sim 20 \mu\text{M}$) in buffer B with 25-2.500 μM NADH or 25-1.000 μM NAD(P)H. The concentrations given are final values after mixing in the flow cell. Experiments were performed with a SF-61SX2 stopped flow device from TgK Scientific Limited (Bradford-on-Avon, UK) positioned in an anoxic glove box from Belle Technology (Weymouth, UK) at 4 °C. Changes in flavin absorption were followed with a PM-61s photomultiplier from TgK Scientific Limited (Bradford-on-Avon, UK) at 453 nm.

Limited proteolysis

12 μM Irc15p in buffer D (50 mM HEPES, 50 mM NaCl, 5 mM EDTA and 1 mM DTT, pH 7.0) in the presence and absence of 50 mM NADH and under oxic or anoxic conditions was digested using 5 $\mu\text{g}/\text{mL}$ trypsin from Promega (Madison, WI, USA). The reactions were also supplemented with 8 mM DTT. The reactions were performed at 37 °C. Reactions in the absence of dioxygen were conducted in a glove box from Belle Technology (Weymouth, UK) filled with nitrogen gas. After preincubation of trypsin at 37 °C for 15 minutes, the digestion was started and samples were taken out after different time points (0, 1, 2, 3, 4, 5, 6 and 16 hours). The reactions were stopped by adding SDS sample buffer and the samples were boiled at 95 °C for 10 minutes. The samples were then analysed by SDS-PAGE with a 12.5% separating and 5% stacking gel. (45, 46)

Hydrogen peroxide assay

A time-dependent generation of H₂O₂ by Irc15p in the presence and absence of NADH was monitored using the Pierce™ Quantitative Peroxide Assay Kit (ThermoFischer Scientific). For the assay, 20 μM Irc15p in buffer C (50mM HEPES, 50 mM NaCl, pH 7.0) was incubated with 50 mM NADH at room temperature. A sample without NADH, also incubated at room temperature, was used as a control. The reactions were terminated at 0, 1 and 16 h by addition of 10% TCA solution. Samples of this reaction mixture (10 μl) were added to 100 μl of the working reagent in a 96-well plate and incubated for 20 min at room temperature. Working reagent was prepared according to the protocol specified in the kit (1 vol of reagent A in 100 vol of reagent B). Absorbance was recorded at 595 nm on a plate reader (FLUOStar Omega plate reader, BMG Labtech). The values were normalized to account for the intrinsic absorption of the working reagent. A standard curve containing 0 to 100 μM of H₂O₂ was prepared to determine the amount of H₂O₂ present in each sample.

Small-angle X-ray scattering

For successful SAXS measurements, an additional purification step of Irc15p was needed. Therefore, Irc15p in buffer D (50 mM HEPES, 50 mM NaCl, 5 mM EDTA and 1 mM DTT, pH 7.0) was purified by size exclusion chromatography on a Superdex 200 Increase 10/300 GL column from GE Healthcare (Little Chalfont, UK) connected to an ÄKTApurifier™ system (GE Healthcare, Little Chalfont, UK). The protein containing fractions were then collected, centrifuged and used for further sample preparation.

For the SAXS measurements, three separate reaction mixtures were prepared, including one control with a concentration of 119 μM Irc15p and two samples with a concentration of 61 μM Irc15p, measured after 0 and 12 hours incubation with 50 mM NADH at 4 °C. Buffers for background corrections were also prepared from buffer D with either 119 μM or 61 μM FAD in the absence or presence of 50 mM NADH. All samples contained 8.3 mM DTT to prevent precipitation of Irc15p.

SAXS data for Irc15p were recorded with an in-house SAXS instrument (SAXSspace, Anton Paar, Graz, Austria) equipped with a Kratky camera, a sealed X-ray tube source and a Mythen2 R 1K Detector (Dectris). Thereby Irc15p and the buffers for background subtraction were loaded via an ASX autosampler and measured in a flow cell. The scattering patterns were measured with a 180-min exposure time (180 frames, each 1 min). Radiation damage was excluded on the basis of a comparison of individual frames of the 180-

min exposures, wherein no changes were detected. A range of momentum transfer of $0.010 < s < 0.63 \text{ \AA}^{-1}$ was covered ($s = 4\pi \sin(\theta)/\lambda$, where 2θ is the scattering angle, and λ is the X-ray wavelength, in this case 1.5 \AA).

Obtained SAXS data were processed using the SAXSanalysis package (Anton Paar, version 3.0). and analyzed using the ATSAS package (version 2.8.2, Hamburg, Germany). The data were desmeared using GIFT (PCG-Software). The forward scattering ($I(0)$), the radius of gyration, (R_g), the maximum dimension (D_{\max}) and the interatomic distance distribution function ($P(r)$) were computed with GNOM (47). The masses of the solutes were evaluated based on their Porod volume.

Acknowledgements

The authors are grateful for the support by the interuniversity program in natural sciences (NAWI Graz) and appreciate the help of Chaitanya R. Tabib for his support with the HPLC analysis and Eva-Maria Frießer for the help with routine work, as protein expression and purification. This work was supported by the Bavarian Ministry of Sciences, Research and the Arts (Bavarian Molecular Biosystems Research Network, to T.M.), the President's International Fellowship Initiative of CAS (No.2015VBB045, to T.M.), the National Natural Science Foundation of China (No. 31450110423, to T.M.), the Austrian Science Fund (FWF: P28854 and I3792 to T.M.), the Austrian Research Promotion Agency (FFG: 864690), the Integrative Metabolism Research Center Graz, the Austrian infrastructure program 2016/2017, BioTechMed/Graz, the OMICS center Graz as well as the Deutsche Forschungsgemeinschaft (DFG) with the grant MA5703/1-1 (to T.M.).

References

1. Gianluca eFarrugia, Rena eBalzan. Oxidative stress and programmed cell death in yeast. *Frontiers in Oncology*. 2012 Jun 1,;2.
2. Zeida A, Babbush R, Lebrero MCG, Trujillo M, Radi R, Estrin DA. Molecular basis of the mechanism of thiol oxidation by hydrogen peroxide in aqueous solution: challenging the SN2 paradigm. *Chemical research in toxicology*. 2012 Mar 19,;25(3):741-6.
3. Groitl B, Jakob U. Thiol-based redox switches. *Biochimica et biophysica acta*. 2014 Aug;1844(8):1335.
4. Lindhoud S, van den Berg, Willy A. M., van den Heuvel, Robert H. H., Heck AJR, van Mierlo, Carlo P. M., van Berkel, Willem J. H. Cofactor binding protects flavodoxin against oxidative stress. *PLoS ONE*. 2012;7(7):e41363.
5. Gudipati V, Koch K, Lienhart WD, Macheroux P. The flavoproteome of the yeast *Saccharomyces cerevisiae*. *Biochim Biophys Acta*. 2014 Mar;1844(3):535-44.
6. Keyes BE, Burke DJ. Irc15 Is a Microtubule-Associated Protein that Regulates Microtubule Dynamics in *Saccharomyces cerevisiae*. *Current Biology*. 2009;19(6):472-8.
7. Argyrou A, Blanchard JS. Flavoprotein disulfide reductases: advances in chemistry and function. *Prog Nucleic Acid Res Mol Biol*. 2004;78:89-142.
8. Miller S, Flavoprotein disulfide reductases and structurally related flavoprotein thiol/disulfide-linked oxidoreductases, in: Hille R, Miller S, Palfey B. (Eds) Volume 2 *Complex Flavoproteins, Dehydrogenases and Physical Methods*. Berlin, Boston: De Gruyter; 2013, 165–201.
9. Mattevi A, Obmolova G, Kalk KH, van Berkel WJ, Hol WG. Three-dimensional structure of lipoamide dehydrogenase from *Pseudomonas fluorescens* at 2.8 Å resolution. Analysis of redox and thermostability properties. *J Mol Biol*. 1993 Apr 20,;230(4):1200-15.
10. Kellis M, Birren BW, Lander ES. Proof and evolutionary analysis of ancient genome duplication in the yeast *Saccharomyces cerevisiae*. *Nature*. 2004 Apr 8,;428(6983):617-24.
11. Byrne KP, Wolfe KH. The Yeast Gene Order Browser: combining curated homology and syntenic context reveals gene fate in polyploid species. *Genome research*. 2005 Oct;15(10):1456-61.
12. French CE, Boonstra B, Bufton KA, Bruce NC. Cloning, sequence, and properties of the soluble pyridine nucleotide transhydrogenase of *Pseudomonas fluorescens*. *J Bacteriol*. 1997 Apr;179(8):2761-5.
13. Boonstra B, French CE, Wainwright I, Bruce NC. The *udhA* gene of *Escherichia coli* encodes a soluble pyridine nucleotide transhydrogenase. *J Bacteriol*. 1999 Feb;181(3):1030-4.

14. Komuniecki R, Saz HJ. Purification of lipoamide dehydrogenase from *Ascaris* muscle mitochondria and its relationship to NADH:NAD⁺ transhydrogenase activity. *Arch Biochem Biophys*. 1979 Aug;196(1):239-47.
15. Argyrou A, Blanchard JS. *Mycobacterium tuberculosis* lipoamide dehydrogenase is encoded by Rv0462 and not by the *lpdA* or *lpdB* genes. *Biochemistry*. 2001 Sep 25;40(38):11353-63.
16. Schneider CA, Rasband WS, Eliceiri KW. NIH Image to ImageJ: 25 years of image analysis. *Nat Methods*. 2012 Jul;9(7):671-5.
17. Benen J, van Berkel W, Zak Z, Visser T, Veeger C, de Kok A. Lipoamide dehydrogenase from *Azotobacter vinelandii*: site-directed mutagenesis of the His450-Glu455 diad. Spectral properties of wild type and mutated enzymes. *Eur J Biochem*. 1991 Dec 18;202(3):863-72.
18. Macheroux P. UV-visible spectroscopy as a tool to study flavoproteins. *Methods Mol Biol*. 1999;131:1-7.
19. Minnaert K. Measurement of the equilibrium constant of the reaction between cytochrome c and cytochrome a. *Biochim Biophys Acta*. 1965 Oct 25;110(1):42-56.
20. UniProt Consortium. UniProt: a hub for protein information. *Nucleic Acids Res*. 2015 Jan;43(Database issue):204.
21. Sievers F, Wilm A, Dineen D, Gibson TJ, Karplus K, Li W, et al. Fast, scalable generation of high-quality protein multiple sequence alignments using Clustal Omega. *Mol Syst Biol*. 2011 Oct 11;7:539.
22. Arnold K, Bordoli L, Kopp J, Schwede T. The SWISS-MODEL workspace: a web-based environment for protein structure homology modelling. *Bioinformatics*. 2006 Jan 15;22(2):195-201.
23. Zhang Y. I-TASSER server for protein 3D structure prediction. *BMC Bioinformatics*. 2008 Jan 23;9:40.
24. Schrödinger LLC, The PyMOL Molecular Graphics System Version 1.5.0.4. (2002)
25. Youn H, Kwak J, Youn HD, Hah YC, Kang SO. Lipoamide dehydrogenase from *Streptomyces seoulensis*: biochemical and genetic properties. *Biochim Biophys Acta*. 1998 Nov 10;1388(2):405-18.
26. Heinrich P, Ronft H, Schartau W, Kresze GB. Lipoamide dehydrogenase from baker's yeast. Improved purification and some molecular, kinetic, and immunochemical properties. *Hoppe Seylers Z Physiol Chem*. 1983 Jan;364(1):41-50.
27. Ericsson UB, Hallberg BM, Detitta GT, Dekker N, Nordlund P. Thermofluor-based high-throughput stability optimization of proteins for structural studies. *Anal Biochem*. 2006 Oct 15;357(2):289-98.

28. Wilkinson KD, Williams CH,Jr. Evidence for multiple electronic forms of two-electron-reduced lipoamide dehydrogenase from *Escherichia coli*. *J Biol Chem*. 1979 Feb 10;254(3):852-62.
29. Hopkins N, Williams CH,Jr. Lipoamide dehydrogenase from *Escherichia coli* lacking the redox active disulfide: C44S and C49S. Redox properties of the FAD and interactions with pyridine nucleotides. *Biochemistry*. 1995 Sep 19;34(37):11766-76.
30. van Berkel WJ, Regelink AG, Beintema JJ, de Kok A. The conformational stability of the redox states of lipoamide dehydrogenase from *Azotobacter vinelandii*. *Eur J Biochem*. 1991 Dec 18;202(3):1049-55.
31. Benen J, van Berkel W, Veeger C, de Kok A. Lipoamide dehydrogenase from *Azotobacter vinelandii*. The role of the C-terminus in catalysis and dimer stabilization. *Eur J Biochem*. 1992 Jul 15;207(2):499-505.
32. Matthews RG, Ballou DP, Williams CH,Jr. Reactions of pig heart lipoamide dehydrogenase with pyridine nucleotides. Evidence for an effector role for bound oxidized pyridine nucleotide. *J Biol Chem*. 1979 Jun 25;254(12):4974-81.
33. Benen J, van Berkel W, Dieteren N, Arscott D, Williams C,Jr, Veeger C, et al. Lipoamide dehydrogenase from *Azotobacter vinelandii*: site-directed mutagenesis of the His450-Glu455 diad. Kinetics of wild-type and mutated enzymes. *Eur J Biochem*. 1992 Jul 15;207(2):487-97.
34. Yu F, Dai R, Goh S, Zheng L, Luo Y. Logic of a mammalian metabolic cycle: An oscillated NAD⁺/NADH redox signaling regulates coordinated histone expression and S-phase progression. *Cell Cycle*. 2009 Mar 1;8(5):773-9.
35. da Veiga Moreira J, Peres S, Steyaert JM, Bigan E, Pauleve L, Nogueira ML, et al. Cell cycle progression is regulated by intertwined redox oscillators. *Theor Biol Med Model*. 2015 May 29;12:2.
36. Harkcom WT, Ghosh AK, Sung MS, Matov A, Brown KD, Giannakakou P, et al. NAD⁺ and SIRT3 control microtubule dynamics and reduce susceptibility to antimicrotubule agents. *Proc Natl Acad Sci U S A*. 2014 Jun 17;111(24):2443.
37. Menon SG, Goswami PC. A redox cycle within the cell cycle: ring in the old with the new. *Oncogene*. 2007 Feb 22;26(8):1101-9.
38. Wilson C, Gonzalez-Billault C. Regulation of cytoskeletal dynamics by redox signaling and oxidative stress: implications for neuronal development and trafficking. *Front Cell Neurosci*. 2015 Sep 30;9:381.
39. Jung Chae Lim, Hoon-In Choi, Yu Sun Park, Hyung Wook Nam, Hyun Ae Woo, Ki-Sun Kwon, et al. Irreversible Oxidation of the Active-site Cysteine of Peroxiredoxin to Cysteine Sulfonic Acid for Enhanced Molecular Chaperone Activity. *Journal of Biological Chemistry*. 2008 Oct 24;283(43):28873-80.
40. Pashley C, Kendall S. Cloning in plasmid vectors. *Methods in molecular biology* (Clifton, N.J.). 2003;235:121.

41. Swords WE. Chemical transformation of *E. coli*. *Methods in molecular biology* (Clifton, N.J.). 2003;235:49-53.
42. Cherry JM, Hong EL, Amundsen C, Balakrishnan R, Binkley G, Chan ET, et al. *Saccharomyces Genome Database: the genomics resource of budding yeast*. *Nucleic Acids Res.* 2012 Jan;40(Database issue):700.
43. Laemmli UK. Cleavage of structural proteins during the assembly of the head of bacteriophage T4. *Nature.* 1970 Aug 15;227(5259):680-5.
44. V. Massey. A simple method for the determination of redox potentials. In: B. Curti, S Ronchi, G Zanetti (eds), editor. *Flavins and flavoproteins.* ; 1990. p. 59-60.
45. Lienhart WD, Gudipati V, Uhl MK, Binter A, Pulido SA, Saf R, et al. Collapse of the native structure caused by a single amino acid exchange in human NAD(P)H:quinone oxidoreductase(1.). *The FEBS journal.* 2014 Oct;281(20):4691-704.
46. Chen S, Deng PS, Bailey JM, Swiderek KM. A two-domain structure for the two subunits of NAD(P)H:quinone acceptor oxidoreductase. *Protein science : a publication of the Protein Society.* 1994 Jan;3(1):51-7.
47. Svergun DI. Determination of the regularization parameter in indirect-transform methods using perceptual criteria. *Journal of Applied Crystallography.* 1992 Aug 1;25(4):495-503.

Curriculum vitae
Shalinee Jha



Personal Data

Name Shalinee Jha
Address Steyrergasse 67-4, 8010 Graz
Mobile +43 688 60925660
E-Mail shalinee.jha@tugraz.at
DOB 21.10.1988 in Jamshedpur, India

Education and Research experience

- Nov 2014- Dec 2018** Graz University of Technology
PhD in Biochemistry
PhD thesis: “Biochemical and metabolic studies towards characterization of dipeptidyl peptidyl-3 knockout mice”
- July 2012- July 2014** Indian Institute of Technology-Guwahati
M.tech in Biotechnology
M.Tech thesis: “Elucidation the structural mechanism of inhibition of matrix metalloproteinase-2 by green tea polyphenol epigallocatechin 3-gallate”
- July 2008- July 2012** G. B. Pant University of Agriculture and Technology
B.Tech in Biotechnology
B.Tech thesis: “Engineering drought stress tolerance in plants”

Technical skills

- Animal manipulation** Handling of transgenic mice, behavioral and metabolic studies, genotypic and phenotypic characterization, collection and processing of biological samples (e.g. tissues, plasma, serum, whole blood, urine, etc.)
- Molecular cloning** Vector design: primers design, digestions, ligations, transformation, R N A extraction, reverse transcription, qPCR, PCR, DNA purification (CsCl gradient, mini- and maxi-preps), DNA gel analysis, quantification and extraction.
- Biochemistry** Recombinant protein expression and purification, SDS-PAGE, Western blot, ELISA, enzymatic assays.
- Analytical methods** Titrations, spectrophotometry, chromatography (thin layer, ion exchange, size exclusion, HPLC), sound theoretical knowledge and interpretation of most analysis techniques (NMR, MS,...)

Publications

- Linda Rehfeld et al. Novel methods for the quantification of Dipeptidyl Peptidase 3 (DPP3) concentration and activity in human blood samples. (Accepted in The Journal of Applied Laboratory Medicine)
- Karin Koch et al. Oxidative stress induced structural changes in the microtubule-associated flavoenzyme Irc15p from *Saccharomyces cerevisiae*. *Protein Science*, 2018 Sep 29. doi: 10.1002/pro.3517
- Shalinee Jha et al. Direct inhibition of matrix metalloproteinase-2 (MMP-2) by (-)-epigallocatechin-3-gallate: A possible role for the fibronectin type II repeats. *Gene*, 593 (2016) 126–130

Achievements

- August 2016** Invited talk at XXIV EFMC International Symposium on Medicinal Chemistry, Manchester, UK
- August 2016** Royal Society of Chemistry travel prize to attend XXIV EFMC International Symposium on Medicinal Chemistry, Manchester, UK
- July 2015** Discussion leader at the Gordon Research Seminar on Enzymes, Co-enzymes and Metabolic pathways, Waterville Valley, New Hampshire, USA

Languages and Skills

- Languages** English: Fluent
Hindi: Mother tongue
German: Elementary
- Computer skills** Microsoft Office (Word, Excel), Linux, GraphPad, PyMOL, AutoDock

Certifications

- December 2017** Effective Scientific Writing in English
- July 2016** Felasa B Lab Animal Training course

List of Publications

1. **Jha S**, Taschler U, Domenig O, Poglitsch, Bourgeois B, Madl T, Gruber K, Breinbauer R, Zimmermann R and Macheroux P. Knock-out of DPP3 in mice unravel its involvement in the metabolic regulation of the renin-angiotensin system. (Manuscript in preparation).
2. Ivkovic Jakov, **Jha S**, Lembacher-Fadum C, Macheroux P and Breinbauer R. Efficient inhibition of a metallopeptidase by hydroxyethylene transition state peptidomimetics. (Manuscript in preparation).
3. Koch K, Strandback E, **Jha S**, Richter G, Bourgeois B, Madl T and Macheroux P. Oxidative stress induced structural changes in the microtubule-associated flavoenzyme Irc15p from *Saccharomyces cerevisiae*. *Protein Sci.* 2018 Sep 29.
4. Rehfeld L, Funk E, **Jha S**, Macheroux P, Mellander O and Bergmann A. Novel methods for the quantification of Dipeptidyl Peptidase 3 (DPP3) concentration and activity in human blood samples. (Accepted in *The Journal of Applied Laboratory Medicine*).
5. **Jha S**, Kanaujia SP and Limaye AM. Direct inhibition of matrix metalloproteinase-2 (MMP-2) by (?)-epigallocatechin-3-gallate: A possible role for the fibronectin type II repeats. *Gene*, 593 (2016) 126–130

List of Posters and Oral Presentations

- 07/2017 Gordon Research Conference and Seminar on Enzymes, Co-enzymes and Metabolic pathways, New Hampshire, USA, **Poster Presentation**
- 07/2017 18th Doc Day NAWI Graz Doctoral School of Molecular Biosciences and Biotechnology, Graz, **Oral Presentation**
- 06/2017 DK Molecular Enzymology Graduate Seminar 2017, **Oral Presentation**
- 02/2017 17th Doc Day NAWI Graz Doctoral School of Molecular Biosciences and Biotechnology, Graz, **Poster Presentation**
- 09/ 2016 Retreat at Semmering 2016, Joint retreat with DK Biomolecular Technology of Proteins, Vienna, Semmering, Austria, **Poster Presentation**
- 09/ 2016 8th ÖGMBT Annual Meeting 2016, Graz, Austria, **Poster Presentation**
- 08/2016 XXIV EFMC International Symposium on Medicinal Chemistry, Manchester, UK, **Oral Presentation**
- 12/2015 5th Austrian Peptide Symposium, Vienna, Austria, **Poster Presentation**
- 07/ 2015 14th Doc Day NAWI Graz Doctoral School of Molecular Biosciences and Biotechnology, Graz, **Poster Presentation**
- 07/ 2015 Gordon Research Conference and Seminar on Enzymes, Co-enzymes and Metabolic pathways, New Hampshire, USA, **Poster Presentation**
- 05/2015 DK Molecular Enzymology Graduate Seminar, Graz, Austria, **Poster Presentation**

Achievements

- 09/2016 Royal Society of Chemistry **BMC Travel Prize** for XXIV EFMC International Symposium on Medicinal Chemistry, Manchester, UK
- 07/2015 **Discussion leader** at the Gordon Research Seminar and Conference on Enzymes, Co-enzymes and Metabolic pathways, Waterville Valley, New Hampshire, USA

We shall not cease from exploration. And the end of all our exploring will be to arrive where we started and know the place for the first time.

Thomas Stearns Eliot

Nobel Prize in Literature, 1948